Microstructure Development in Magnetite Films via Non-classical Crystallization

by

Kaushik Sridhar Vadari Venkata

A Dissertation Presented in Partial Fulfillment
of the Requirements for the Degree
Doctor of Philosophy

Approved March 2018 by the
Graduate Supervisory Committee:

William Petuskey, Chair
Ray Carpenter
Martha McCartney
Candace Chan

ARIZONA STATE UNIVERSITY

May 2018

ABSTRACT

Polycrystalline magnetite thin films were deposited on large area polymer substrates using aqueous solution based spin-spray deposition (SSD). This technique involved the hydrolysis of precursor salt solutions at low temperatures (70-100°C). The fundamental mechanisms and pathways in crystallization and evolution of the film microstructures were studied as a function of reactant chemistry and reactor conditions (rotation rate, flow rates etc.). A key feature of this method was the ability to constantly supply fresh solutions throughout deposition. Solution flow due to substrate rotation ensured that reactant depleted solutions were spun off. This imparted a limited volume, near two-dimensional restriction on the growth process. Film microstructure was studied as a function of process parameters such as liquid flow rate, nebulizer configuration, platen rotation rate and solution chemistry. It was found that operating in the micro-droplet regime of deposition was a crucial factor in controlling the microstructure.

Film porosity and substrate adhesion were linked to the deposition rate, which in-turn depended on solution chemistry. Films exhibited a wide variety of hierarchically organized microstructures often spanning length scales from tens-of-nanometers to a few microns. These included anisotropic morphologies such as nanoplates and nanoblades, that were generally unexpected from magnetite (a high symmetry cubic solid). Time resolved studies showed that the reason for complex hierarchy in microstructure was the crystallization via non-classical pathways. SSD of magnetite films involved formation of precursor phases that subsequently underwent solid-state transformations and nanoparticle self-assembly. These precursor phases were identified and possible reaction mechanisms for the formation of magnetite were proposed. A qualitative description of the driving forces for self-assembly was presented.

In loving memory of my grandmother, C. Meenakshi (1941-2016)

&

my father, Dr. V.V. Giridhar (1958-2018)

ACKNOWLEDGMENTS

I would like to express my sincere gratitude to my research advisor Prof. William Petuskey for his constant support and guidance throughout my graduate study. I greatly appreciate his faith in my research ideas and the freedom he granted me to tackle various aspects of this research. I thank my committee members Prof. Ray Carpenter, Prof. Martha McCartney and Prof. Candace Chan for their generous time and advice towards completion of my dissertation. I would also like to acknowledge financial support from Advanced Materials Initiatives (AMI) at ASU and Northrop Grumman.

I have had the privilege of getting hands-on training in various materials characterization techniques during my studies at ASU. This would not have been possible without the keen mentorship I received from the staff at the Leroy Eyring Center for Solid State Science. This includes David Wright, Emmanuel Soignard, Karl Weiss and Shery Chang. Special thanks to Dr. Thomas Groy, for his assistance with diffraction analysis and lengthy discussions on science and life during various phases of my graduate study. I would also like to thank Grant Baumgardner for his help and advice in maintaining the spin spray disc reactor.

I am forever grateful to my colleagues over the years- Nicole Ray (for her guidance and mentorship in the use of the spin spray reactor), Blake Rogers (for helping me find unique solutions to engineering problems), Alicia Brune (for the various discussions on crystal growth) and Heath Lorzel (for sharing his insight on fluid flow inside the spin spray reactor). I would also like to thank all my friends at ASU for their support and company.

Lastly, I would like to thank my family for their unconditional love and support. My grandmother always motivated me to face adversity with relentless positivity and my scientific pursuit is inspired by my first science teacher, my father. This dissertation is my humble dedication to honor their memory.

TABLE OF CONTENTS

Page

LIST OF TABLES ix

LIST OF FIGURES x

CHAPTER

1. INTRODUCTION 1
    1.1. Research Objectives 2
    1.2. Background and Literature Review 3
        1.2.1 Classical Crystallization 3
        1.2.2 Non-classical Crystallization 5
        1.2.3 Low Temperature Solution Deposition of Metal Oxide Thin Films 12
2. EXPERIMENTAL METHODOLOGY 17
    2.1. Spin Spray Deposition 17
    2.2. Characterization Techniques 22
        2.2.1. X-ray Diffraction 22
        2.2.2. Electron Microscopy 24
3. DEPOSITION OF MAGNETITE FILMS USING SPIN SPRAY DEPOSITION. 30
    3.1. Deposition of Magnetite Films Using Ammonia/Acetate Based Oxidant solutions 30
    3.2. Deposition of Magnetite Films Using Bicarbonate Based Oxidant Solutions .. 33
    3.3. Reaction Chemistry for the Spin Spray Deposition of Magnetite 37
        3.3.1. From Ammonia/Acetate Based Oxidant Solutions 37
        3.3.2. From Bicarbonate Based Oxidant Solutions 39

3.4 Conclusions 44
4. PROCESS DEPENDENT MORPHOLOGIES OF MAGNETITE 46
4.1. Effect of Process Parameters Affecting Fluid Flow 47
4.1.1 Number of Nebulizers and Nebulizer Configuration 47
4.1.2 Platen Rotation Speed (P_r) 55
4.2. Effect of Process Parameters Affecting Chemical Behavior of Solutions 61
4.2.1. Effect of Concentration of HCO_3^- 61
4.2.2. Effect of Fe^{2+} Concentration 63
4.3. Conclusions 69
5. STRUCTURAL ANALYSIS OF HIERARCHICALLY ORDERED MAGNETITE 71
5.1. TEM Studies 71
5.2. Conclusions 77
6. MECHANISTIC ASPECTS OF MAGNETITE FILM GROWTH USING SPIN SPRAY DEPOSITION 78
6.1. Time Resolved Evolution of Porous Magnetite Films 78
6.2. Time Resolved Evolution of Dense Magnetite Films 94
6.3. Comparison of Growth Mechanisms with Other Studies on Oxide Deposition Via Chemical Solution 104
6.4. Role of Intermolecular Forces in Film Deposition and Self-assembly 105
6.5. Implications of Non-classical Crystallization in Microstructural Development of Thin Films 108

CHAPTER Page

6.6. Conclusions 110
7. SUMMARY AND CONCLUSIONS 111
REFERENCES 119

LIST OF TABLES

Table Page

4.1. Spin Spray Deposition Process Parameters 46

4.2. Deposition Conditions for Experiments in Section 4.1 48

LIST OF FIGURES

Figure Page

1.1 Free Energy Change (ΔG) Associated with Crystallization as a Function of Particle Size (r)……………………………………………………………….................... 4

1.2 TEM Images Showing Hydrothermally Coarsened Anatase…………………………..6

1.3 Pathways to Crystallization by Particle Attachment (CPA).…………………………...8

1.4 Schematic Showing Classical (left) and Non-classical (right) Crystallization Pathways…………………………………………………………………............10

1.5 Spin Spray Plating….………………………………………………………………...16

2.1 Schematic of Spin Spray Disc Reactor……………………………………………….19

2.2 Experimental Set Up for Spin Spray Deposition (SSD) ……………………………..20

2.3 Schematic Showing Principle of X-ray Diffraction. Waves 1, 2 and 3 Are Incident X-Ray Radiation While 1', 2' and 3' Are Scattered Waves from the Crystal. hkl Denotes the Miller Indices of the Diffracting Planes of the Crystal……………………………23

2.4 Schematic of a Scanning Electron Microscope (SEM)…..…………………………..26

2.5 Electron-sample Interaction Volume ………………………………………………...27

2.6 Schematic of a Transmission Electron Microscope (TEM)..….……………………...29

3.1 A Typical Magnetite Film Deposited in 30 Mins Using Ammonium/Acetate Based Oxidant Solution……………………………………………………………………..31

3.2 SEM Images of Magnetite Films Showing Dense Polycrystalline Microstructure. Insets Show That Each Mosaic Grain Is Made of Several Spherical Nanoparticles…………32

3.3 Cross-section SEM Images of a Magnetite Film Showing Columnar Growth………33

Figure Page

3.4 A Typical Magnetite Film Deposited in 30 Mins Using Sodium Bicarbonate Buffered Oxidant Solution…………………………………………………….....................34

3.5 SEM Images of Magnetite Film Deposited Using Bicarbonate Buffered Oxidant Solution (a) Low Magnification Image Showing Micron-sized Clusters, (b) Higher Magnification Image of Clusters Showing Nanoflakes and (c) Equiaxed Polycrystalline Structures………………………………………………………………................36

3.6 Formation of Magnetite by Spin Spray Deposition as Described by Abe…………….38

3.7 General Structure of a Layered Double Hydroxide (LDH)…………………………..41

4.1 Schematic of Nebulizer Configuration N-8- X_n Denotes Reactant Solution Spray and O_n Denotes Oxidant Solutions Spray…………………………………………………48

4.2 Approximate Areas of Film Coverage (From Corresponding Pairs of Nebulizers (X_nO_n)) Represented as Rings Superimposed on a Film Deposited with 8 Nebulizers at 90 Rpm………………………………………………………………………………49

4.3 SEM Images of Film Deposited for 90 Mins (a) Nanoplates Showing Lenticular Cross-section (b) Faceted Cube Showing Nanoscale Roughness (c and d) Occurrence of Faceted Polycrystals (blue arrows) and Nanoplates (red arrows) within the Same Region of the Film…………………………………………………………………51

4.4 Schematic Showing Differences in Liquid Film Thickness Across the Substrate……52

4.5 Schematic Depicting Liquid in Continuous Layer Regime and Microdroplet Regime.52

4.6 SEM Images of Magnetite Film Deposited Using Two Nebulizers at X_1 and O_1 (a) Low Magnification Image Showing Micron-sized Clusters (b) High Magnification Image Showing Nanoplate Sub-units That Are Contained in the Clusters…..........................54

Figure Page

4.7 SEM Images of Films Deposited at P_r=150 Rpm (a and b) Low Magnification Images Showing Micron-sized Clusters (c) High Magnification Image Showing Blade-like Subunits That Are Contained in the Clusters………………………….................56

4.8 SEM Images of Films Deposited at P_r=150 Rpm (Taken with the Sample Tilted at 54°) (a) Low Magnification Image of Clusters (b) High Magnification Image Showing Blade-like Subunits That Are Contained in the Clusters (c) Low Magnification Image Showing Homocentric Assembly of Blade-like Sub-units…………………………...57

4.9 Low Magnification SEM Images of Films Deposited at P_r=200 Rpm………………58

4.10 (a) SEM Image Showing Columns Made up of Stacked Mosaic Discs (b) High Magnification Image Showing Mosaic Discs……………………………………...59

4.11 SEM Images of Films Deposited at P_r=200 Rpm (Taken with the Sample Tilted at 45°) (a) Low Magnification Image Showing Clusters of Columns (b) High magnification Image of the Same……………………………………………………60

4.12 Schematic of the Different Hierarchical Morphologies of Magnetite Films………60

4.13 SEM Images Showing Microstructures of Films Deposited with Various Concentrations of $NaHCO_3$………………………………………………………..62

4.14 SEM Images Showing Microstructures of Films Deposited with Various Concentrations of $FeCl_2$………………………………………………………...64

4.15 Field Map of Microstructural Features of Magnetite Films as a Function of [Fe^{2+}] and [HCO_3^-]……………………………………………………………………………67

4.16 (a) Linear Deposition Rate Vs [HCO_3^-] (b) Linear Deposition Rate Vs [Fe^{2+}] (c) Linear Deposition Rate Vs [Fe^{2+}] . [HCO_3^-] ………………………………………..68

Figure Page

4.17 Mass Deposition Rate Vs [HCO_3^-] at Fixed [Fe^{2+}] =16.7 mM……………………...69

5.1 TEM Images of a Nanoplate (a) Low Magnification Image Showing Aggregation of Primary Nanoparticles (Arrows Indicate Examples of Internal porosity) (b) HRTEM Image Showing Crystalline Nature of Nanoparticles (c) SAED Pattern of Nanoplate Showing Preferred Orientation (Indexed Planes Correspond to Magnetite)…………73

5.2 TEM Images of a Nanoblade (a) Low Magnification Image Showing Two Overlapping Nanoblades (b) HRTEM and FFT (Inset) Image Showing Crystalline Nature of Nanoblades ([1 1 2] Zone Axis of Magnetite)………………………………………..75

5.3 TEM Images of a Nanoplate (a) Low Magnification Image Showing Stacked Columns (Scale Bar- 0.2 μm) (b) HRTEM and FFT (Inset) Image Showing Presence of Nanocrystalline Sub-units (Arrows Indicate Examples of Internal Pores, Scale Bar- 10 nm)…………………………………………………………………………...76

6.1 XRD of Films Deposited for Various Times with P_r= 150 Rpm (Magnetite Peaks Are Denoted by Black Cross-marks, Substrate Peaks Are Denoted by Green Circles)……79

6.2 Morphological Evolution of Films Deposited with P_r= 150 Rpm……………………81

6.3 XRD of Films Deposited for Various Times with P_r= 200 Rpm (Magnetite Peaks Are Denoted by Black Squares, Substrate Peaks Are Denoted by Green Circles)……….82

6.4 Morphological Evolution of Films Deposited with P_r= 200 Rpm……………………84

6.5 (a) Low Magnification TEM Image of Green Rust Platelets, (b) A Green Rust Plate and its Corresponding SAED Pattern (Inset)……………………………………………...86

6.6 Polyhedral Representation of the Crystal Structures (Created Using VESTA 3 and *CrystalMaker*® Softwares) of (a) Iron Hydroxycarbonate (Rhombohedral axes) and (b) Magnetite, as Seen From [1 1 1] Directions……………………………………..87

6.7 (a) SEM Image of a Nanoflake Showing Cracks on Its Surface (The Arrows Show Epitaxially Growing Magnetite Crystals) (b) TEM Image of a Nanoflake Showing Contrast Variations and Constituent Nanoparticles…………………………………88

6.8 Schematic Illustration of Growth Mechanism of Films Deposited at P_r= 150 Rpm. The Dark dots in b) and c) Represent Nucleating Magnetite Nanoparticles………………90

6.9 Schematic Illustration of Preferential Vertical Growth of Columns (Above) and an SEM Image (Below) Depicting the Same……………………………………………92

6.10 Schematic Illustration of Growth Mechanism of Films Deposited at P_r= 200 Rpm. The Dark Dots in b) and c) Represent Nucleating Magnetite Nanoparticles…………93

6.11 (a) SEM Image of Film After 5 Mins of Deposition (b) TEM Image Showing Mosaic Nature of Spindles (c) HRTEM Image and FFT (Inset) of a Single Mosaic Spindle….96

6.12 GIXRD of Film Deposited for 20 Mins Showing a Broad (1 1 3) Maghemite Peak...97

6.13 XRD of Films Deposited at 60, 90 and 120 Mins (Magnetite Peaks Are Denoted by Black Squares, Substrate Peaks Are Denoted by Green Circles)……………………97

6.14 Morphological Evolution of Dense Magnetite Films……………………………...100

6.15 (a) Mosaic Truncated Octahedron (b) Magnetite Crystal Shape Generated Using VESTA 3 (Red faces Correspond to 1 1 1 Family of Planes and Blue Faces Correspond to 1 1 0 Family of Planes)………………………………………………………...103

Figure Page

7.1 Schematic Demonstrating the Complexity of the Free Energy Landscape (Pathways B and C) in Crystal Growth by Spin Spray Deposition. Pathway A Represents Crystal Growth as Described by Classical Pathways…………………………………………….................114

Chapter 1

INTRODUCTION AND LITERATURE REVIEW

The crystal structure and bonding of a material influences the various physical properties of that material. It is for this reason that much effort taken by scientists around the world has been devoted to developing techniques to study crystal structure and the crystallization phenomenon. For the most part of the 20th century, crystallization has been studied from the perspective of classical nucleation and growth theories, the foundations of which were laid as early as the 1800s by J.W. Gibbs and Wilhelm Ostwald. While the classical nucleation and growth theories have had tremendous success in describing crystallization in a plethora of materials, there has been an increasing number of examples where they cannot be used completely to explain crystal formation. Over the last decade, elaborate studies on crystals occurring in nature and synthetic environments have suggested that crystals can also form and grow by particle attachment [1]. This mechanism is referred to as non-classical crystallization and involves crystal growth from any of intermediate clusters, liquid precursors, amorphous precursors or nanoparticles that serve as primary building blocks as opposed to classical crystallization where crystals form through monomer (such as atom by atom) mediated steps[2]. Such mechanisms can play an influential role in the development of functional nanomaterials for various applications.

Recently, ferrite thin and thick films deposited by the spin spray deposition method have been shown to exhibit excellent magnetic properties[3]. Structural analysis alluded to the involvement of non-classical crystal growth modes in their deposition. This provided motivation for the study of crystallization pathways involved in the development of film microstructure.

1.1 Research Objectives:

A clear understanding of crystal growth mechanisms is imperative for tailoring the microstructure from film deposition. In this research, magnetite films were deposited using a low temperature aqueous deposition technique called spin spray deposition (SSD). The use of bicarbonate based solutions as pH adjuster led to the formation of hierarchically self-assembled microstructures that scaled from a few nanometers to a few microns. The grand objective of this thesis was to determine the mechanisms involved in the crystallization of magnetite films deposited by SSD and tailor their microstructure. In particular, the role of non-classical crystallization and particle attachment in microstructure development was investigated. Nanoparticle self-assembly and aggregation are directly influenced by the rate of solid formation (nucleation and growth) from solution. In this regard, a comprehensive study of the effect of deposition rate on the growth characteristics was carried out. Deposition rate was controlled by varying process parameters such as liquid flow rates, position of nebulizers and most importantly, solution chemistry. In addition, time resolved studies were carried out to identify precursor phases to magnetite, their transformations and influence on the final microstructure of the films. A qualitative description of the driving forces for self-assembly was also discussed. Structural analysis of various hierarchical microstructures was carried out using electron microscopy.

1.2. Background and review of relevant literature:

1.2.1 Classical crystallization:

Crystallization from solution involves formation of a new solid phase that is thermodynamically more stable, i.e. has a lower free energy relative to the same components in the bulk of the solution. Classical crystallization theory describes the formation of this lower free energy phase by atom-by-atom or monomer-by-monomer addition along with dissolution of unstable phases and re-precipitation of stable phases [4]. According to this theory, formation of a new phase in solution begins when a solution is supersaturated with respect to the solute. With increase of supersaturation, more and more solid precipitates in order to decrease the total free energy of the system. These particles are very small in size and are called nuclei. The process of formation of nuclei is called nucleation.

Nucleation can be of two types, that is, homogeneous and heterogeneous. The former involves formation of nuclei from the bulk of the solution while the latter involves formation of nuclei at the interface of a liquid and a surface. In homogeneous nucleation, the overall free energy change involved in the formation of a new phase in solution involves the sum of two terms, namely, free energy change due to transformation of a new volume and free energy due to formation of a new surface. This overall free energy change (ΔG) can be represented by the following equation for spherical particles,

$$\Delta G = \frac{-4}{3}\frac{\pi r^3 k_B T ln(S)}{V} + 4\pi r^2 \gamma \quad \text{- (1.1)}$$

where V is the molecular volume of the precipitated particle, r is the radius of the particle, k_B is the Boltzmann constant, T is the temperature, S is the degree of supersaturation and γ is the surface free energy per unit area. A supersaturated solution is one that contains more dissolved material than the solvent can hold in normal conditions (thermodynamic equilibrium). The degree of supersaturation defines how far a solution is from thermodynamic equilibrium. The overall free energy with respect to changing radius can be represented as shown in Figure 1.1.

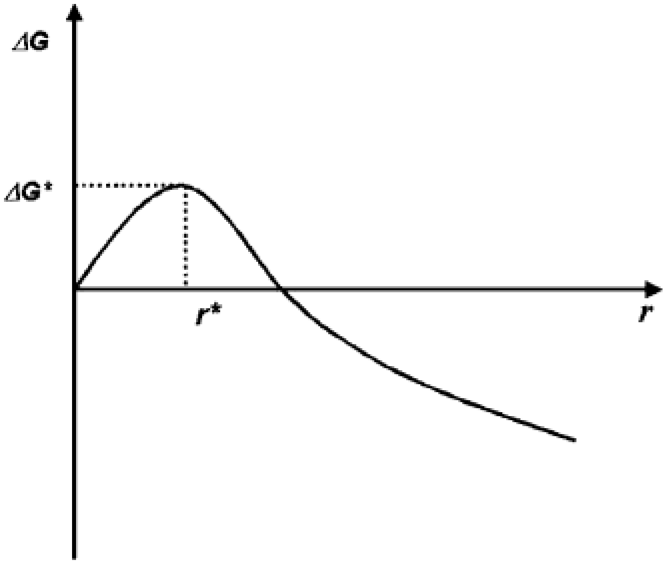

Figure 1.1: Free energy change (ΔG) associated with crystallization as a function of particle size (r)[4]

The value of r for which ΔG is a positive maximum is called the critical radius, r*. Particles formed in the solution with radius r<r* dissolve back into solution. Particles with r=r* are called nuclei. Particles with r>r* will further decrease their free energy by growing and are called stable nuclei. The expression for r* is obtained by solving eqn. (1) for ΔG at its maximum, that is,

$$r^* = \frac{2V\gamma}{3k_B T ln(S)} \qquad \text{- (1.2)}$$

Nuclei will continue to form, grow, dissolve, as long as the solution is supersaturated with respect to the precipitated species. Generally, the larger the supersaturation, the greater the number of nuclei produced and the more rapid the nucleation.

The next step in crystallization according to classical theory is the growth of stable nuclei by a phenomenon known as Ostwald ripening. This process involves the growth of larger particles at the expense of the smaller particles i.e., larger particles continue to grow and the smaller particles get smaller, dissolve and re-precipitate onto the larger particles. This process is thermodynamically spontaneous as the larger particles have lesser surface energy as compared to smaller particles. Ripening occurs with progress in time as the supersaturation of the solution decreases and hence the critical radius r* increases. As a result, the radius for particles to remain stable in solution is greater than the initial particle size.

1.2.2 Non- classical crystallization:

The need for an alternative formalism for crystallization arose from the difficulty faced by researchers to explain the formation of a wide variety of biominerals occurring in nature. Biominerals are crystals synthesized by organisms for their own functional requirements [5]. The most common biominerals are calcium carbonates. Nature exhibits a wide variety of calcium carbonate crystals in sea urchin spines, crustacean exoskeletons, foraminifer shells, etc. Other examples include elongated nanocrystals of magnetite produced by magnetotactic bacteria[6]. Many such symmetry defying forms of crystals could not be explained within the thermodynamic and kinetic boundaries imposed by the classical nucleation theory. In addition to the crystals observed in nature, other examples of anisotropic and complex crystals synthesized in laboratory conditions also posed the same problems.

In the early '90s, when Penn and Banfield [7] were studying coarsening mechanisms in nanocrystalline titania under hydrothermal conditions, they observed that titania nanoparticles underwent coarsening via spontaneous self-organization of adjacent nanoparticles. They noticed that these particles, upon assembling, shared a common crystallographic orientation. It was proposed that this phenomenon occurred because nanoparticles have high surface energy and hence, prefer to associate to eliminate a surface and decrease the overall free energy. It was observed that hydrothermally coarsened anatase showed organization of several primary nanocrystallites into single crystalline structures (Figure 1.2).

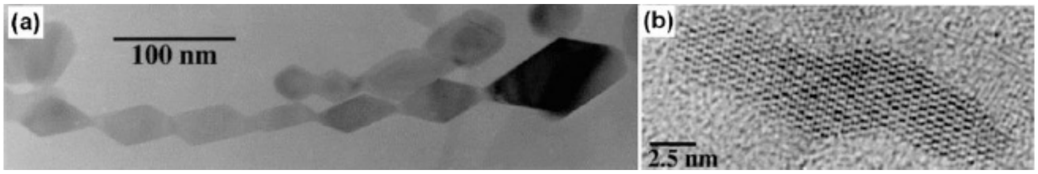

Figure 1.2: TEM images showing hydrothermally coarsened anatase[7]

Non-classical crystallization involves particle mediated reaction channels as compared to ion mediated channels as in classical crystallization [2, 8]. There can be various steps within the non-classical crystallization formalism and have been postulated in Colfen's textbook on mesocrystals. These are:

a) Formation of intermediary clusters as primary building blocks.
b) Crystallization via amorphous intermediates.
c) Oriented attachment of nanoparticles.
d) Mesocrystallization (3D self-organization).

Non-classical crystallization has been described by some authors [1] as crystallization by particle attachment. The graphic below illustrates the various pathways thought to be involved in crystallization by particle attachment.

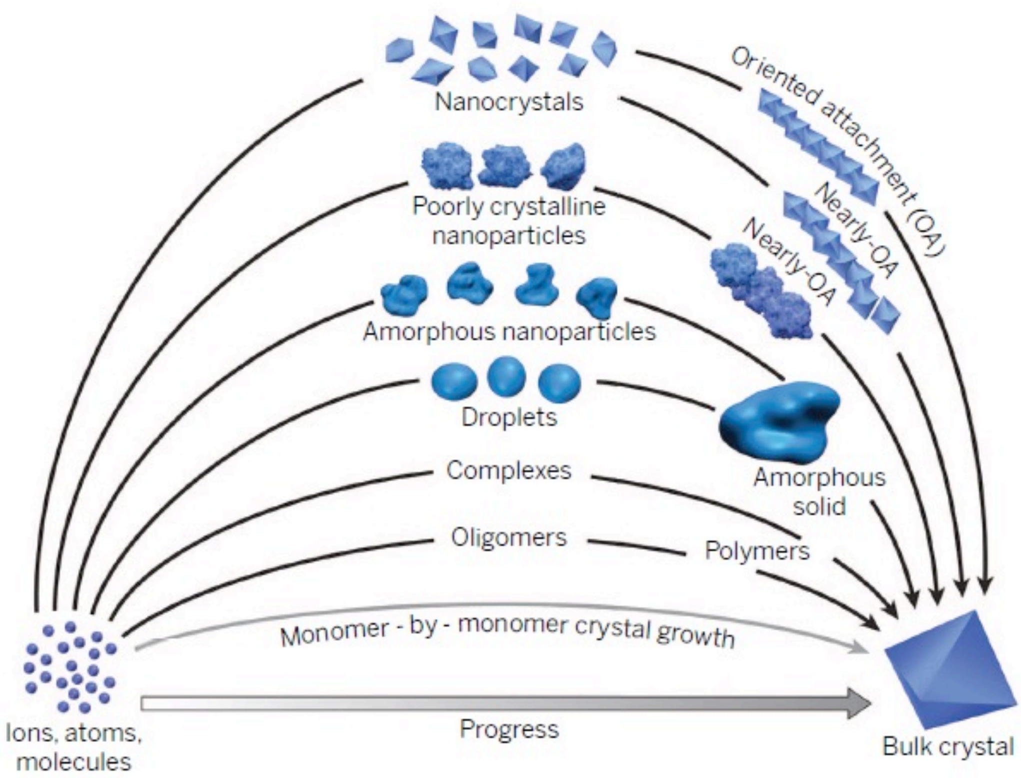

Figure 1.3: Pathways to crystallization by particle attachment (CPA)[1]

It is to be noted that both classical and non-classical crystallization mechanisms start with formation of primary particles or nuclei [9]. It is the growth into a crystal after this step that differs between the two.

Oriented Attachment (OA) and Mesocrystals:

As mentioned earlier, oriented attachment was described by Penn and Banfield in their studies on TiO_2. Kinetic models proposed by Penn[10] consider two mechanisms for nanoparticle collisions to result in an irreversible oriented aggregate. The first mechanism considered a collision to result in oriented attachment only if the colliding nanoparticles came together in oriented fashion at the time of collision. The second route involved formation of an intermediate complex between any two colliding nanoparticles and subsequent reorganization leading to the final oriented aggregate. Either route yielded second order rate laws dependent on the concentration of the primary nanoparticles. An important understanding obtained from this kinetic description is that particles can be expected to undergo oriented attachment when the solution pH is closer to its isoelectric point. It was also concluded that presence of ligands and passivating agents or change in solvents can significantly control growth by oriented attachment.

Mesocrystals as defined by Colfen et al. [8] are crystals composed of individual nanocrystals that align in a common crystallographic fashion exhibiting scattering properties similar to a single crystal. The latter property of mesocrystals is a defining feature that determines detection of such crystals. Mesocrystals have received growing attention in the scientific community owing to the unique properties that they can exhibit and the prospect of obtaining fascinating nanostructures. Its unusual mechanical properties [2] and inherent porosity makes them interesting candidates for applications like thermal and dielectric insulation and as medical delivery systems. Mesocrystals often exhibit superstructures using nanoparticle building units with anisotropic shapes and hence offer exciting prospects for control of crystal morphology [8]. A large fraction of mesocrystals synthesized involve use of polymer additives to stabilize the mesocrystals as they can transform to single crystals by OA and fusion. Hence, it has been suggested that mesocrystals could serve as intermediates to single crystal formation. It is to be noted that mesocrystals can and have been synthesized without the use of polymer additives[11]. Figure 1.4 illustrates mesocrystal formation as compared to classical crystallization.

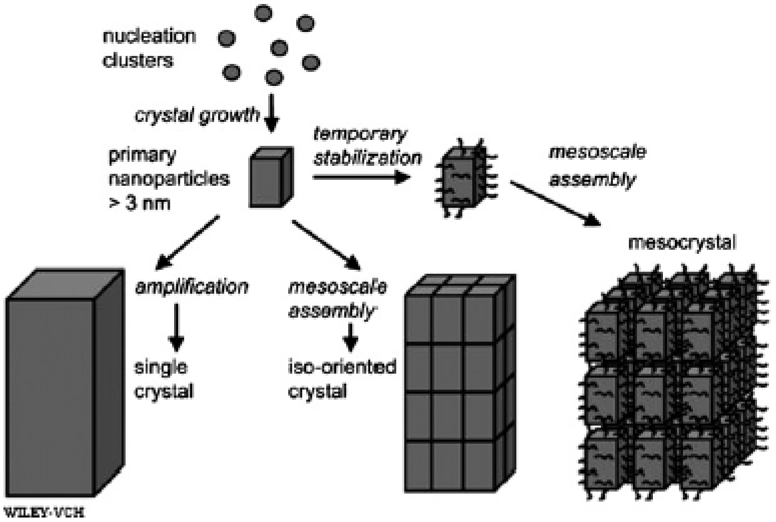

Figure 1.4: Schematic showing classical (left) and non-classical (right) crystallization pathways. [4]

Detection of OA and mesocrystals generally involves analysis of crystals using Scanning Electron Microscopy (SEM) and High Resolution Transmission Electron Microscopy (HRTEM) but is not limited to these. Combinations of direct imaging, spectroscopy and scattering techniques including Small Angle X-ray Scattering (SAXS), Wide Angle X-ray Scattering (WAXS) etc. may be needed to detect OA and mesocrystals.

Oriented aggregates and Mesocrystals in iron oxide systems:

There have been several reports on the synthesis of iron oxide mesocrystals in synthetic environments. M.Ocana et al.[12] reported the synthesis of ellipsoidal hematite (α-Fe_2O_3) mesocrystals by homogeneous precipitation that had formed by the aggregation of smaller anisotropic particles of 30-40 nm in diameter. Shindo et al.[13] reported the synthesis of pseudocubic mesocrystals of α-Fe_2O_3 showing high order of alignment.

M.Nidereberger et al.[14] also synthesized hematite mesocrystals using hydrothermal synthesis. Their mesocrystals showed remarkable features of organization and interpenetrating crystals. Penn et al. synthesized α-FeOOH (goethite) nanorods by oriented aggregation of ferrihydrite nanoparticles[15]. They demonstrated the use of OA to form nanorods of various sizes. Oriented assemblies of spherical magnetite (Fe_3O_4) particles were synthesized using solvothermal synthesis by Yu et al.[16] They also demonstrate the synthesis of microporous spheres using the same technique. Liu et al. [17]demonstrated ionic-liquid assisted solvothermal synthesis of self-assembled Fe_3O_4 nanoflakes of 500 nm diameter. The nanoflakes were made up of an assembly of 15 nm nanocrystals. J.Wan et al.[18] synthesized monodispersed spherical Fe_3O_4 mesocrystals using solvothermal treatment of ferrous chloride in ethylene glycol and in the presence of sodium hydroxide. The mesocrystals of 300 nm diameter and were made up of 23 nm sub-crystallites.

It has been suggested that iron oxides have a particular affinity to forming mesocrystals[8]. This could be attributed to the thermodynamic complexity involved in the iron oxide/oxyhydroxide system. Navrotsky et al.[19] determined formation and surface energies of many of these oxides and have inferred that stability of the oxide phases is size driven, leading to cross-overs at different size scales i.e. an oxide more stable than another oxide in bulk may be less stable in nanoscale or aqueous environments. These complexities seem to be rather conducive for synthesis of oriented assemblies and mesocrystals. Penn et al.'s method of growing goethite nanorods from ferrihydrite particles[15] serves as an example of exploiting such cross-overs. By understanding the stability of the various phases at different size scales, the synthesis conditions can be changed to manipulate the precursor phases in crystal formation by non-classical growth modes. The following excerpt from Navrotsky's paper [20] stresses on this importance - "Thus, a strategy for making a given polymorph in the laboratory, and one that may be used by organisms as well, is to control the size of the initial crystal (typically by controlling concentration of reactants, ionic strength, and organic and inorganic additives) to precipitate the desired polymorph with a relatively uniform size distribution within the size range in which that polymorph is stable and then aggregate and coarsen the particles without phase transformation." [20]

1.2.3 Low temperature solution deposition of metal oxide thin films:

Over the years, several techniques have been used for the deposition of metal oxide thin films. These can be broadly classified into a) vacuum based techniques such as chemical vapor deposition (CVD), physical vapor deposition (PVD) etc. and, b) solution based techniques such as chemical bath deposition (CBD), electrochemical deposition, electroless deposition, sol-gel processing, etc.[21] Solution based techniques are preferred for reasons of low equipment costs, relatively low toxicity of chemicals, low temperatures of synthesis, larger range of substrates and in many cases, lack of requirement for post-processing heat treatments. Some of their disadvantages include lesser control over composition, microstructure and growth rates as compared to vapor phase techniques. Despite these, there has been an increasing interest in recent years to deposit oxide films using solution based techniques owing to the ability to deposit over large areas at low costs [22].

Niesen and Deguire[22] classified low temperature solution techniques used for oxide deposition into the following categories:

1. Chemical Bath Deposition (CBD): This technique refers to deposition of solid oxide films in single or multiple immersions by adjusting pH, temperature or chemistry of solutions. A wide variety of oxides have been deposited using this technique including TiO_2, ZnO, CeO_2 etc. [22] Techniques such as ferrite plating and liquid flow deposition (LFD) that have been used to deposit spinel ferrites (magnetite and NiZn ferrites) and other iron oxides have been described as variants of this process. Four main reaction steps were proposed to be involved in deposition of oxide films by CBD[22]. These were a) equilibrium between complexing agent or ligand (if any) and water and formation of metal-ligand complex, b) dissociation of water, c) displacement of ligands from the metal-ligand complex by hydroxyls and d) deprotonation to form oxide.
2. Liquid Phase Deposition (LPD): This refers to the technique of depositing oxides by the hydrolysis of metal fluoro-complexes using boric acid or aluminium metal.
3. Successive Ion Layer Adsorption and Reaction (SILAR): This refers to the growth of films by successive and alternate immersions of the substrate into metal salt solutions and hydrolyzing solutions.
4. Electroless deposition: This refers to an electrochemical deposition carried out at sensitized substrates without the involvement of external electrical sources and involved a change of oxidation state of the metal.

Chemical solution deposition of magnetite and other spinel ferrites:

Polycrystalline spinel ferrite $(M, Fe)_3O_4$ film deposition from chemical solutions was demonstrated by Abe et al. in 1983 using what they referred to as “ferrite plating”[23]. This was a broad term used for a variety of techniques developed by Abe’s group and included electroplating and electroless plating approaches to deposit films at 24-100ºC. The overall reaction scheme for deposition was essentially similar to that of CBD described above. However, ferrite plating involved oxidation of the main metal, iron from Fe^{2+} to Fe^{3+}. The oxidizing agent could be air, anodic current (electroplating) or dissolved reagents such as sodium nitrite, hydrogen peroxide etc. Equation 1.3 summarizes the ferrite formation reaction[24].

$$xFeOH^{2+} + yFeOH^{+} + zMOH^{(n-1)+} + OH^{-} \rightarrow (Fe^{3+}Fe^{2+}M^{n+})_3O_4 + 4H^{+} \quad \text{- (1.3)}$$

$$where\ x + y + z = 3\ and\ M = Fe, Cu, Ni, Co, Zn, Cr, Al\ etc$$

The first ferrite plating set up developed by Abe et al.[25] involved the use of either air (electroless) or anodic current (electroplating) to oxidize Fe^{2+} to Fe^{3+}. Plating was carried out in a single solution (dissolved salts of metals) reaction set up. Electroless plating allowed the use of a variety of substrates such as metals, polymers, etc., whereas, electroplating required the use of only metals. The substrate was completely immersed in the solution. A variation of this method, called the 'reactor' method involved the use of two separate solutions for the metal source (reactant) and oxidizer. The latter consisted of an oxidizing agent such as $NaNO_2$ and a pH buffer such as CH_3COONH_4 [24]. Next, they developed an ultrasound-enhanced plating technique [26], in which the substrates were placed in a mixture of reactant and oxidant solutions, followed by the application of low frequency ultrasound.

Subsequently, Abe et al. turned their attention from static solution based deposition methods to flow-based methods. This was likely due to static solutions having a self-limiting effect on thin film growth. Among the flow techniques developed were thin liquid-film method (described by other groups as liquid flow deposition[27] and involved flowing reactant solutions over a substrate), spin coating (dripping solutions on a rotating substrate) and spin spray plating or deposition (spraying solutions on a rotating substrate) [28]. The spin-spray deposition (SSD) method was found to be particularly productive for deposition of high quality films over large area substrates[24].

SSD involved spraying reactant and oxidant solutions onto a rotating substrate that was heated simultaneously[28]. Typical temperatures used were 70-90ºC [28-30]. The reactant solutions generally consisted of metal chlorides ($FeCl_2$, $NiCl_2$, $ZnCl_2$ etc.). The oxidant solutions were made up of sodium nitrite ($NaNO_2$) and ammonium or potassium acetate (serving as pH adjuster). The solutions were atomized using N_2 gas. A schematic of the set up developed by Abe et al. is illustrated below in Figure 1.5. This process enabled deposition onto a wide range of substrates including flexible polymers such as polyether ether ketone (PEEK), polyimide etc. Consequently, it has received increasing attention for the deposition of NiZn and NiZnCo ferrites to be used for electromagnetic applications[3, 30, 31]. They exhibit exceptional magnetic properties owing to their fine microstructures (typically nanosized features owing to the low process temperatures) [3, 31].

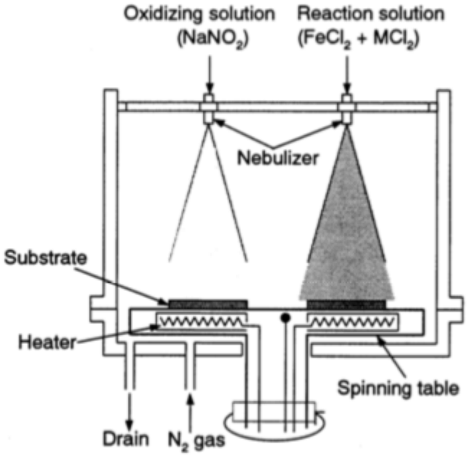

Figure 1.5 Spin spray plating[24]

Crystal structure of magnetite:

Magnetite (Fe_3O_4) crystallizes in the cubic inverse spinel structure. Its structure type is AB_2O_4 and belongs to the Fd-3m space group. Its crystal structure is made up of a cubic close packed lattice of oxygen (O^{2-}) ions with all Fe^{2+} ions occupying the octahedrally co-ordinated sites (A sites) and the Fe^{3+} ions distributed evenly between the tetrahedral (B sites) and octahedral sites (A sites). The lattice parameter is a=8.39A°.

Chapter 2

EXPERIMENTAL METHODOLOGY

This chapter describes the specifics of the deposition reactor and experimental procedures involved in the growth of magnetite films. An aqueous deposition method called spin-spray plating or spin-spray deposition (SSD) was used to deposit magnetite films onto flexible polyether ether ketone (PEEK) substrates at low temperatures of 90-95°C. *Ex-situ* characterization carried out on the samples included X-ray diffraction (XRD) for phase identification and purity analysis, scanning electron microscopy (SEM) for imaging film microstructure, transmission electron microscopy (TEM) for high resolution imaging of nanoscale features and analysis of crystallinity.

2.1 Spin Spray Deposition:

The spin spray deposition is an aqueous solution deposition technique that involves hydrolysis of precursor salt solutions at low temperatures (70-100°C). The technique was developed in the 1980's by Matsushita, Abe et al. [29] and involved several process variables (liquid flow rate, platen rotation rate, choice of substrates, temperature etc.) that can be adjusted to change the phase, composition and microstructure of the deposited films. Generally, it involved rotating substrates on a heated platen under two liquid sprays, which when combined reacted to deposit films on the substrate. The residual liquid was flung off the platen due to centrifugal force.

The spin disc reactor (SDR) used for the experiments in the current study was designed and constructed by Dr. Nicole Ray at ASU. [31]. It consisted of a rotating stainless steel platen nine inches in diameter. The platen was resistively heated to low temperatures (upto 300°C) and contained inside a gas-purged stainless-steel chamber. The chamber was covered with a lid made up of polymethyl methacrylate (PMMA) and had eight ports for liquid solution and gas feed using PEEK (polyether ether ketone) Miramist nebulizers from Burgener Research Inc. The nebulizers were placed such that they were 6” above the platen during deposition. Precursor solutions were fed continuously to the nebulizers by a Gilson peristaltic pump. Nitrogen gas was scrubbed using a gettering furnace and fed along with the liquid solutions into the nebulizers to create the atomized spray. The chamber also had two ports at the bottom that serve as outlets for liquid waste that spins off the platen and an additional port for nitrogen gas circulation. Process variables included speed of rotation of platen, liquid feed rate (or pump speed), temperature of the platen and solution chemistry. The temperature and speed of rotation of platen were recorded during the experiment using National Instruments compact DAQ device and LabView Signal Express. A schematic of the spin spray deposition reactor is shown in Figure 2.1.

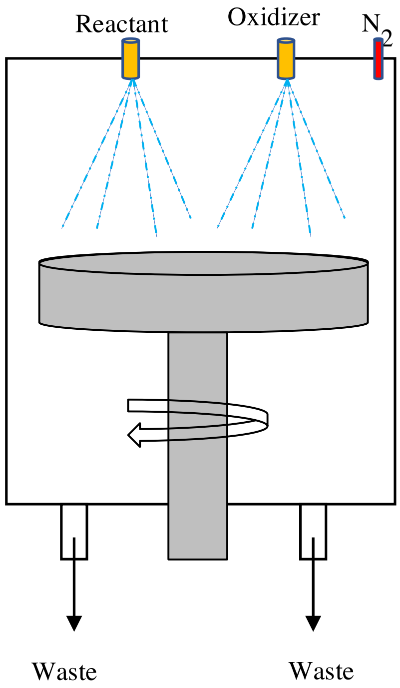

Figure 2.1: Schematic of spin spray disc reactor

Figure 2.2: Experimental set up for spin spray deposition (SSD)

1,2 – Reactant and oxidant solution reservoirs

3 – Gilson peristaltic pump

4 – Waste collection unit

5 – Spin spray reactor

6 – Helmholtz coils

7 – Scrubbed N_2 gas supply

8 – Platen Rotation controller

9 –Platen temperature controller

Deposition could be carried out on a variety of substrates including glass, silicon, quartz and polymer substrates like polyether ether ketone (PEEK). In this study, magnetite was deposited on plasma treated PEEK substrate. The PEEK substrate had a 20% mineral loading to better match the thermal expansion coefficient of magnetite.

Before every deposition experiment, the surface of the platen was cleaned thoroughly with deionized water followed by acetone. The PEEK substrate was then attached to the platen using Kapton tape and the lid (with the nebulizers attached to it) was placed on top to close the reactor. The platen was then heated to the desired temperature and rotated at desired speeds (60-200 rpm). N_2 gas feed through the nebulizers was started at this point in order to purge the chamber. The precursor solutions were then fed using the peristaltic pump into the nebulizers. Solution flow rates were typically 10-30 ml/min for both precursors. The carrier N_2 gas pressure was between 44-50 psi. The solutions sprayed onto the rotating substrate and over the course of time, film growth occurred on the substrate. Use of scrubbed nitrogen was of utmost importance as magnetite at ultra-small particle/grain sizes has a strong tendency to undergo oxidation to maghemite (γ-Fe_2O_3) or hematite (α-Fe_2O_3).

Two separate reservoirs were maintained to house the aqueous solutions to be fed into the reactor. The first solution, called the reactant (metal chloride) consisted of ferrous chloride ($FeCl_2.4H_2O$) dissolved in deionized (DI) water. The second solution, called the oxidant consisted of sodium nitrite ($NaNO_2$) that served as an oxidizer of Fe^{2+} to Fe^{3+}. The pH of the oxidant solution was controlled using pH adjusters (base). For maintaining the pH within a broader range of 6-9, mixtures of glacial acetic acid (CH_3COOH) and ammonia (28% NH_3) or salts like ammonium acetate (CH_3COONH_4) and potassium acetate

(CH_3COOK) were added to the oxidant solution. For tighter control of pH in the range of 8.0-8.6, sodium bicarbonate was added to the oxidant solution. Much of this study involved the use of the latter. The type of pH adjuster used determined the microstructure of the films. The use of ammonia and acetate based oxidant solutions gave dense and textured polycrystalline microstructures (with columnar growth of grains). On the other hand, the use of $NaHCO_3$ gave rise to microstructures with hierarchical features of several orders. The reactant chloride solution pH was between 3.8 – 4.5.

At the end of a deposition run, the heating of the platen was stopped and pure DI water was fed through all the nebulizers to wash the surface of the film. This was done for 15 mins. After the film was washed and cooled to room temperature, the platen rotation was stopped and the film was carefully removed from the platen.

2.2 Characterization Techniques:

2.2.1 X-ray Diffraction:

X-ray diffraction (XRD) was routinely used to analyze phase purity and the crystal structure of the deposited films. Crystals comprise regular arrays of atoms in three-dimensional space. X-rays being electromagnetic radiation (waves) can be scattered by atoms owing to their electrons. Most of the scattered waves from the crystal undergo destructive interference, and cancel each other. However, a fraction of the scattered waves interferes constructively in specific directions that satisfy the Bragg's law given by,

$$n\lambda = 2d\sin\theta \quad \text{- (2.1)}$$

where n is any integer, λ is the wavelength of the X-rays, d is the spacing between the diffracting planes of atoms and θ is the angle of incidence of the radiation (Figure 2.3).

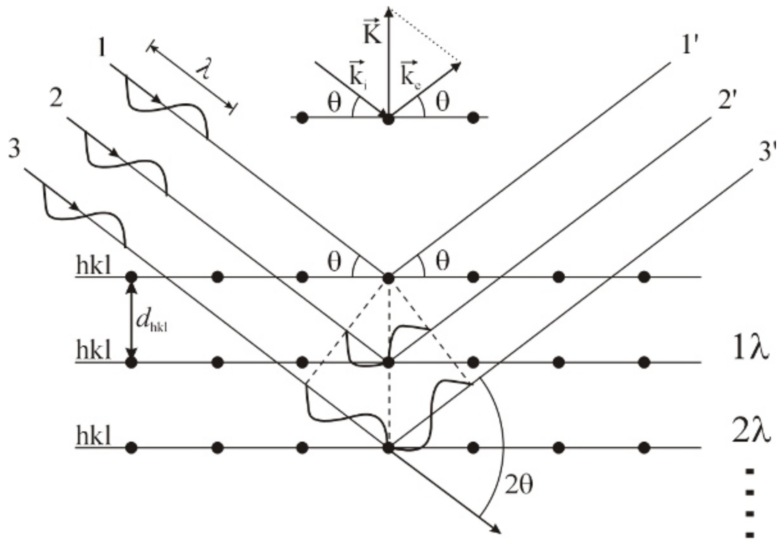

Figure 2.3: Schematic showing principle of X-ray Diffraction. Waves 1, 2 and 3 are incident X-Ray radiation while 1', 2' and 3' are scattered waves from the crystal. hkl denotes the Miller indices of the diffracting planes of the crystal [32].

In an X-ray diffractometer, a sample is irradiated with X-rays from a source. Either the sample or the source is moved through a range of angles and the scattered beam is collected by a detector. The intensity of the radiation collected from the detector is amplified and recorded. The data is commonly recorded in the form of an x-y plot with 2θ on the x-axis and peak intensities on the y-axis.

X-Ray diffraction analysis of the deposited films was carried out using Siemens D5000 X-ray Diffractometer with cobalt K_α radiation (λ=1.78 $\overset{\circ}{A}$). Phase identification was carried out by analyzing the data from the diffractometer using MDI Jade9 software. Sub-micrometer sized particles cause broadening of the peaks. This peak broadening can be used to calculate the crystallite size using Scherrer's equation given by,

$$\tau = \frac{K\lambda}{\beta cos\theta} \qquad \text{- (2.2)}$$

where τ is the grain size, K is a dimensionless shape factor (typically 0.9), λ is the wavelength of the X-rays, β is the line broadening at full width half maximum (FWHM) and θ is the Bragg angle in degrees.

Jade9 software had additional plugins that enabled calculation of particle size from peak broadening using the Scherrer equation.

2.2.2 Electron Microscopy:

Electron microscopy was used to analyze the microstructure and morphologies of the magnetite films. Electron microscopes are powerful characterization tools that enable imaging of specimens down to the nanoscale. They have much higher resolving power than normal optical light microscopes. This is due to the extremely small wavelengths of high energy electrons (given by the deBroglie wavelength) which is typically of the order of a few picometers. Visible light has much larger wavelengths between 400 nm-700 nm. In this study, two types of electron microscopes were used- Scanning Electron Microscope (SEM) and Transmission Electron Microscope (TEM).

Scanning Electron Microscopy:

Scanning Electron Microscopy (SEM) was used to analyze the microstructure, morphology and particle/grain sizes of magnetite films.

Scanning electron microscope (SEM) is a type of electron microscope with the ability to produce high resolution images of the surface microstructure of a sample using a focused beam of high energy electrons (0.2 keV to 40 keV). A variety of signals are generated upon the interaction of the electrons with the sample. These signals can be collected using appropriate detectors and analyzed to obtain valuable information regarding the sample topography and composition. Figure 2.4 shows a schematic of a typical SEM. The electron beam source or the electron gun are of three main types: tungsten filament cathodes, lanthanum hexaboride (LaB_6) cathodes or field emission guns (FEG). The electron gun produces a beam of electrons inside a high vacuum chamber where the samples for analysis are placed. This beam is collimated and focused by electromagnetic condenser and objective lenses. The beam then passes through electromagnetic deflection coils which enable the beam to be rastered or scanned along the surface of the sample. The electrons in the primary electron beam, on interacting with the sample lose energy by scattering and absorption within a small volume of the sample called the interaction volume (Figure 2.5). In the primary imaging mode of the SEM, the secondary electrons (low energy <50 eV) ejected from the sample (due to inelastic scattering) surface (<50nm) are detected using a secondary electron detector. The signal from the detector is amplified by a photomultiplier which is then displayed as variations in brightness on a computer. The position of the beam on the sample and the resulting signals are correlated and hence the image obtained gives a mapped distribution of the signal intensities from the scanned area of the sample. The SEM can also be used for backscattered electron imaging and compositional analysis using energy dispersive X-ray spectrometer.

The SEM used in this study was an XL-30 Environmental FESEM (FEI) with a FEG source. Since the PEEK substrate used in our study and magnetite were relative poor electrical conductors, samples were coated with gold (using a sputtering system) before

SEM analysis to prevent charging. Feature sizes (particle/grain size) and thicknesses were measured by analysis of captured images in the *ImageJ* software. Thicknesses of dense films were measured using images of fractured surfaces that revealed the cross-section of the film. The latter was created by mild scratching of the films with a razor blade. Porosity analysis for films was carried out using image thresholding tools within *ImageJ*.

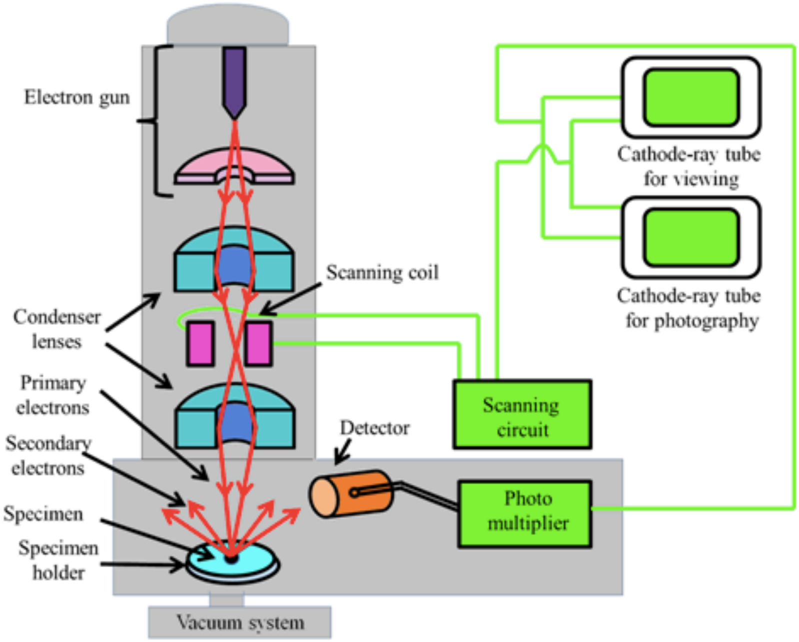

Figure 2.4: Schematic of a Scanning Electron Microscope (SEM)[33]

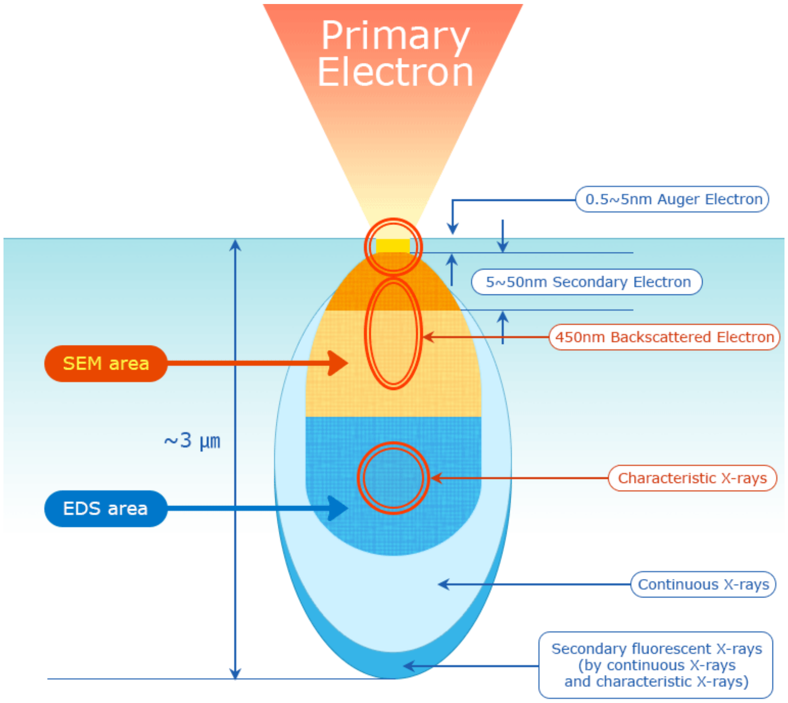

Figure 2.5: Electron-sample interaction volume[34]

Transmission Electron Microscopy:

Transmission electron microscopy (TEM) was used to analyze nanoscale and atomic scale features of the microstructure of magnetite films.

Transmission electron microscopy (TEM) is an imaging technique in which high resolution images of a specimen are obtained by transmitting a beam of electrons through a specimen (Figure 2.6). The sample needs to be ultrathin (<100nm) for transmission of the electrons through it. The final image obtained is a magnified version of the sample. This magnification is achieved by the passage of the electron beam through a series of electromagnetic lenses. This image is focused onto a fluorescent screen, a layer of photographic film or a detector like a charge coupled device (CCD). The energy of the electron beam used in a TEM (typically 60-300keV) is significantly higher than that of an

SEM. Hence, the deBroglie wavelengths of the electrons are much smaller and resolving power of TEMs are much higher. TEM can be operated in direct imaging mode or in electron diffraction mode. The former is used to study particle morphology, grain sizes, lattice defects etc. while the latter is used to study crystallographic structure of the material. In imaging mode, at lower magnifications, image contrast is due to differential absorption of electrons by the specimen due to compositional or thickness variations within it. At higher magnifications (High Resolution Transmission Electron Microscopy-HRTEM mode), the contrast is due to differences in phase of the electron waves after interaction with the specimen. This contrast is called phase contrast. HRTEM mode can also be used to study crystal structure and lattice defects.

TEM analysis in this study was carried out largely in HRTEM mode. Electron diffraction was also used to study crystallographic structure. Samples were prepared by first scratching magnetite deposit off the PEEK substrates using either a diamond tip or Teflon spatula. This deposit was then suspended in deionized (DI) water, sonicated and further diluted by DI water. A drop of this suspension was then placed on a 3 mm 200 mesh holey carbon coated copper TEM grid. TEM analysis was carried out primarily on a FEI Titan 300/80 aberration corrected TEM (operated at an accelerating voltage of 300 keV or 80 keV for samples prone to beam damage) and a Philips CM200-FEG TEM (operated at an accelerating voltage of 200 keV). TEM image analysis was carried out using *Gatan Digital Micrograph* software package. This included feature (particles/grains) size measurements and Fast Fourier Transform (FFT) analysis of HRTEM images to obtain crystallographic information (lattice spacing of planes).

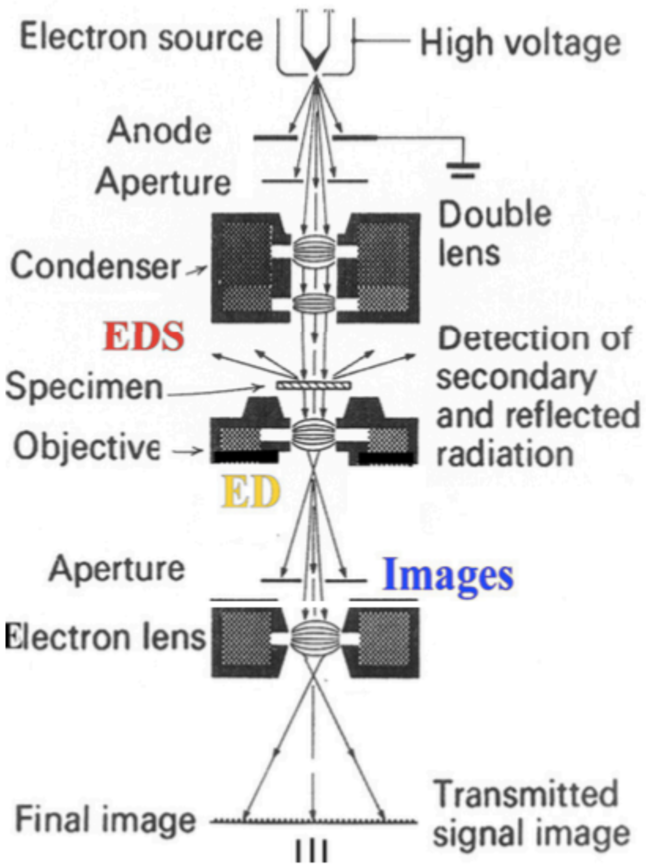

Figure 2.6: Schematic of a Transmission Electron Microscope (TEM)[35]

Chapter 3

DEPOSITION OF MAGNETITE FILMS USING SPIN SPRAY DEPOSITION

This chapter describes the fundamentals of the aqueous chemistry employed to deposit magnetite films using the spin spray deposition technique. A novel synthesis protocol was developed during this study that has led to a facile method for depositing films with self-assembled hierarchical microstructures. A major advantage of this chemistry is that it contained no organic additives nor involved post-deposition treatments to bring about the observed microstructures.

In all our experiments, the reactant solution (metal source) always consisted of ferrous chloride ($FeCl_2.4H_2O$) dissolved in DI water. The oxidant solution primarily consisted of sodium nitrite ($NaNO_2$) to help oxidize Fe^{2+} to Fe^{3+}. However, the choice of base in the oxidant solution was varied. The details of these variants are described in the sections below.

3.1 Deposition of magnetite films using ammonia/acetate based oxidant solutions:

Magnetite films were first synthesized using various solutions containing ammonia and acetate ions to adjust the pH of the oxidant solution. The oxidant ($NaNO_2$) concentration was maintained between 4.35 – 5 mM. Depending on the concentration and source of acetate/ammonia used, the pH of the oxidant solution was adjusted between 6 and 8.5. This was done using potassium acetate, ammonium acetate or mixtures of glacial acetic acid (CH_3COOH) and ammonia solution (28% NH_3). The concentration of the pH adjuster in the oxidant solution was typically 30-70 mM. The reactant solutions used in these experiments consisted of 16.7 mM ferrous (II) chloride solution. These experiments were carried out at 90°C and a platen rotation rate of 90 rpm. The precursor solutions were sprayed using a total of eight nebulizers, four of which sprayed the reactant solution while the rest sprayed the oxidant solution. Each nebulizer had a flow rate of 8 ml/min.

Magnetite films deposited using this chemistry typically had a lustrous grey appearance attributed to nanocrystalline magnetite (Figure 3.1). This did not change with the source of the acetate or ammonia ions nor their concentrations. The films adhered to the substrate very well. Physical handling of the films did not affect the deposit.

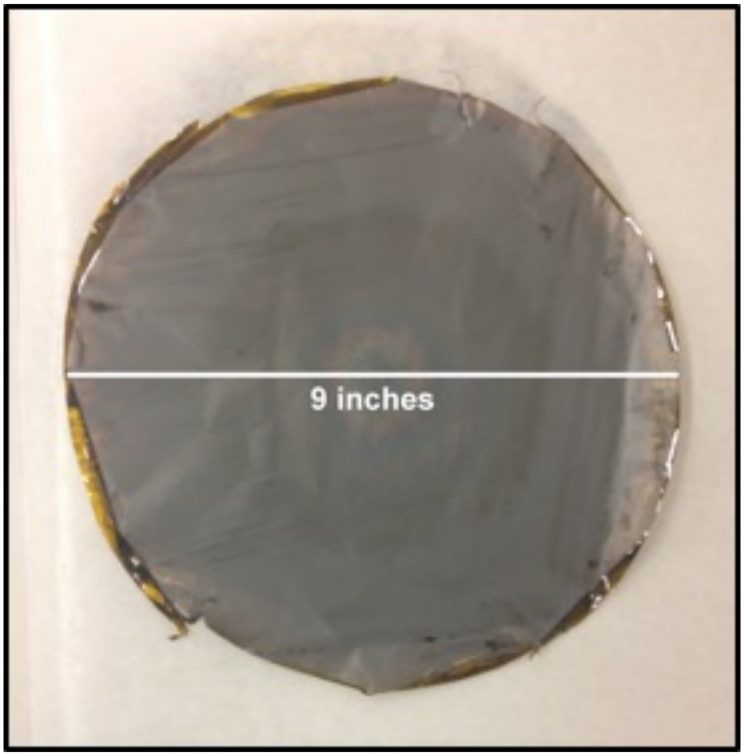

Figure 3.1 A typical magnetite film deposited in 30 mins using ammonium/acetate based oxidant solution

SEM analysis of magnetite films deposited using ammonia/acetate buffers showed dense microstructures consisting of mosaic grains, which are polycrystalline assemblies of smaller spherical nanoparticles. These grains took various shapes that included octahedrons, spheres, cubes depending upon the source of acetate and ammonia ions and the pH of the oxidant solution used in the synthesis. Their size was generally between 100 nm and 500 nm. The smaller nanoparticles were in the size range of 15-30 nm and sometimes larger. Some of the observed morphologies are presented in the images below (Figure 3.2).

Cross-sectional images of fractured surfaces of the film showed columnar texturing within the films (Figure 3.3). It is worth noting these columns were made of smaller nanocrystallites.

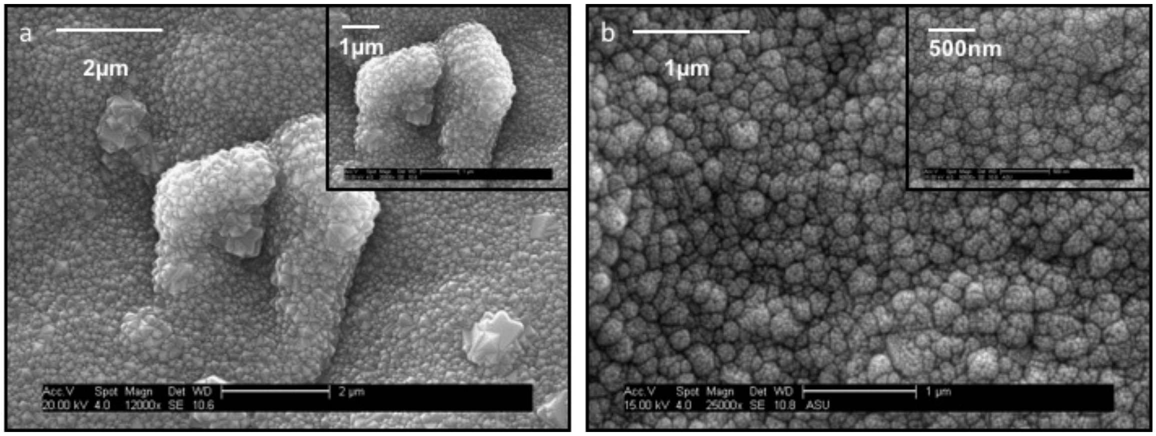

Figure 3.2 SEM images of magnetite films showing dense polycrystalline microstructure. Insets show that each mosaic grain is made of several spherical nanoparticles

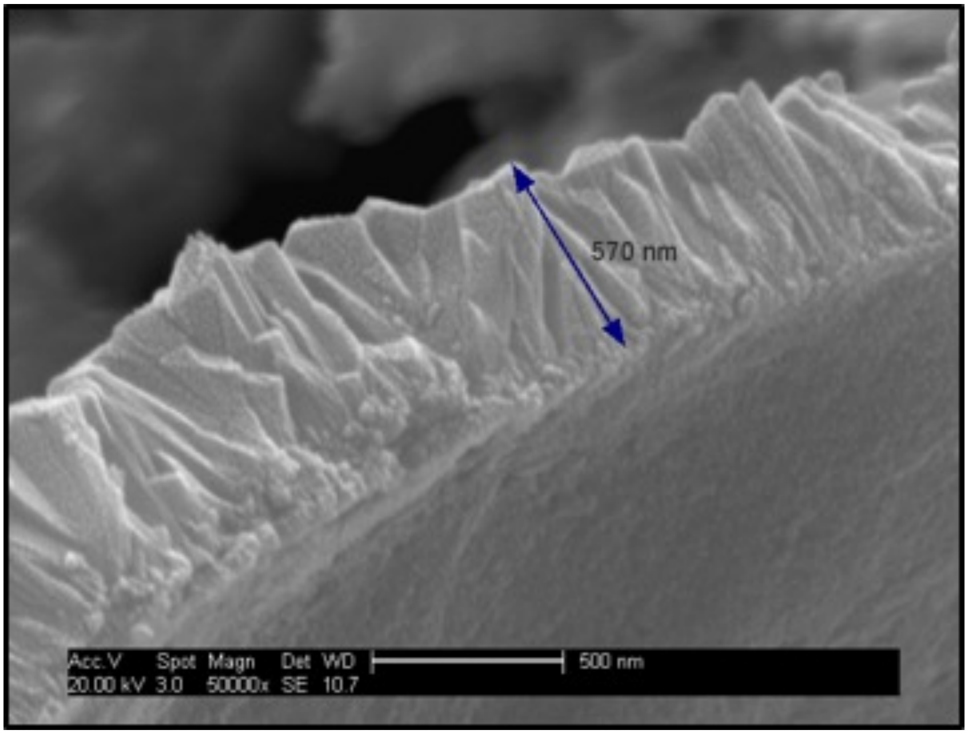

Figure 3.3 Cross-section SEM images of a magnetite film showing columnar growth.

These observations were in agreement with Abe et al.'s work [28]. They [28] first used the acetate chemistry while depositing magnetite films using spin spray deposition (SSD) in order to increase uniformity of the film and control deposition rate. They also suggested that the acetate (CH_3COO^-) ions prevented the precipitation of $Fe(OH)_2$ which would lead to deterioration in surface smoothness.

3.2 Deposition of magnetite films using sodium bicarbonate based oxidant solutions:

As a part of this study, a new synthesis protocol was developed and involved the use of a weaker base to adjust the pH of the oxidant solution. Based on several trials, sodium bicarbonate was chosen as it offered a tighter control of the pH (typically 8.0 to

8.6) for a wider range of concentrations used. In preliminary experiments, the oxidant solution consisted of 4 - 5 mM $NaNO_2$ and 100 mM $NaHCO_3$. The reactant solution was made up of 16.7 mM $FeCl_2$.The rest of the process parameters were the same as in section 3.1.

Magnetite films deposited under these conditions were jet-black in color (Figure 3.4). They lacked luster and were opaque. The films did not adhere to the substrate as well. They generally flaked off the substrate with only moderate physical handling.

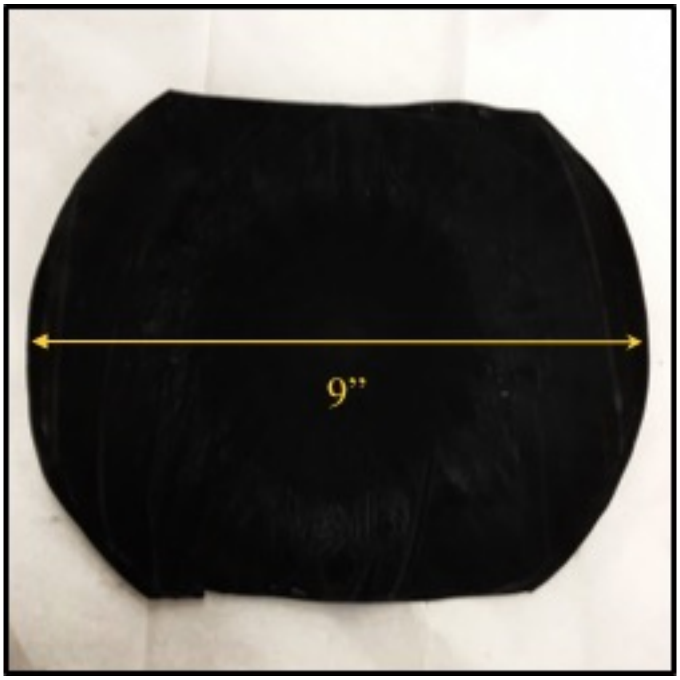

Figure 3.4 A typical magnetite film deposited in 30 mins using sodium bicarbonate buffered oxidant solution

SEM analysis of the films revealed a porous microstructure. It was made up of loose 5-10 μm sized clusters (Figure 3.5a) made up of several nanoflakes. The nanoflakes were roughly 1 μm x 1 μm in size and 35-50 nm thick (Figure 3.5b). Secondary features in the form of smaller equiaxed polycrystalline (mosaic) structures were also observed. Their sizes varied between 100-500 nm. Grain boundaries were clearly visible within these equiaxed structures (Figure 3.5c), showing that they were made up of smaller nanoparticles. These films were considerably thicker with thickness ranging between 5-15 μm.

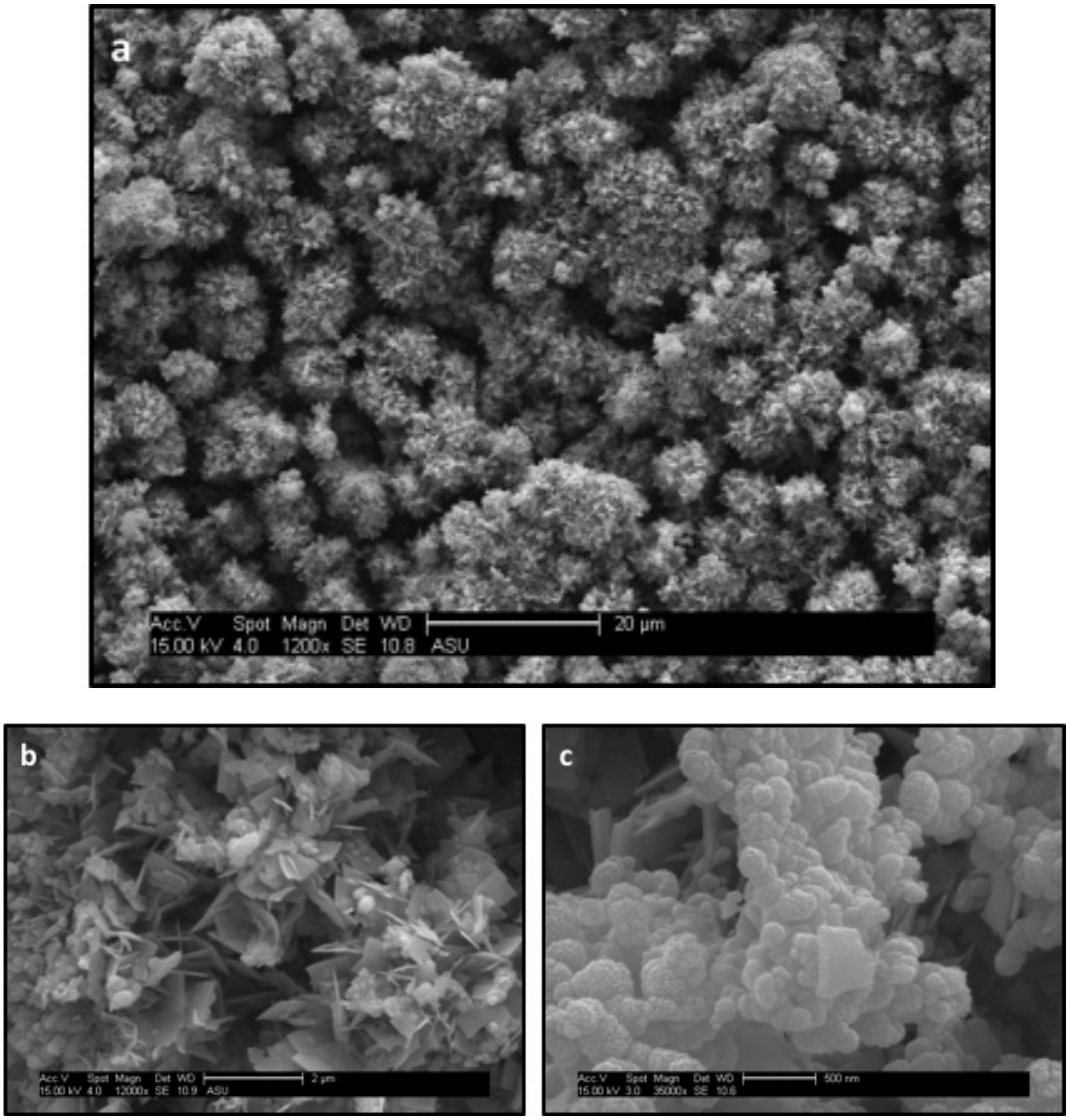

Figure 3.5 SEM images of magnetite film deposited using bicarbonate buffered oxidant solution (a) low magnification image showing micron sized clusters, (b) higher magnification image of clusters showing nanoflakes and (c) equiaxed polycrystalline structures

Additionally, $NaHCO_3$ based oxidant solutions could also be used to deposit lustrous, dense and well-adhered magnetite films. Such films were obtained when the concentration of $FeCl_2$ in the reactant solution or $NaHCO_3$ in the oxidant solution or both were decreased (This will be discussed in detail in subsequent chapters). Their microstructures were comparable to those described in section 3.1.

3.3 Reaction chemistry for the spin spray deposition of magnetite:

3.3.1 From ammonia/acetate based oxidant solutions:

Abe et al. [30, 36, 37] and Ray et al[3, 31] worked extensively on the deposition of ferrite films using the chemistry (ammonia/acetate based oxidant solutions) described in section 3.1. In their studies, Abe et al. [24, 38] proposed an overall principle for ferrite formation involving a sequential set of reactions. They proposed that ferrite films grow as a result of chemical reactions that occur during the sequential exposure of reactant and oxidant solutions. As per this model, the steps involved in the formation of magnetite (illustrated in Figure 3.6) can be summarized as follows:

1. Adsorption of OH^- ions (from the oxidant solution) on the substrate followed by adsorption Fe^{2+} ions leading to the release of H^+.
2. Oxidation of some of the Fe^{2+} ions to Fe^{3+} by $NaNO_2$ in the oxidant solution, which can be expressed as,

$$Fe^{2+} + NO_2{}^{-} + 2H^{+} \longrightarrow Fe^{3+} + \mathrm{NO} + H_2\mathrm{O} \quad \text{-}(3.1)$$

3. More adsorption of Fe^{2+} ions on the surface layer of the pre-adsorbed Fe^{2+} and Fe^{3+} ions.

4. Formation of ferrite layer following hydrolysis and release of H^+. This can be expressed as

$$Fe^{2+} + 2Fe^{3+} + 4H_2O \longrightarrow Fe_3O_4 + 8H^+ \text{ - (3.2)}$$

An overall reaction leading to the formation of magnetite can be expressed as follows:

$$3Fe^{2+} + 2NO_2{}^{-} + 2H_2O \longrightarrow Fe_3O_4 + 2NO + 4H^+ \text{- (3.3)}$$

In addition, Abe et al. proposed that in actual experiments, the above steps occur jointly.

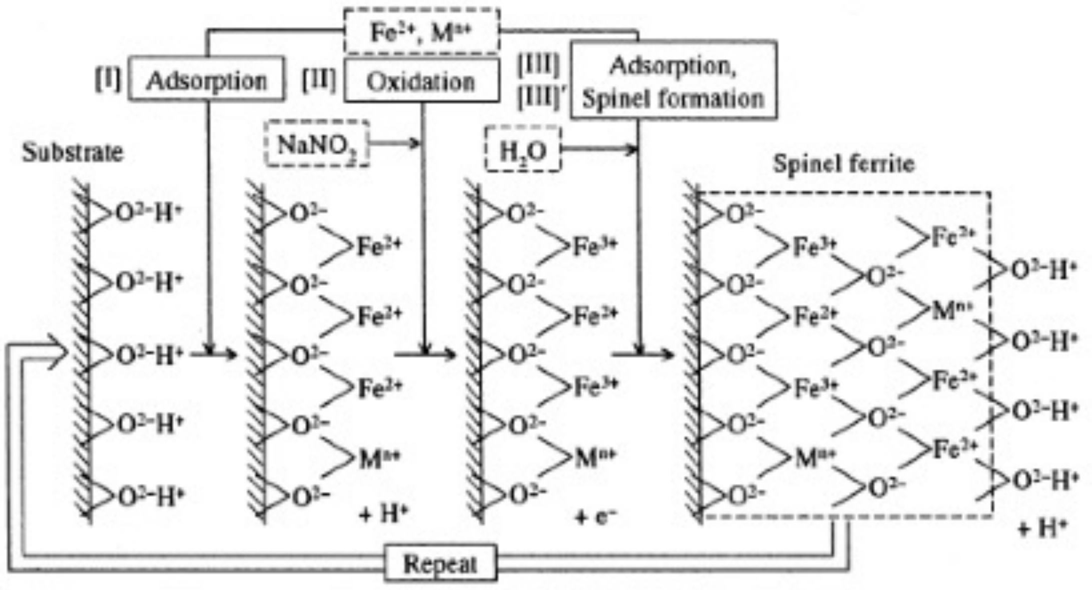

Figure 3.6 Formation of magnetite by spin spray deposition as described by Abe [24]

This model served well to describe the deposition of dense ferrite films using the ammonia/acetate chemistry. It was especially successful in explaining the columnar growth of films perpendicular to the substrate and their slow growth rates (10-20 nm/min). This is due to the involvement of adsorption of metal and hydroxyl ions prior to oxide formation.

3.3.2 From bicarbonate based oxidant solutions:

As a part of this study, a sequence of time-resolved experiments (details of which will be explained in subsequent chapters) were carried out and have led to the formulation of alternate mechanisms for the deposition of magnetite films. These mechanisms were found to operate when the pH of the oxidant solution was controlled by bicarbonate or alternately carbonate (not a part of our current study) and involved the formation of intermediate solid precursor phases to magnetite.

Magnetite crystallization through oxy-hydroxide precursors:

One of the unique characteristics of the Fe-H_2O system is the involvement of an exceptionally large number and variety of stoichiometries available for iron oxides and (oxy)hydroxides which play a vital role in the pathways taken to obtain the final product[39, 40]. These pathways depend on a variety of factors such as pH, supersaturation, redox chemistry and other kinetic factors. The final product(s) (oxide or oxyhydroxide) obtained is (are) extremely sensitive to the aforementioned conditions. The complications of the aqueous chemistry of iron has been attributed to the very low solubility of both $Fe^{2+}$and Fe^{3+} ions and the involvement of a variety of hydrolyzed species (oxo-hydroxo complexes of Fe) in solution depending on the pH [41, 42]. This particularly bears a huge influence in the formation of magnetite through aqueous solution pathways. Ahn et al. [40] have demonstrated the involvement of intermediate solid phases (amorphous or crystalline) which subsequently transform into the magnetite. Such pathways and intermediate phases also bear an important influence on the morphology of the magnetite obtained at the end.

Green rust compounds as a precursor to magnetite:

Green rusts are a class of Fe-bearing oxy-hydroxy compounds that belong to the layered double hydroxides (LDH) family of compounds that have the general formula $[M^{II}_{(1-x)} M^{III}_{x} (OH)_2]^{x+} \bullet [(x/n)\ A^{n-}\ (m/n)\ H_2O]$ (M being Fe in this case). An example LDH compound is illustrated in Figure 3.7. They are derived from the layered brucite type structure. The layers are positively charged owing to the presence of both Fe(II) and Fe(III) cations. These cations occupy the center of octahedrons with OH^- at its six apices. The anions (A^{n-}) situated between these layers maintain the electro-neutrality of the compound. Green rusts have been broadly classified into two types depending on the nature of the anions in the interlayers. Green rusts I (GRI) consist of either Cl^- or CO_3^{2-} ions while green rusts II (GRII) consist of SO_4^{2-} ions[41, 42]. These compounds have been shown to form during the partial oxidation of Fe^{2+} ions in weakly basic solutions (pH=7-9). The green rusts have been studied by various groups[39, 43-45] and have been recognized as precursors to magnetite. Mirabello et al. [39] showed with the help of time-resolved cryo-TEM analysis that during the synthesis of magnetite nanoparticles by partial oxidation of Fe^{2+} solutions, magnetite formation was preceded by the formation of green rusts that eventually underwent transformation.

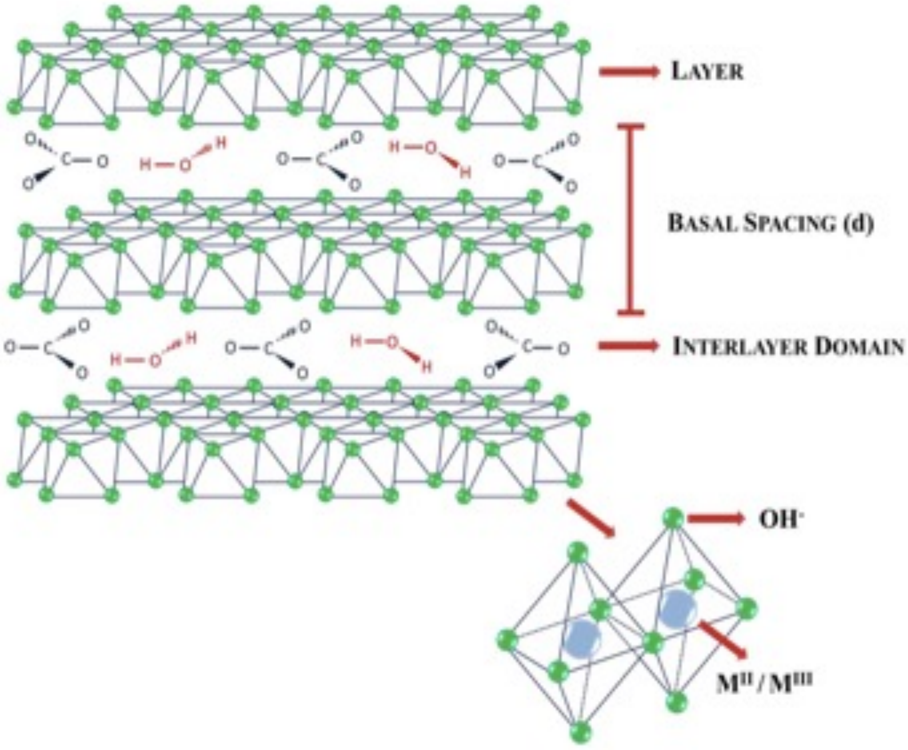

Figure 3.7 General structure of a layered double hydroxide (LDH) [46]

Taylor[45] showed that small amounts of Fe(III) in solutions containing Fe(II) and CO_3^{2-} and at near neutral pH can induce the precipitation of Fe(II)-(III) hydroxycarbonate or GR(CO_3) (belong to green rust type I class) at 25°C. Fe(II)-(III) hydroxycarbonate belongs to the pyroaurite group of minerals and in its stoichiometric form has a chemical formula given by $Fe^{II}_4 Fe^{III}_2 (OH)_{12} CO_3$. While studies by Taylor and other authors[43, 44, 47-49] have shown the transformation of green rust to magnetite, the description of nature of the transformation has been varied – with some authors suggesting solid state transformation, while others dissolution and re-precipitation. A noteworthy detail is that all the aforementioned studies involve growth of magnetite from bulk solutions.

In our studies on SSD of porous magnetite films with the bicarbonate based oxidant solutions, the presence of GR(CO_3) was observed in the initial stages of film deposition (discussed in detail in subsequent chapters). With time, the green rust phase transformed to magnetite. Based on these observations, the following reactions have been proposed to be involved in the formation of magnetite:

$$Fe^{2+} + NO_2{}^{-} + 2H^{+} \longrightarrow Fe^{3+} + \mathrm{NO} + H_2\mathrm{O} \qquad \text{-(3.4)}$$

$$HCO_3{}^{-} \longrightarrow CO_3{}^{2-} + H^{+} \qquad \text{-(3.5)}$$

$$4Fe^{2+} + 2Fe^{3+} + CO_3{}^{2-} + 12OH^{-} \longrightarrow Fe^{II}{}_4Fe^{III}{}_2(OH)_{12}CO_3 \qquad \text{-(3.6)}$$

$$Fe^{II}{}_4Fe^{III}{}_2(OH)_{12}CO_3 + \tfrac{1}{3}O_2 \longrightarrow \tfrac{5}{3}Fe_3O_4 + Fe^{2+} + CO_3{}^{2-} + 6H_2O \qquad \text{-(3.7)}$$

Reaction 3.7 was proposed to occur in low oxygen environments by Ruby et al. [49].

Other iron oxides as precursors to magnetite:

Alternately, SSD of dense magnetite films with bicarbonate based oxidant solutions involved the formation of hematite (α-Fe_2O_3) in the initial stages of film deposition. Hematite is an iron oxide that crystallizes in the hexagonal lattice system and in its pure form comprises iron completely in its +3 oxidation state. With continued deposition, hematite underwent solid state transformation to a spinel structured maghemite (γ-Fe_2O_3). This spinel structured iron oxide consists of a slightly higher Fe^{3+} content than that present in stoichiometric magnetite and slightly lesser Fe^{3+} than in stoichiometric hematite. Maghemite, then transformed to magnetite. The proposed sequence of reactions has been detailed below.

$$Fe^{2+} + NO_2^{-} + 2H^{+} \longrightarrow Fe^{3+} + \mathrm{NO} + H_2\mathrm{O} \quad \text{- (3.8)}$$

$$HCO_3^{-} + H_2\mathrm{O} \longrightarrow H_2\mathrm{C}O_3 + OH^{-} \quad \text{- (3.9)}$$

$$2Fe^{3+} + 6OH^{-} \longrightarrow \alpha - Fe_2O_3 + H_2\mathrm{O} \quad \text{- (3.10)}$$

With time, a series of solid-state transformations occurred leading to the formation of magnetite. These transformations included structural re-arrangements as well as redox reactions.

$$\alpha - Fe_2O_3 \xrightarrow{Fe^{2+}} \gamma - Fe_2O_3 \xrightarrow{Fe^{2+}} Fe_3O_4 \quad \text{- (3.11)}$$

In spin spray deposition, all the reactions (nucleation and growth of crystals) are restricted to an almost two dimensional zone near the substrate as solution is continuously spun off the substrate due to centrifugal force exerted by rotating platen. Hence, the transformation of green rust to magnetite or hematite to magnetite (via maghemite) in SSD is purely solid state. Transformation through dissolution-reprecipitation would require the presence of bulk solution to dissolve into, which is unavailable in the SSD case. A more detailed description of these transformations and their role in the morphological evolution of magnetite films will be discussed in a Chapter 6.

3.4. Conclusions:

A set of preliminary experiments were conducted to deposit magnetite films using spin spray deposition. Two different solution chemistries differing primarily in the choice of base in the oxidant solution were used. The ammonia/acetate based oxidant solutions were previously studied by Abe et al. and Ray et al. and were shown to produce dense magnetite films that were lustrous and well adhered to the substrate. A second synthesis protocol was developed as a part of this study. This involved the use of bicarbonate based oxidant solutions and led to the deposition of porous and dense magnetite films with hierarchical morphologies.

The reaction chemistry involved in the deposition of films using the ammonia/acetate oxidant solutions was previously described by Abe et al. Alternate reaction schemes involved in the crystallization of porous and dense magnetite films are proposed in this study. The deposition of porous films involved the formation of an intermediate green rust iron hydroxycarbonate phase followed by its solid state transformation to magnetite. Dense magnetite films crystallized by transformation from hematite and maghemite precursor phases.

Chapter 4

PROCESS DEPENDENT MORPHOLOGIES OF MAGNETITE FILMS

As mentioned in Chapter 2, a salient feature of the spin spray deposition method is the availability of multiple variable process parameters that can influence the deposition of films. These parameters can be grouped into subcategories that affect a) the fluid flow of solutions and b) the chemical behavior of solutions.

Table 4.1 Spin spray deposition process parameters

Fluid flow parameters	**Chemical behavior of solutions**
I. Rotation speed of platen (rpm)	Choice of precursor solutions (reactant and oxidant)
II. Liquid feed rate (ml/min/nebulizer or number of nebulizers)	**III. Concentration of precursor solutions (mM)**
IV. Nebulizer configuration	pH of precursor solutions
Carrier gas (N_2) pressure (psi)	Temperature of platen (°C)
Substrate material	

Out of these, the effect of choice of base in the oxidant solution has already been described in Chapter 3. An additional variable that is not classified under these two categories is the deposition time. In this chapter, the effect of the parameters marked with roman numerals in Table 4.1 on the microstructure of magnetite films will be described.

The primary focus of this chapter is on the parameters that affect the fluid flow on the substrate. Towards the end of the chapter, the effect of chemical parameters will be examined.

The precursors used for all the experiments described in this chapter are solutions containing ferrous chloride for the reactant and solutions containing sodium nitrite and sodium bicarbonate for the oxidant.

4.1 Effect of process parameters affecting fluid flow:

4.1.1 Number of nebulizers and nebulizer configuration:

The initial goal was to deposit magnetite films with uniform microstructure on large area substrates. As in previous chapters, deposition was carried out on 9” diameter substrates. In order to achieve magnetite coverage over the entire area of the substrate, preliminary experiments were carried out with the use of eight nebulizers to spray the precursor solutions (four spraying reactant and four spraying oxidant). Their placement configuration (N-8) on the reactor lid is illustrated in Figure 4.1. The deposition conditions for these experiments are listed in Table 4.2. The use of eight nebulizers led to complete coverage of the 9” substrate (410 cm^2) with magnetite film within 30 mins (Figure 3.4). The film coverage could be visualized as zones or rings (Figure 4.2) of deposit obtained upon reaction of precursor solutions from pairs of nebulizers X_nO_n.

Table 4.2 Deposition conditions for experiments in section 4.1

Platen rotation rate (P_r)	**Reactant solution and concentration**	**Oxidant solution and concentration**	**Liquid feed rate per nebulizer**	**Substrate Temperature**
90 rpm	$FeCl_2$- 16.7 mM	$NaNO_2$-4.35 mM $NaHCO_3$-100 mM	8 ml/min	90°C

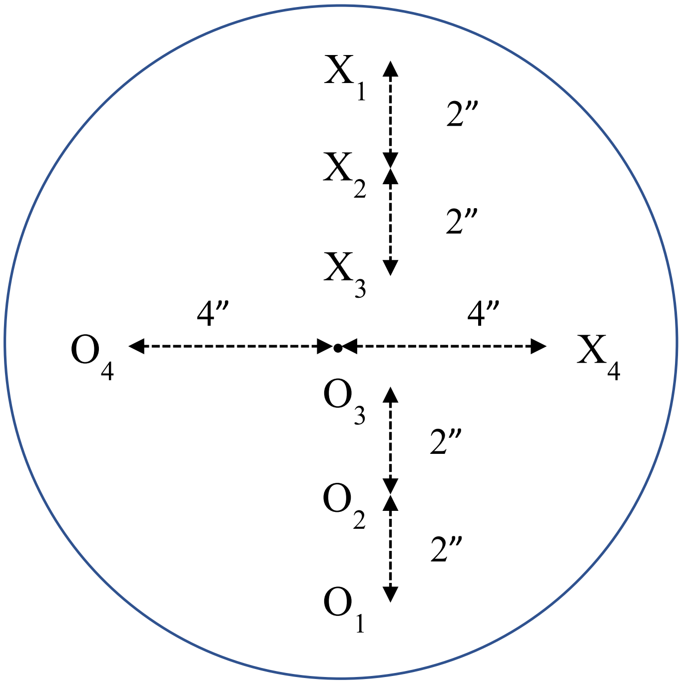

Figure 4.1 Schematic of nebulizer configuration N-8- X_n denotes reactant solution spray and O_n denotes oxidant solutions spray

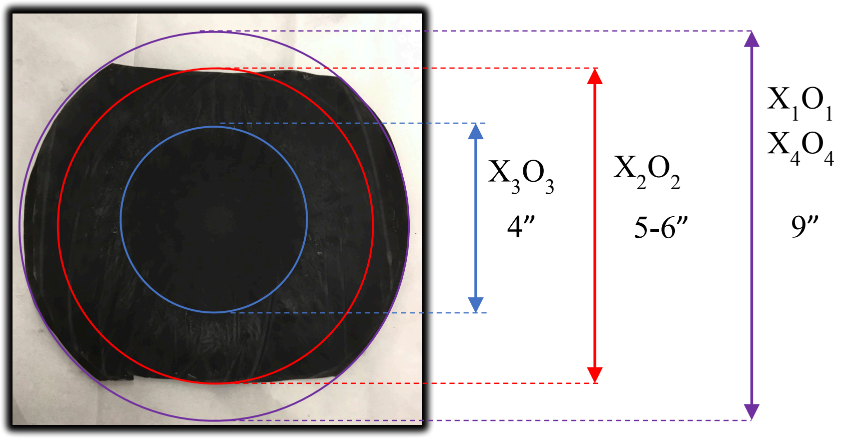

Figure 4.2 Approximate areas of film coverage (from corresponding pairs of nebulizers (X_nO_n)) represented as rings superimposed on a film deposited with 8 nebulizers at 90rpm

The microstructure of these films was discussed previously in section 3.2. While the use of eight nebulizers helped achieve complete and uniform coverage of magnetite macroscopically over the 9” substrate, it proved difficult to control the morphological homogeneity at the microscopic scale. The two predominant morphologies that were observed were the nanoflakes and spherical mosaic grains (Chapter 3). Their distribution was not uniform in all regions, which only amplified with increasing deposition time. When increased to 90 mins, the nanoflakes coarsened to form 150-200 nm thick nanoplates that exhibited lenticular cross-section (Figure 4.3a).

Increasing deposition time also led to the appearance of 250-500 nm faceted polycrystals (Figure 4.3b). These appear to have formed from spherical mosaic grains that coarsened into such structures. An interesting feature was their nanoscale roughness and apparent porosity, suggesting coarsening by nanoparticle aggregation[50]. The lack of homogeneity in microstructure was confirmed by the presence of both anisotropic nanoplates and faceted polycrystals in samples taken from the same region of the film (Figure 4.3 c and d). This non-homogeneity in microstructure was attributed to two major factors:

a) Large volumes of reacting solutions and simultaneous multiple processes: The use of eight nebulizers leads to a constant and uniform supply of reactant and oxidant solutions across the entire substrate throughout the deposition time. This leads to the simultaneous and uncontrolled occurrence of multiple processes (namely crystal nucleation, growth and coarsening) at any given time during deposition.

b) Radial variation in the centrifugal force: Since the platen was 9” in diameter, the centrifugal force experienced by the liquid droplets is not uniform across the platen. The liquid closer to the center experiences smaller force as compared to the liquid further away towards the platen edges. As a result, the residence time of the liquid droplets at the center is longer than at the edges. This in turn leads to their coalescence and the formation of pools with considerable liquid film thickness. Such pooling does not occur along the edges and hence, the liquids comprise largely of individual droplets (Figure 4.4). In other words, the deposition at the center is through a continuous liquid layer, while the deposition at the outer edges is via a micro-droplet regime mechanism [31]. The latter refers to the regime where fluid flow on the substrate can be described by discrete droplets that varied in size between 10-50 microns.

Deposition through a continuous liquid layer is uneven as it relies on the diffusion and mixing of solutions within the layer (Figure 4.5). This can be compared to crystal growth in a stagnant homogeneous solution where, the crystallization occurs in the bulk of the solution. Such an environment is undesired for uniform film deposition. The formation of a continuous liquid layer also gives rise to thermal gradients within it. The temperature at the top of the layer is closer to that of the incoming spray and hence, cooler than the bottom, which is in contact with the heated substrate. This is also undesired as such thermal gradients lead to localized chemical fluctuations (aqueous speciation of metal cations is temperature dependent).

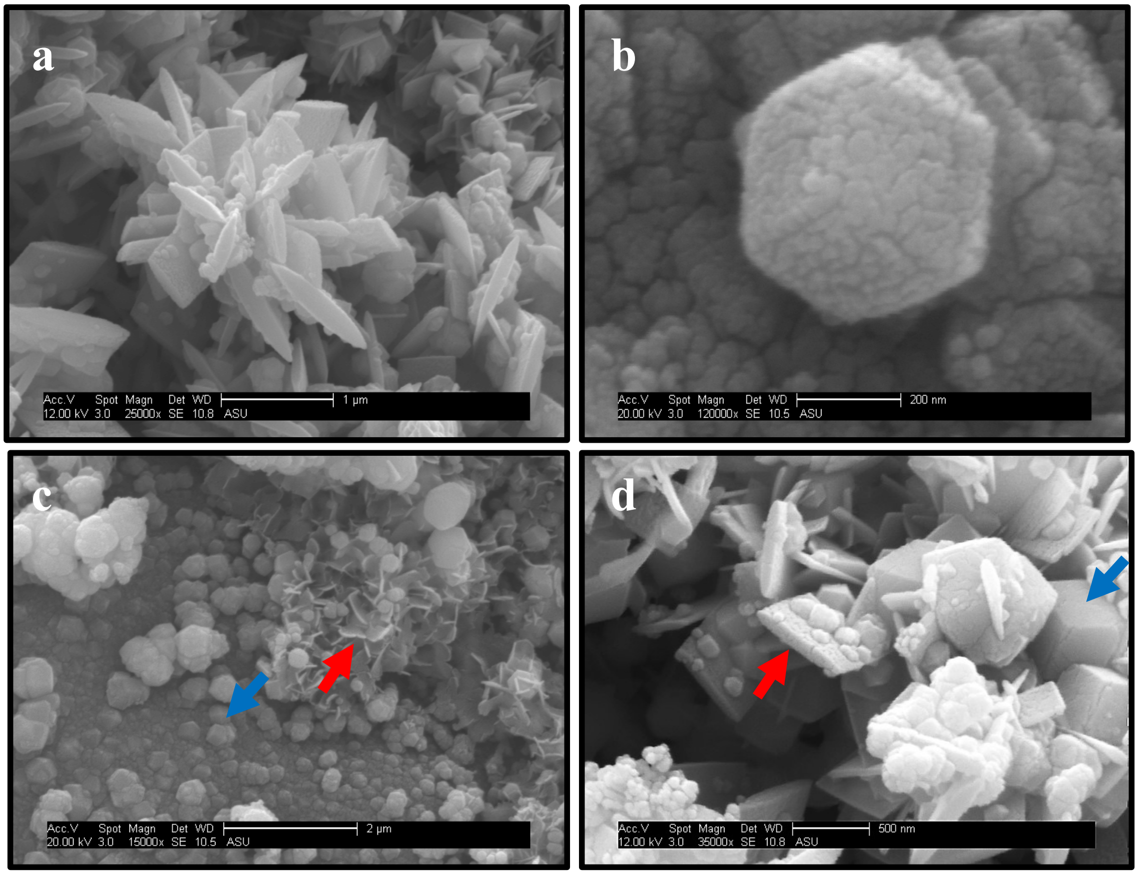

Figure 4.3 SEM images of film deposited for 90 mins (a) Nanoplates showing lenticular cross-section (b) faceted cube showing nanoscale roughness (c and d) occurrence of faceted polycrystals (blue arrows) and nanoplates (red arrows) within the same region of the film

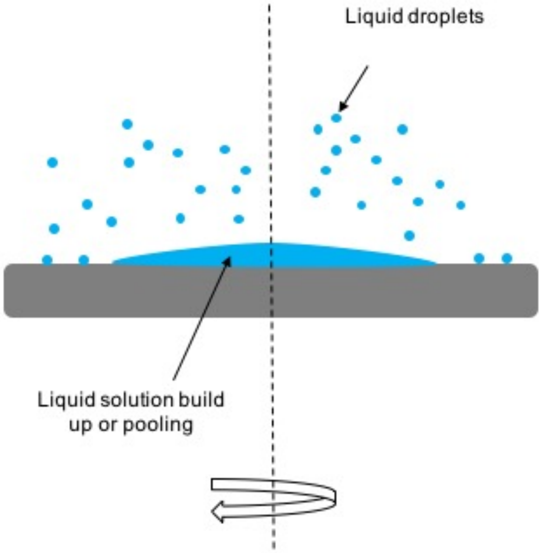

Figure 4.4 Schematic showing differences in liquid film thickness across the substrate

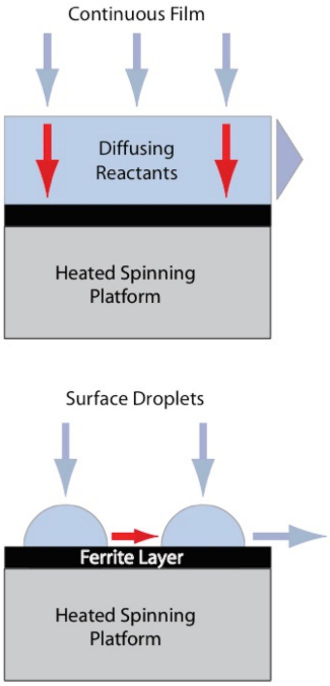

Figure 4.5 Schematic depicting liquid in continuous layer regime and micro-droplet regime[51]

Although these two problems arise primarily due to the use of eight nebulizers, the placement of the nebulizers (N-8) additionally contributes to them. In the N-8 configuration, the inner 4 nebulizers X_2, X_3 and O_2, O_3 (Figure 4.1) are placed closer than the nebulizers on the outside. This leads to larger volumes of solution at the center and consequently, contributes to pooling.

In order to decrease the volume of solutions sprayed onto the substrate, the number of nebulizers was reduced to two; one for the reactant and the other for the oxidant solutions. The flow rate per nebulizer was still maintained at 8 ml/min as was used for each nebulizer in the N-8 configuration. A 30-min deposition run using eight nebulizers consumed a total of 1liter each of the reactant and the oxidant solution. To consume the same total volume of solutions with two nebulizers, the deposition time was increased to 2 hours. When the two nebulizers were placed in positions X_3 and O_3 in Figure 4.1, the deposition area coverage decreased to a 4" diameter circle (81 cm^2) on the substrate. When placed in positions X_2 and O_2, the deposition area was an annular ring of width of 1-2" (50-100 cm^2). Films deposited with either of these configurations did not improve the microstructural homogeneity and were largely comparable to those deposited with the N-8 configuration. This was because the nebulizers were still close enough to one another to cause pooling, thus forming a continuous liquid layer.

When the nebulizers were placed at positions X_1 and O_1, the deposit formed an annular ring of width 0.5-1" (45-85 cm^2) near the outer edge of the substrate. Films deposited with this configuration showed considerably improved uniformity in microstructure. Figure 4.6 shows SEM images of the film. The microstructure consisted of micron sized (5-10 μm) clusters which, in turn, consisted of several hundreds of nanoplates

(80-100 nm thick and 450-500 nm wide) that were randomly intertwined. Faceted polycrystals were not observed in these films. The improvement in the homogeneity of the microstructure is attributed to lower residence times of the liquid droplets near the edges of the platen. Thus, liquid pooling was avoided.

Two kinds of porosity can be defined in porous films with hierarchical microstructures. Inter-cluster porosity comprises large networked pores that exist between the individual clusters. Intra-cluster porosity comprises much smaller pores that exist between the sub-units (nanoplates in this case). While the former can be reasonably estimated by application of image analysis techniques on SEM images, the latter is extremely difficult to quantify. Using *ImageJ* for SEM image analysis [52], the inter-cluster porosity for films deposited at 90 rpm was estimated to be 15.3%. This represents the area fraction of the substrate not covered by the clusters.

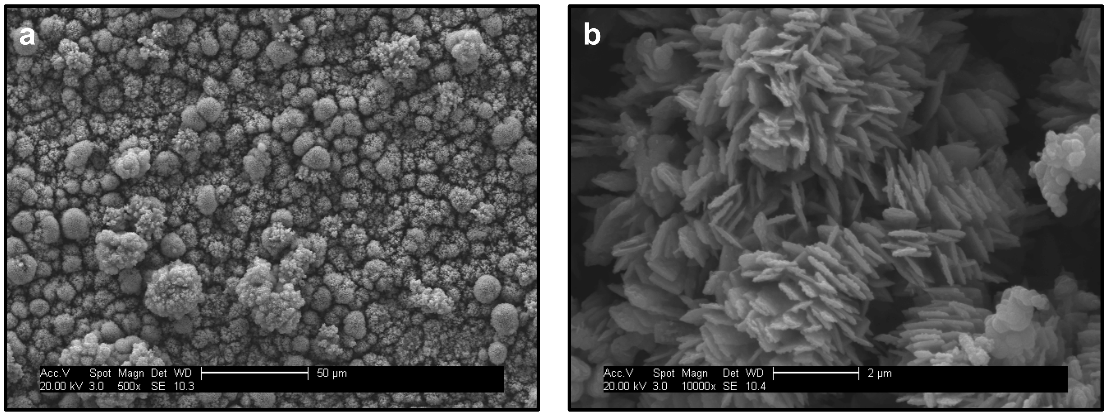

Figure 4.6 SEM images of magnetite film deposited using two nebulizers at X_1 and O_1 (a) low magnification image showing micron-sized clusters (b) high magnification image showing nanoplate sub-units that are contained in the clusters

The experiments described in the following sections were conducted using two-nebulizers placed at positions X_1 and O_1.

4.1.2 Platen rotation speed (P_r):

Another way to decrease the residence time of liquid droplets on the substrate was to increase the speed of rotation of the platen (P_r). When P_r was increased from 90 rpm to 150 rpm, the microstructure consisted of denser clusters that had a broad size range between 5-20 μm (Figure 4.7 a and b). Each cluster was made of several hundreds of intertwined blade-like subunits (Figure 4.7c). Most of these tapered towards the top with a few of them having nearly faceted tips. In the widest regions, the blades were 200-400 nm wide, while at their tips the widths were between 100-150 nm. Their tips were largely encrusted with 50-100 nm sized nanoparticles. (Inferences about these secondary nanoparticles will be described in the subsequent chapters.). The inter-cluster porosity of these films was 9.1%. This decrease was attributed to the congestion of the blade-like subunits and the improved homocentricity of their assembly as a cluster. This is clearly seen in the side-view SEM images taken at a sample tilt of 54° (Figure 4.8 a and b). Low magnification images (Figure 4.8 c) show the homocentric assembly of blade-like subunits giving an apparent impression of growth from a single origin. A similar observation was made by Biswas et al. in TiO_2 films deposited using aerosol assisted MOCVD [53].

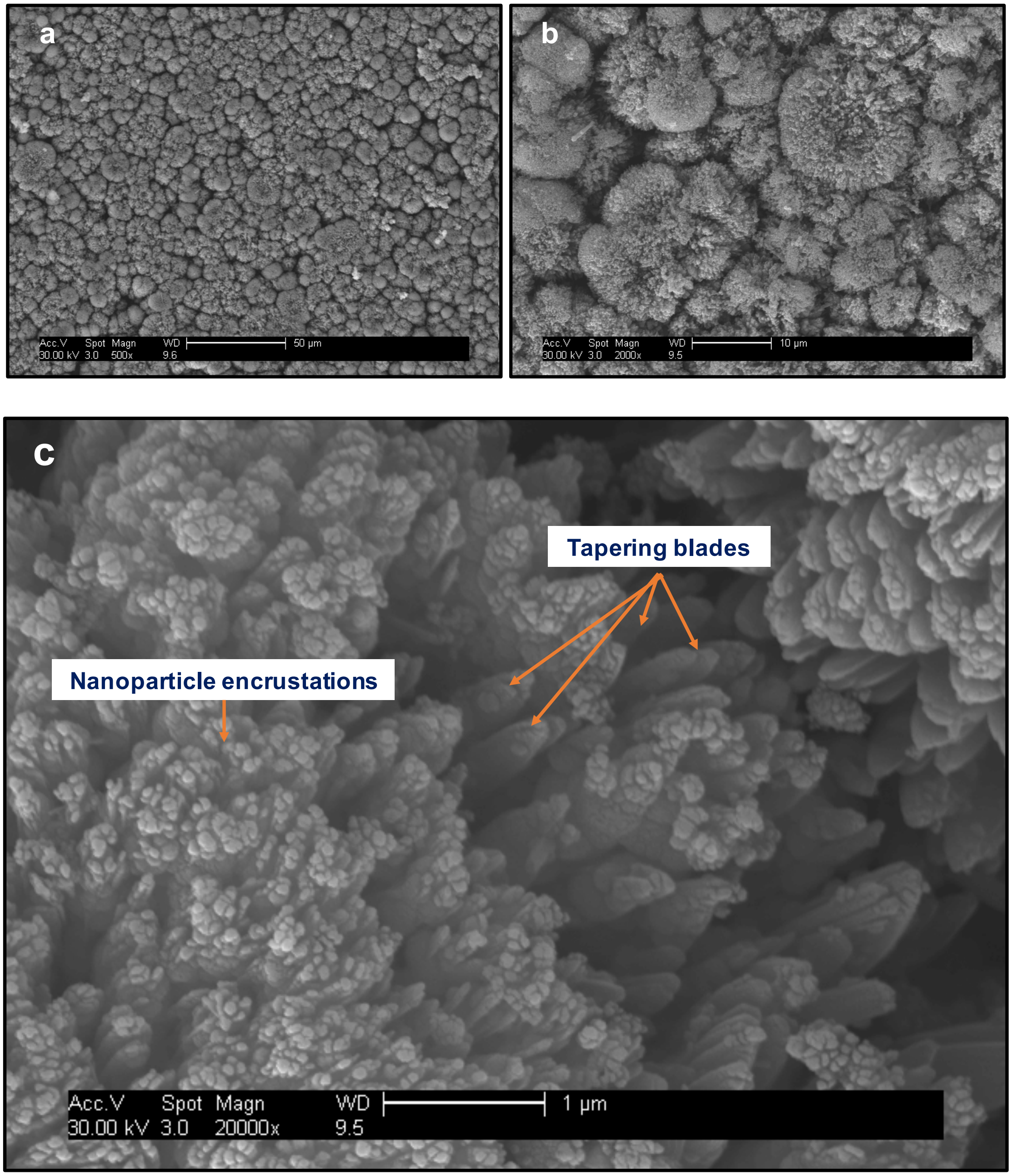

Figure 4.7 SEM images of films deposited at P_r=150 rpm (a and b) low magnification images showing micron-sized clusters (c) high magnification image showing blade-like subunits that are contained in the clusters

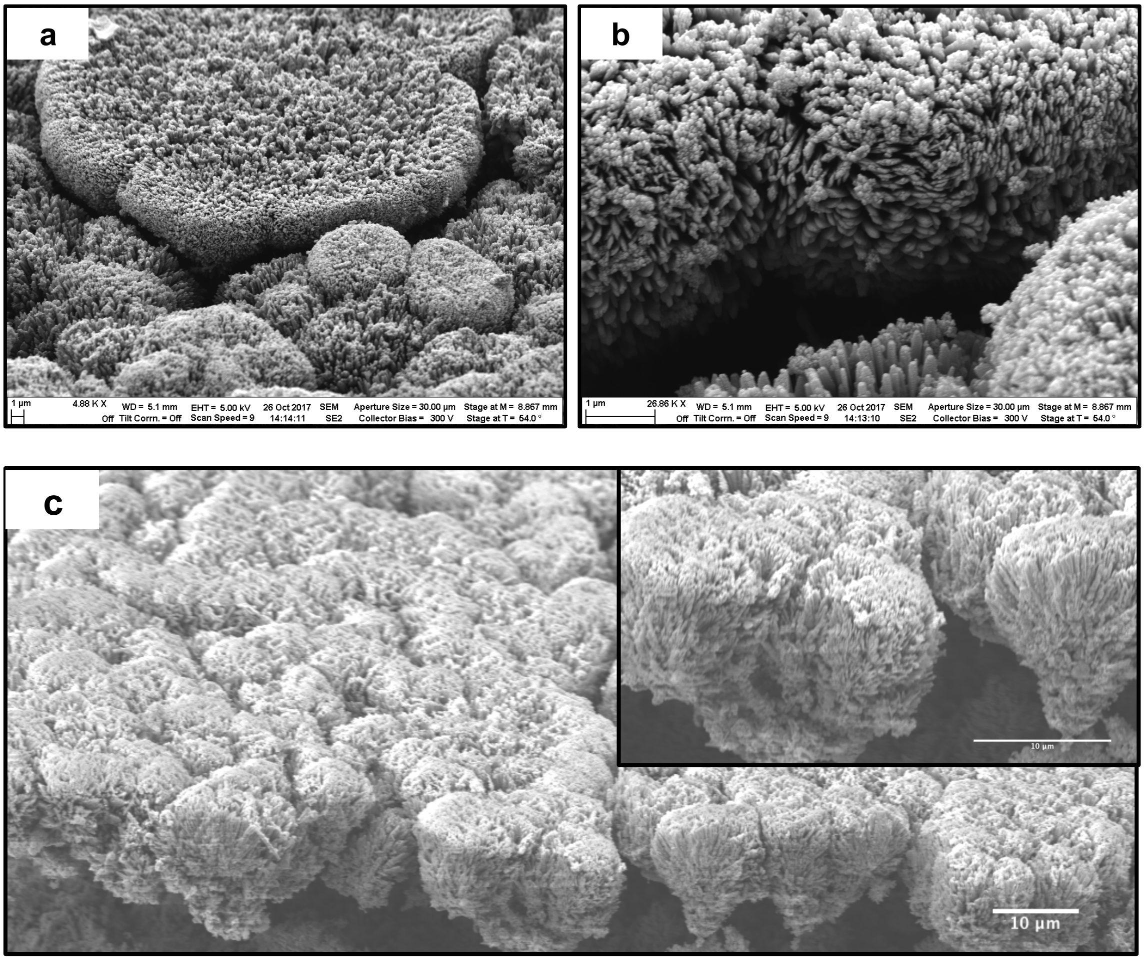

Figure 4.8 SEM images of films deposited at P_r =150 rpm (taken with the sample tilted at 54°) (a) low magnification image of clusters (b) high magnification image showing blade-like subunits that are contained in the clusters (c) low magnification image showing homocentric assembly of blade-like sub-units.

When P_r was increased to 200 rpm, the microstructure of the film obtained was rather unique and exhibited several orders of morphological hierarchy. At the largest length scale, clusters of several columnar structures were observed (Figure 4.9). These columns were 3-10 μm long and tapered towards their apex. They were made up of stacks of several disc shaped mosaic structures. These discs were 200-400 nm in diameter and comprised smaller 2-20 nm sized nanoparticles (Figure 4.10b). The width of the columns varied depending on if columns were made up of only one isolated stack of discs or others that had two or three stacks attached to one another lengthwise along their sides (Figure 4.10a). SEM images obtained by tilting the sample to 45° showed the apparent growth of multiple columns from a single origin forming a cluster (Figure 4.11 a). These clusters consisted of much fewer columns (a few tens) as compared to the clusters of nanoplates/blades (hundreds) described previously. Although the angular spread of majority of the clusters is between 80°-120°, a large fraction of the individual columns is at an angle of 90°-110° with respect to the substrate. This indicates a preferred growth direction close to the normal to the substrate (Figure 4.11 b).

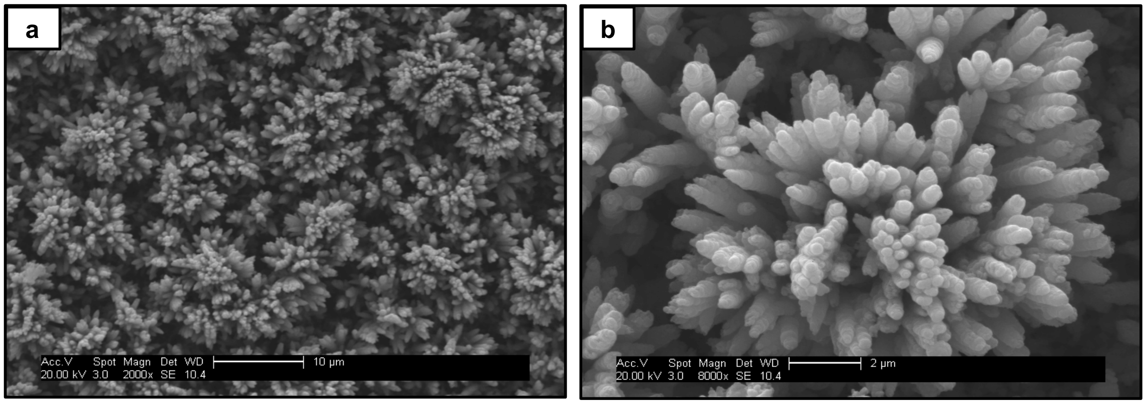

Figure 4.9 Low magnification SEM images of films deposited at P_r =200 rpm

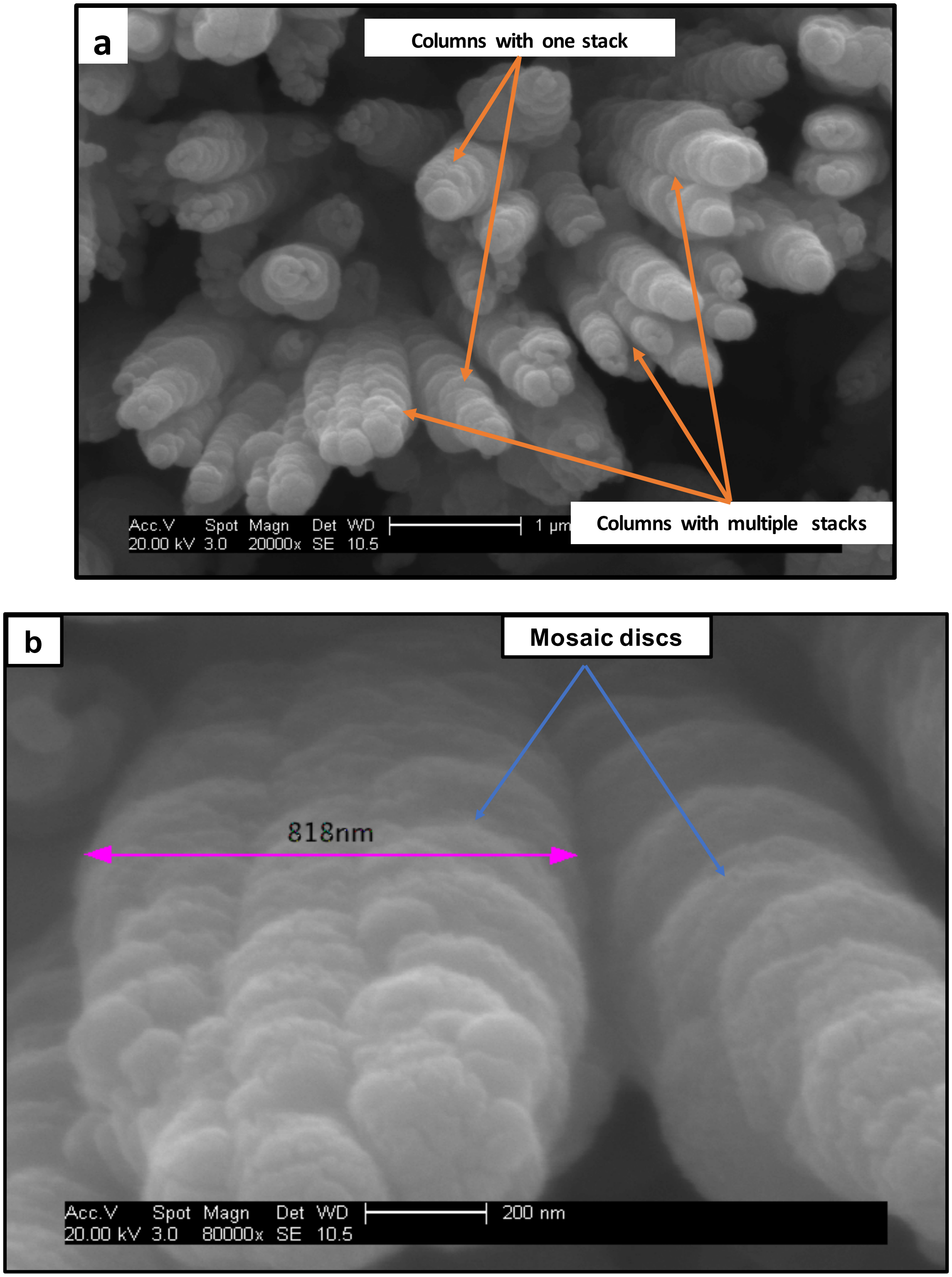

Figure 4.10 (a) SEM image showing columns made up of stacked mosaic discs (b) High magnification image showing mosaic discs

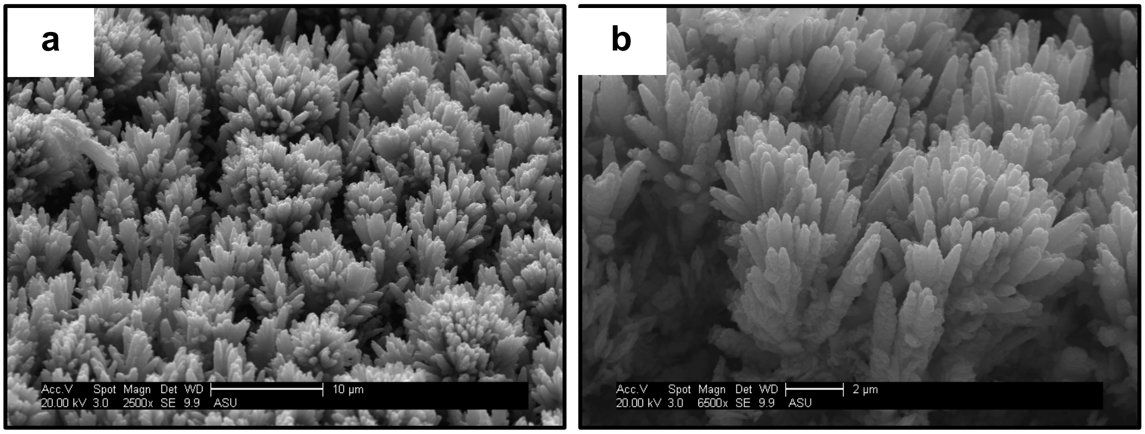

Figure 4.11 SEM images of films deposited at P_r=200 rpm (taken with the sample tilted at 45°) (a) low magnification image showing clusters of columns (b) high magnification image of the same.

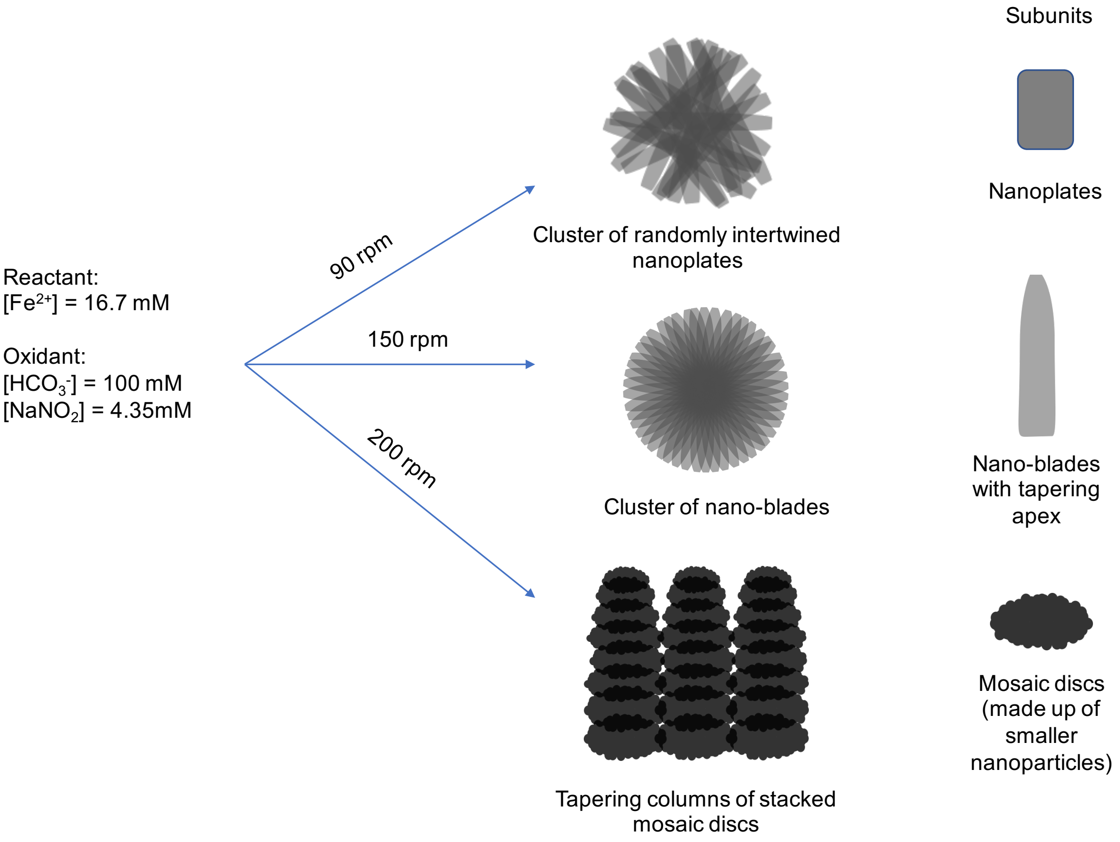

Figure 4.12 Schematic of the different hierarchical morphologies of porous magnetite films

4.2 Effect of process parameters affecting chemical behavior of solutions:

4.2.1 Effect of concentration of HCO_3^-:

In order to understand the influence of $NaHCO_3$ on the microstructural formation of the films, separate experiments with 50 mM, 25 mM, 10 mM, 5 mM, 2 mM and 0 mM concentration of $NaHCO_3$ in the oxidant solution were carried out. The concentration of $NaNO_2$ in the oxidant solutions was kept constant at 4.35 mM for all these experiments and the concentration of $FeCl_2$ in the reactant solution was fixed at 16.7 mM. The rotation speed of the platen was 200 rpm.

When the concentration of $NaHCO_3$ in the oxidant was 50 mM (considered relatively high), the microstructure of the film showed polydispersed and poorly organized spherical mosaic grains (Figure 4.13a-b). This film appeared jet-black in color and had a rough texture. When 25 mM $NaHCO_3$ was used, the film was grey in color and smoother in texture. SEM analysis revealed a dense microstructure (area fraction of uncovered substrate <1%) consisting of mosaic 2-5 μm microspheres (Figure 4.13c) that were in turn made of smaller 50-70 nm nanoparticles (Figure 4.13d). Decreasing the concentration further to 10 mM led to deposition of a lustrous grey colored film that had a dense microstructure (area fraction of uncovered substrate <1%) consisting of faceted mosaic crystals (Figure 4.13e-f). These polycrystals had edges 300-400 nm in length and were made up of smaller 15-50 nm nanoparticles. With $NaHCO_3$ concentrations of 5 mM, 2 mM and 0 mM in the oxidant solution, magnetite was no longer deposited. Instead, a faint red colored film was obtained. The exact phase of this film could not be identified as it was extremely thin to be detected by X-ray diffraction. However, the red color suggested that it was possibly hematite.

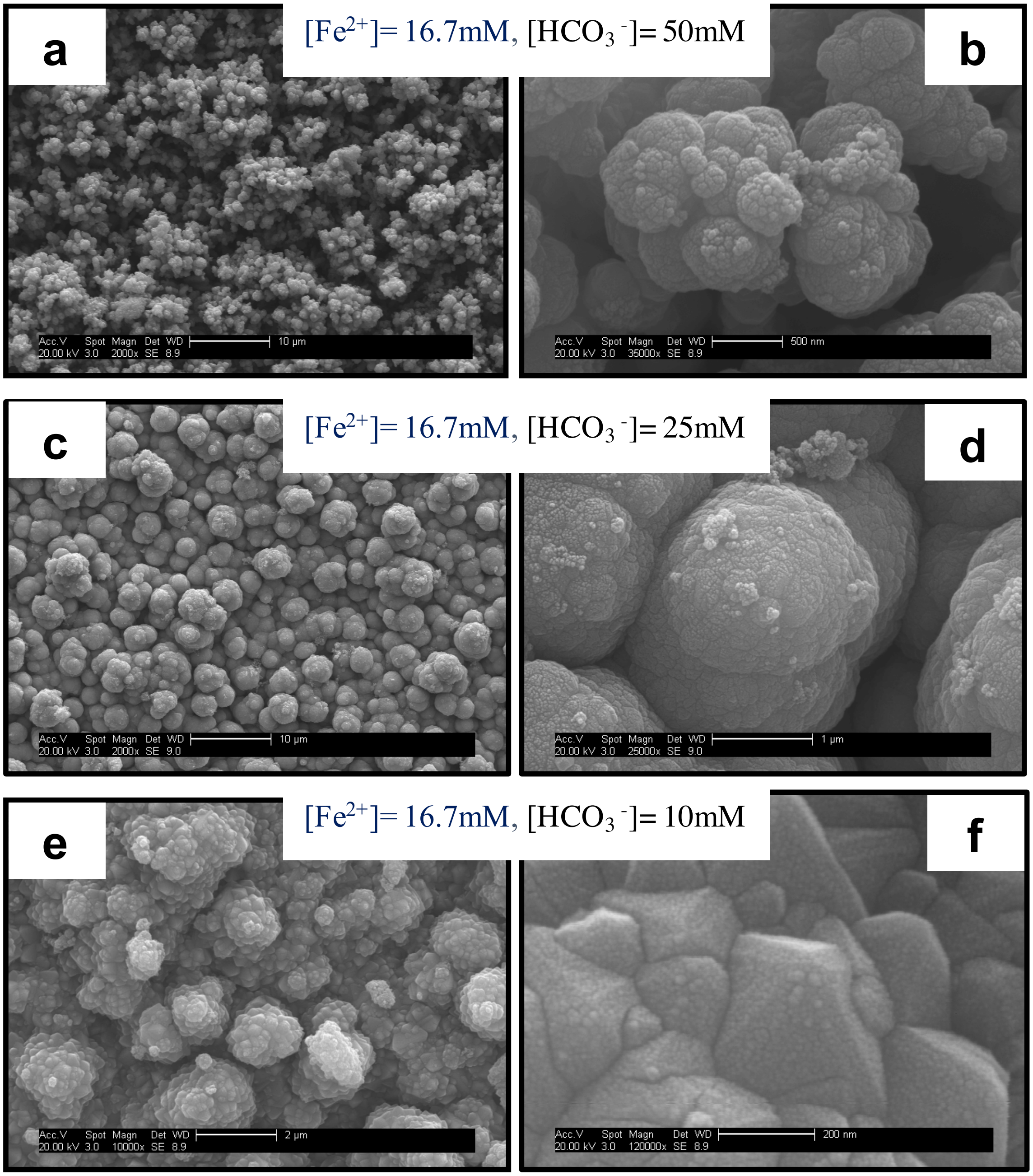

Figure 4.13 SEM images showing microstructures of films deposited with various concentrations of $NaHCO_3$

4.2.2 Effect of Fe^{2+} concentration:

The effect of $[Fe^{2+}]$ was similarly studied by carrying out experiments with 2 mM, 5 mM and 10 mM $FeCl_2$ solutions as reactant. The oxidant solution used for all these experiments comprised 4.35 mM $NaNO_2$ and 100 mM $NaHCO_3$. The rotation speed of the platen was 200 rpm.

The effect of $[Fe^{2+}]$ on the morphologies obtained was similar to that of $[HCO_3^-]$, that is, the density of the films increased with decreasing concentration. With decreasing $[Fe^{2+}]$, film color changed from black to grey (and lustrous) and film texture changed from rough (and flaky) to smooth. The microstructure of films deposited with 10 mM $[Fe^{2+}]$ consisted of 2-5 μm sized mosaic microspheres, which in turn were made up of 50-70 nm sized nanoparticles (Figure 4.14a-b). The cross-section of these films suggested a particulate self-assembly into such mosaic morphologies (Figure 4.14a inset). Films deposited with 5 mM and 2 mM $[Fe^{2+}]$ showed dense microstructures with 300-400 nm faceted mosaic crystals (Figure 4.14c-d). The cross-section of these films showed a columnar structure (Figure 4.14c inset).

$[Fe^{2+}]$= 10mM, $[HCO_3^{\ -}]$= 100mM

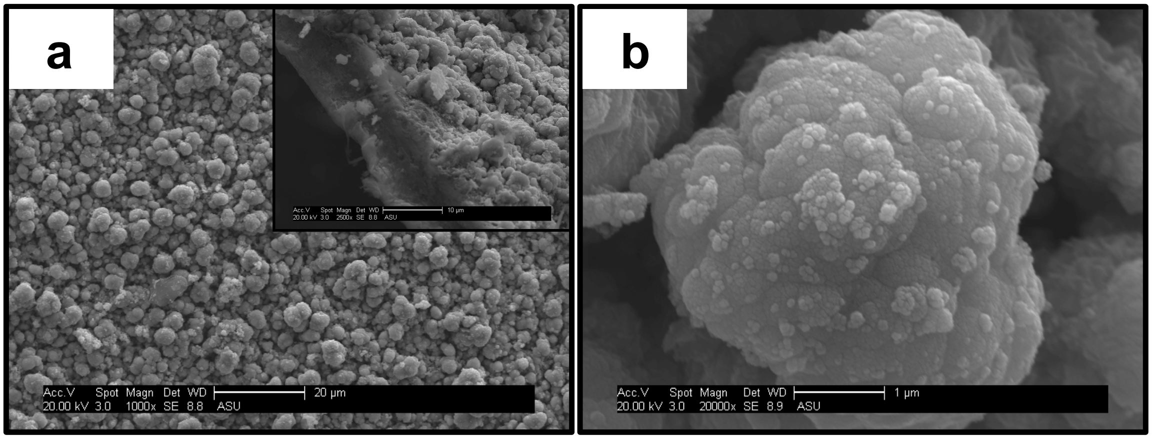

$[Fe^{2+}]$= 2mM, $[HCO_3^{\ -}]$= 100mM

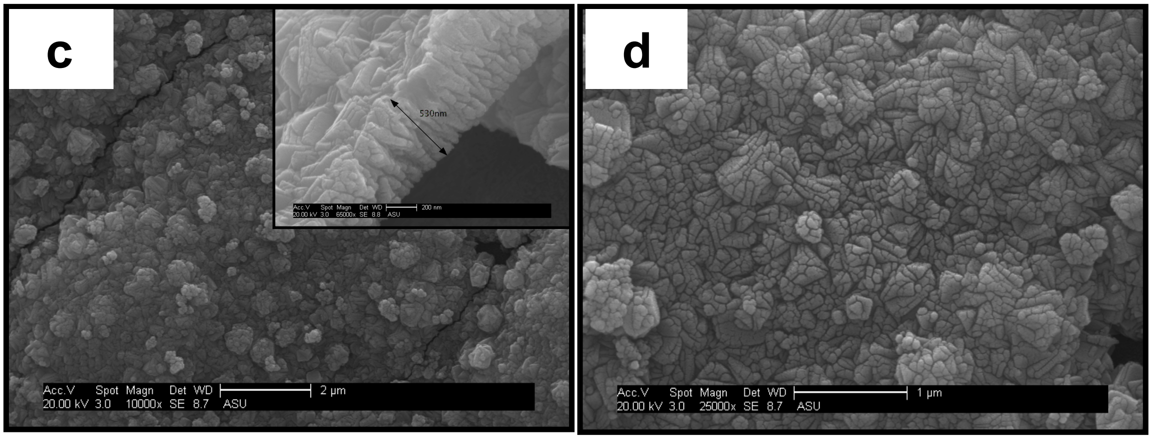

Figure 4.14 SEM images showing microstructures of films deposited with various concentrations of $FeCl_2$

A subsequent set of experiments were carried out in which the concentrations of both Fe^{2+} (in the reactant) and HCO_3^- (in the oxidant) were varied systematically. The rotation rate of the platen was fixed at 200 rpm. Based on these experiments, a field map was constructed to classify microstructural features of magnetite films as a function of $[Fe^{2+}]$ and $[HCO_3^-]$. This has been illustrated in Figure 4.15. It was observed that with extremely low concentrations of Fe^{2+} (0-2 mM) and HCO_3^- (0-10 mM), no magnetite film was deposited. Films with good adhesion to the substrate were deposited for $[Fe^{2+}]$ between 2 mM to 17 mM and $[HCO_3^-]$ between 10 mM and 100 mM. However, the adhesion relatively decreased as concentrations of both species were increased simultaneously. These films were grey and lustrous in appearance and had dense microstructures.

It was also observed that the microstructure of the films deposited with $[Fe^{2+}]$ between 2 mM to 10 mM and $[HCO_3^-]$ between 10-100 mM consisted of faceted mosaic crystals. For $[Fe^{2+}]$ between 10-17 mM and $[HCO_3^-]$ between 25-100 mM, the microstructure of magnetite films consisted of mosaic microspheres (section 4.2.1). Beyond 17 mM $[Fe^{2+}]$ and 100 mM $[HCO_3^-]$, the films deposited were very flaky and poorly adhered to the substrate. They were jet-black in appearance and rough textured. These films had porous microstructures (section 4.1.2).

These differences in morphological features and film density was a consequence of the deposition rates of the film, which in turn was dependent on the concentrations of the solutions used. Linear deposition rates were determined by measuring film thickness from SEM images. Figure 4.16 shows the dependence of linear film deposition rates on $[HCO_3^-]$ and $[Fe^{2+}]$. Keeping $[Fe^{2+}]$ constant, increase in $[HCO_3^-]$ led to increase in linear deposition rates (Figure 4.16a). This increase became more pronounced at higher $[Fe^{2+}]$

(porous films). A similar relationship was seen when [HCO_3^-] was kept constant and only [Fe^{2+}] was changed, i.e. linear deposition rate increased with increasing [Fe^{2+}] (Figure 4.16b). Figure 4.16c shows linear deposition rates plotted as a function of the product of the concentrations of [Fe^{2+}] and [HCO_3^-]. A direct dependence of linear deposition rates on the concentrations of both species is clearly seen, that is,

$$Linear\ deposition\ rate\ \propto [Fe^{2+}].[HCO_3{}^-]$$

Mass deposition rates were determined calculating the average mass deposited per unit area per minute (six different samples of varying dimensions were weighed, for each deposition condition). Figure 4.17 shows mass deposition rates plotted as a function of [HCO_3^-] for films deposited at a constant [Fe^{2+}] of 16.7 mM. The mass deposited showed a logarithmic relationship with [HCO_3^-] for concentrations up to 50 mM. Beyond 50 mM, the films began to flake off the substrate and hence, reliable data on mass deposited could not be collected. However, this showed that mass deposition rates also increased with increasing concentrations of solutions.

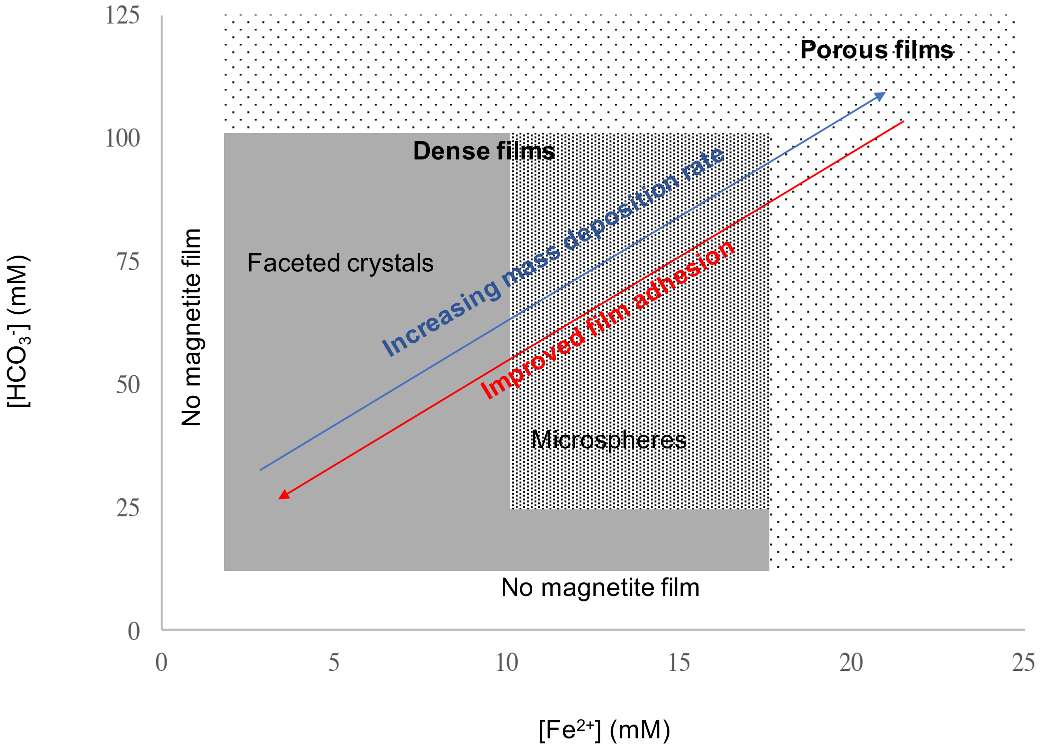

Figure 4.15 Field map of microstructural features of magnetite films as a function of $[Fe^{2+}]$ and $[HCO_3^-]$

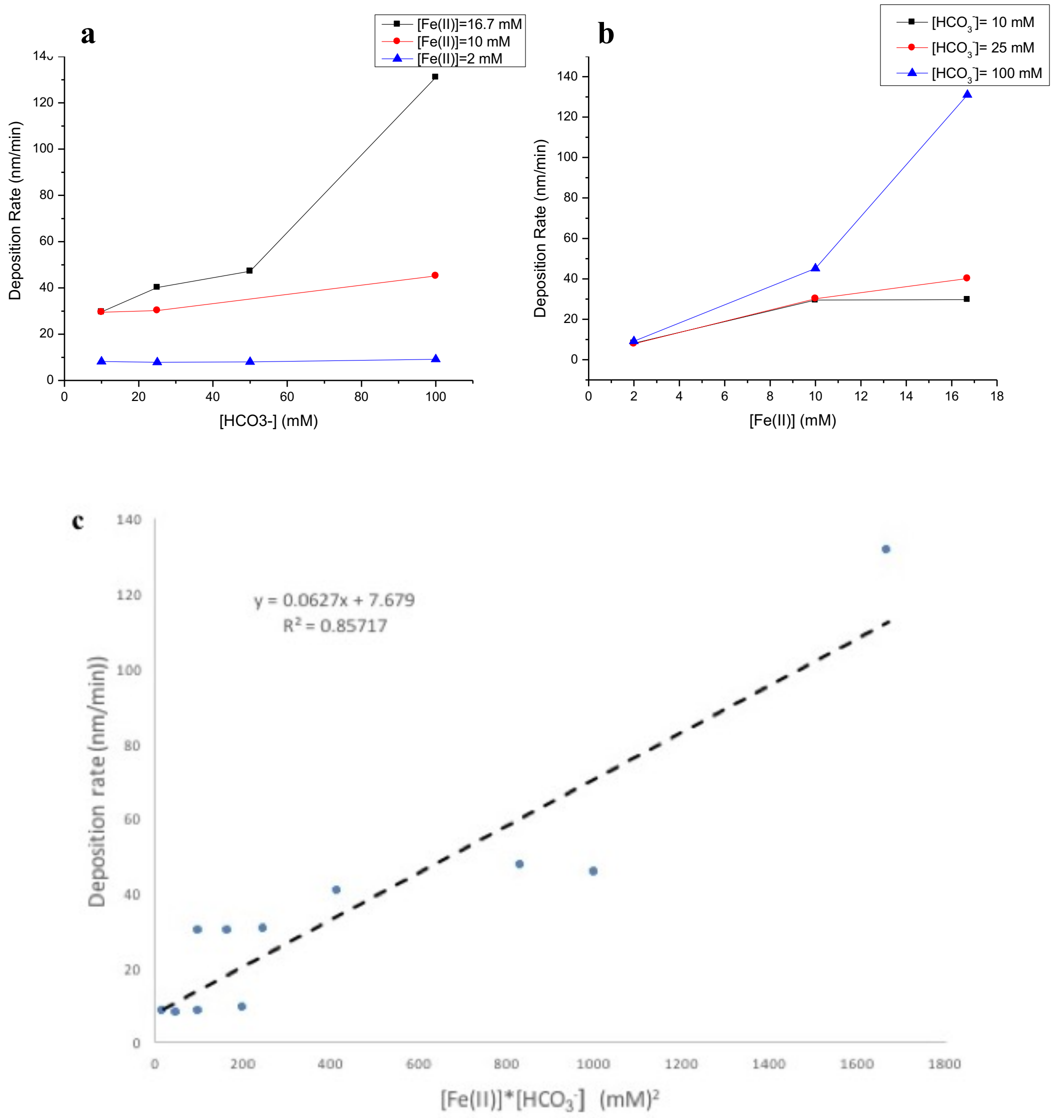

Figure 4.16 (a) Linear Deposition rate vs [HCO_3^-] (b) Linear Deposition rate vs [Fe^{2+}] (c) Linear Deposition rate vs [Fe^{2+}].[HCO_3^-]

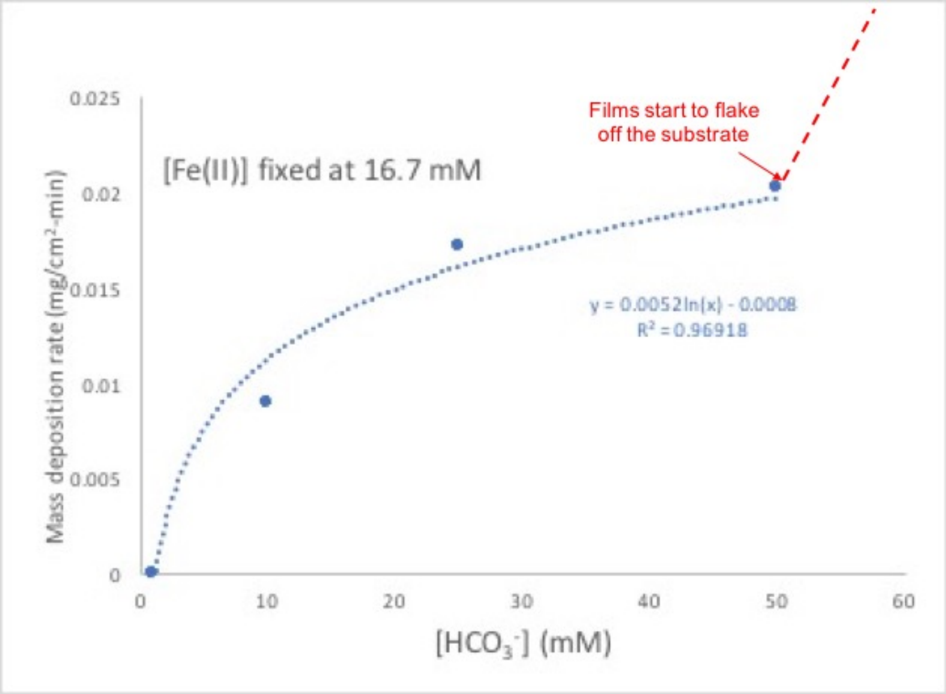

Figure 4.17 Mass Deposition rate vs [HCO_3^-] at fixed [Fe^{2+}] =16.7 mM

4.3 Conclusions:

Spin spray deposition was used to deposit magnetite films on large areas of flexible PEEK substrate. The effect of various SSD process parameters on the deposition of magnetite films was studied. Process parameters like number of nebulizers, nebulizer configuration and platen rotation speed that affected the volume of liquid and liquid residence time on the substrate influenced the homogeneity of film microstructure. Low volume of solutions (liquid feed rate) and shorter liquid residence time (μ-droplet regime) led to most homogeneous microstructures across the entire film area.

Microstructures of magnetite films obtained consisted of hierarchically organized crystal morphologies spanning length scales from tens of nanometers to a few microns. A variety of isotropic and anisotropic self-assembled crystal morphologies were deposited by varying process parameters such as platen rotation rate and precursor solution concentrations i.e. [Fe^{2+}] and [HCO_3^-]. The latter additionally influenced film density and adhesion of films to the substrate. A field map was constructed to classify the microstructural features obtained for a range of [Fe^{2+}] and [HCO_3^-]. Simultaneous increase of both these concentrations led to decrease in film density and adhesion. No magnetite film was obtained for extremely low concentrations. These observations were a direct consequence of the magnitude of the film deposition rates. Linear deposition rate was found to be directly proportional to the concentrations of the precursor solutions.

Chapter 5

STRUCTURAL ANALYSIS OF HIERACHICALLY ORDERED MAGNETITE

In Chapter 4, a variety of hierarchically organized morphologies of magnetite were synthesized by varying different process parameters. All the morphologies discussed exhibited at least one form of particle self-assembly into ordered structures. In order to understand the nuances of their ordering and crystalline structure, complimentary characterization techniques such as HRTEM and SAED were employed to study select samples. TEM characterization was carried out using FEI Titan 300/80 aberration corrected TEM and a Philips CM200-FEG TEM.

Morphology and microstructure can serve as indicators for crystal growth mechanisms at play. Evidence of non-classical growth mechanisms can include features such as dimpled surfaces, nanoscale surface roughness, internal porosity in crystals, dislocations etc.[54] Hence, careful TEM analysis and interpretation can play an important role in identifying growth mechanisms.

5.1. TEM studies:

TEM characterization showed that the sub-units of the cluster morphologies (described in section 4.1) fell apart during sonication for TEM sample preparation. This confirmed that the sub-units loosely assembled into clusters and no bonding occurred between them.

A low magnification TEM image (Figure 5.1a) of the edge of a nanoplate showed that the nanoplates were made up of an agglomeration of several smaller 3-5 nm sized nanoparticles (primary nanoparticles). This was not evident from the SEM images. The nanoscale surface roughness of the nanoplates was already an indication of particle mediated (non-classical) crystallization. Another important observation that alluded to this was the variations in contrast. This revealed the presence of internal porosity between the primary nanoparticles within the nanoplates. Lattice fringes in the HRTEM image (Figure 5.1b) of the same nanoplate confirmed the crystalline nature of the primary nanoparticles. A selected area electron diffraction (SAED) pattern (Figure 5.1c) of the nanoplate confirmed that the smaller nanoparticles were magnetite and showed bright spots that indicated preferred orientation. However, the presence of segments of diffraction rings (arcs) indicated that the crystallographic alignment within the nanoplate was not perfect (that is, not being a porous single crystal, but a polycrystal comprising minor disregistry of the relative orientations of the crystallites). Such observations have been a common occurrence in crystals growing via non-classical mechanisms [2, 55, 56].

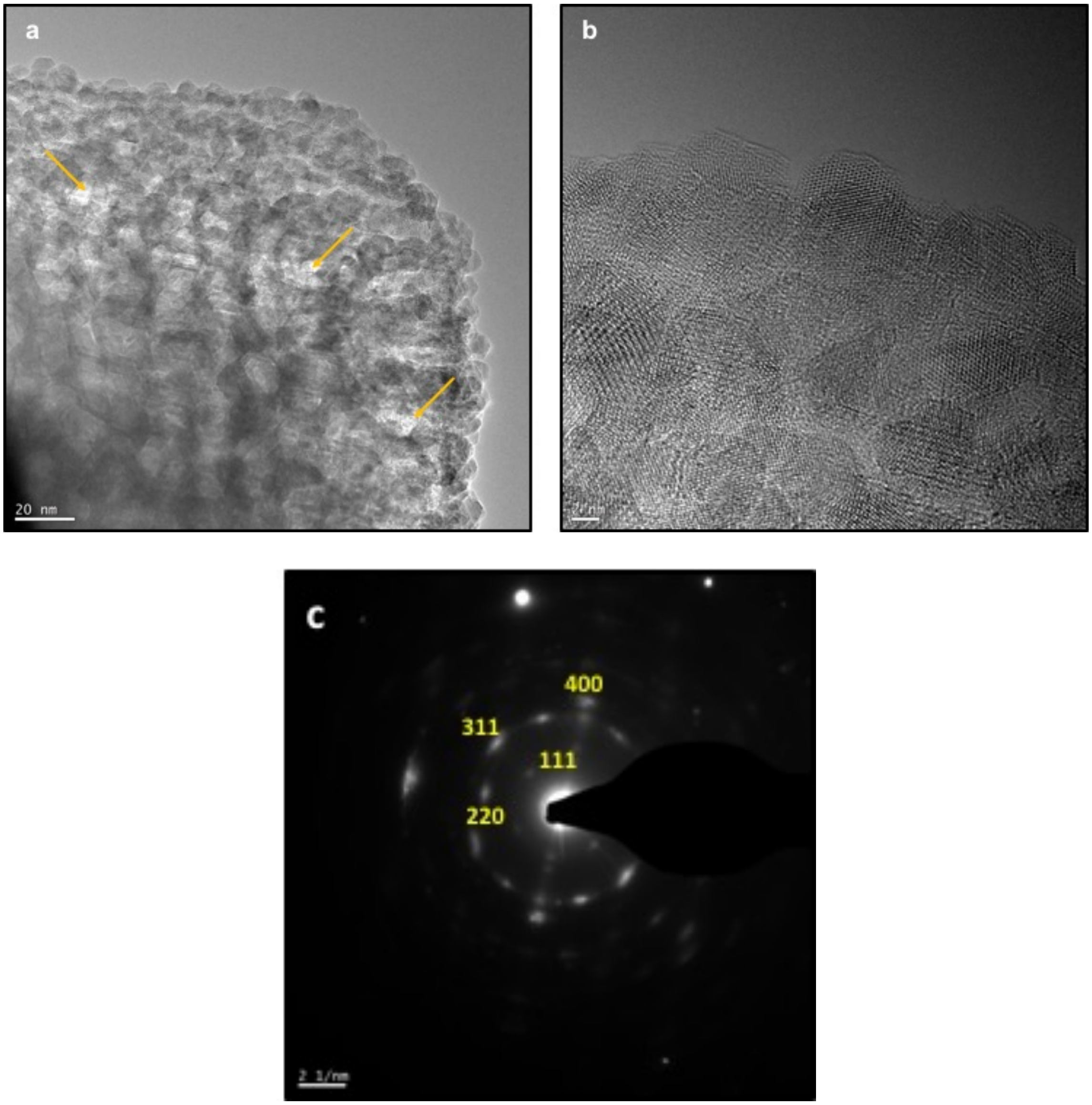

Figure 5.1 TEM images of a nanoplate (a) low magnification image showing aggregation of primary nanoparticles (arrows indicate examples of internal porosity) (b) HRTEM image showing crystalline nature of nanoparticles (c) SAED pattern of nanoplate showing preferred orientation (indexed planes correspond to magnetite).

Figure 5.2a shows a low magnification image of nano-blades. In contrast to the nanoplates, the nanoblades had much more well defined edges. The blades were wider at the bottom and tapered towards the top. HRTEM imaging (Figure 5.2b) of the nano-blade also showed contrast variations. It was unclear if this was due to porosity or thickness variations. In other words, porosity was not as obvious as in the nanoplate case. This was attributed to the fact that the nano-blades behaved more like a single crystal, as confirmed by the presence of spots seen on a Fast Fourier Transform of the HREM image (Figure 5.2b inset).

Mesocrystals or even nearly oriented crystals made up of smaller nanoparticles (as observed in the nanoplates case) often serve as intermediates in the formation of single crystals[1, 57]. They are notoriously difficult to detect as they can be short-lived. This is because, the nanoparticles making the mesocrystal can crystallographically fuse together to form a perfect single crystal[57]. Hence, although nanoblades exhibited single crystalline structure, involvement of an intermediate mesocrystal in its formation cannot be completely ruled out.

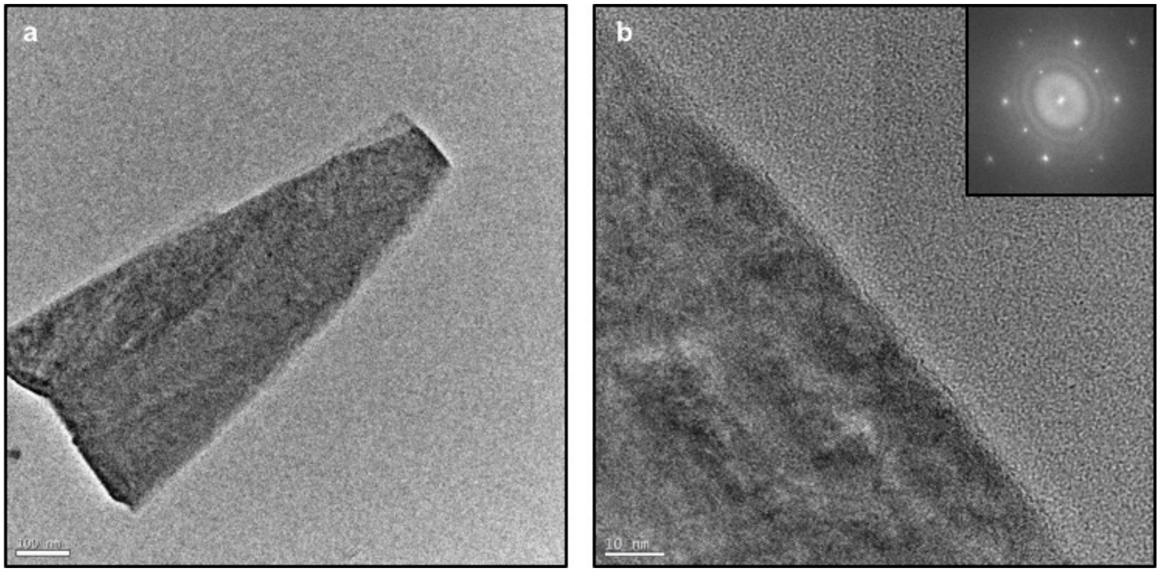

Figure 5.2 TEM images of a nanoblade (a) low magnification image showing two overlapping nanoblades (b) HRTEM and FFT (inset) image showing crystalline nature of nanoblades ([1 1 2] zone axis of magnetite).

Figure 5.3a shows a low magnification image of a stacked column. As seen already from the SEM images, this structure showed several orders of organization. The columns were the largest (micron sized) and thickest features grown using the spin spray deposition technique and hence were not electron transparent. However, HRTEM images of the apex of the column showed that the organization began at the nanoscale (Figure 5.3b). The tip of column showed the presence of several 3-5 nm sized nanoparticles. This region also revealed internal porosity suggesting crystal growth by non-classical mechanisms. FFT of the HREM image (Figure 5.3b inset) confirmed crystallinity and the phase of the nanoparticles to be magnetite. The presence of spots instead of rings in the FFT showed that the nanoparticles organized with a preferred orientation.

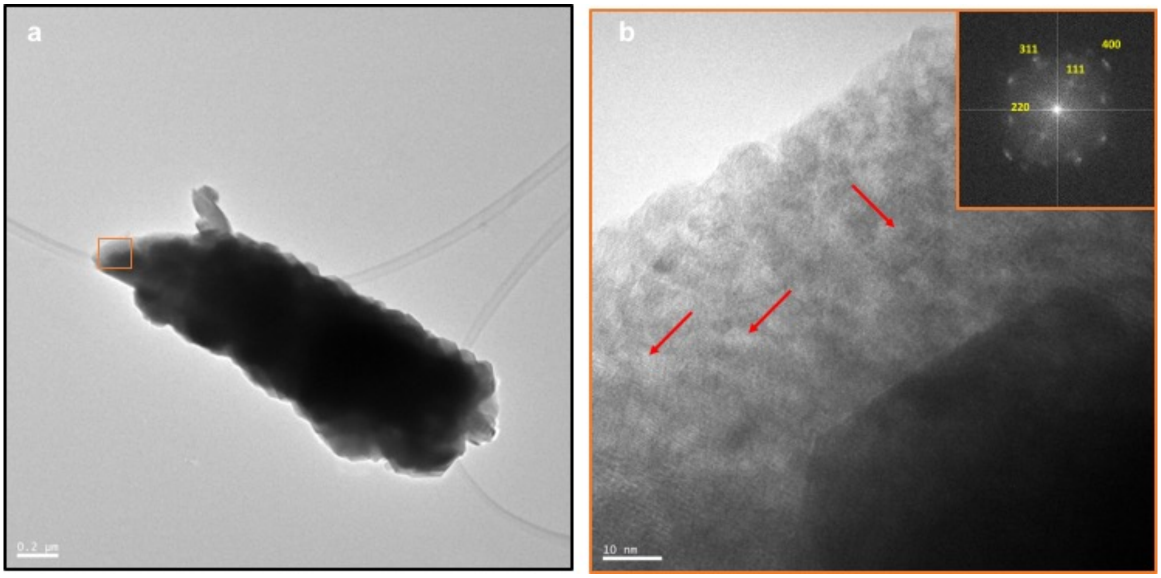

Figure 5.3 TEM images of a nanoplate (a) low magnification image showing stacked columns (scale bar- 0.2 µm) (b) HRTEM and FFT (inset) image showing presence of nanocrystalline sub-units (arrows indicate examples of internal pores, scale bar- 10 nm)

The presence of internal porosity and nanoparticle aggregation into preferentially oriented or completely oriented structures such as nanoplates, or columns suggested the possibility of one of two growth mechanisms - (a) nucleation of primary magnetite nanoparticles followed by nearly oriented or oriented aggregation, or (b) involvement of a metastable crystalline or amorphous precursor phase (oxyhydroxides) followed by its re-crystallization (due to dehydration/solid-state phase transformation) into magnetite nanoparticles and then, nearly oriented/oriented aggregation of magnetite nanoparticles into the final morphologies. Time-resolved experiments can help evaluate the merit of one mechanism over the other and this will be discussed in the next chapter.

5.2 Conclusions:

TEM characterization of the hierarchical morphologies of magnetite showed that the process of self-assembly began at the nanoscale (~3-5 nm). It was found that the nanoplates had very distinct internal porosity and were made up of preferentially oriented magnetite nanoparticles. The nanoblades behaved like a single crystal. The apex of the stacked columnar structures showed preferential orientation of 3-5 nm sized nanocrystals of magnetite. Features such as internal pores, dimpled surfaces (nanoscale surface roughness) and nearly oriented sub-units suggested that crystal growth occurred by particle attachment (non-classical crystal growth). Based on these observations, two possible mechanisms for crystal growth were hypothesized: a) direct nucleation of magnetite nanoparticles from solution, followed by their self-assembly, or, b) nucleation of a precursor phase (amorphous or crystalline) which underwent transformation to magnetite, followed by self-assembly. These mechanisms can be distinguished by carrying out time resolved experiments.

Chapter 6

MECHANISTIC ASPECTS OF MAGNETITE FILM GROWTH USING SPIN SPRAY DEPOSITION

6.1 Time resolved microstructure evolution of porous magnetite films:

Porous magnetite films were obtained when high [Fe^{2+}] and [HCO_3^-] (Figure 4.15) were used in the precursor solutions. A series of time resolved experiments were carried out to understand their microstructural evolution. These depositions were carried out for platen rotation speeds (P_r) of 150 rpm and 200 rpm. The concentrations of precursor solutions used were 16.7 mM $FeCl_2$ (reactant) and 100 mM $NaHCO_3$/4.35 mM $NaNO_2$ (oxidant). Deposition was carried out separately for multiple time intervals, following which the films were analyzed for phase purity using X-ray and electron diffraction, and for microstructure using SEM.

Figure 6.1 shows the phase evolution (depicted by XRD data) of films deposited at P_r= 150 rpm as a function of time. Films obtained after 15 mins of deposition were green-blue in color and changed to an orange-brown upon prolonged exposure to air (typically one hour). X-ray diffraction did not provide conclusive phase identification as the film was very thin at this stage. However, electron diffraction (Figure 6.5b) confirmed the phase to be “green rust I” (GRI) (Samples for electron diffraction analysis were prepared by depositing directly onto a TEM grid). After 30 mins of deposition, the film obtained was black in color and consisted only of magnetite (verified using JCPDS card number 00-019-0629), which remained stable in air. However, the peak intensities in the XRD data were low due to small film thickness. At 60 mins and 120 mins much more intense magnetite peaks were observed confirming the increase of film thickness with deposition time.

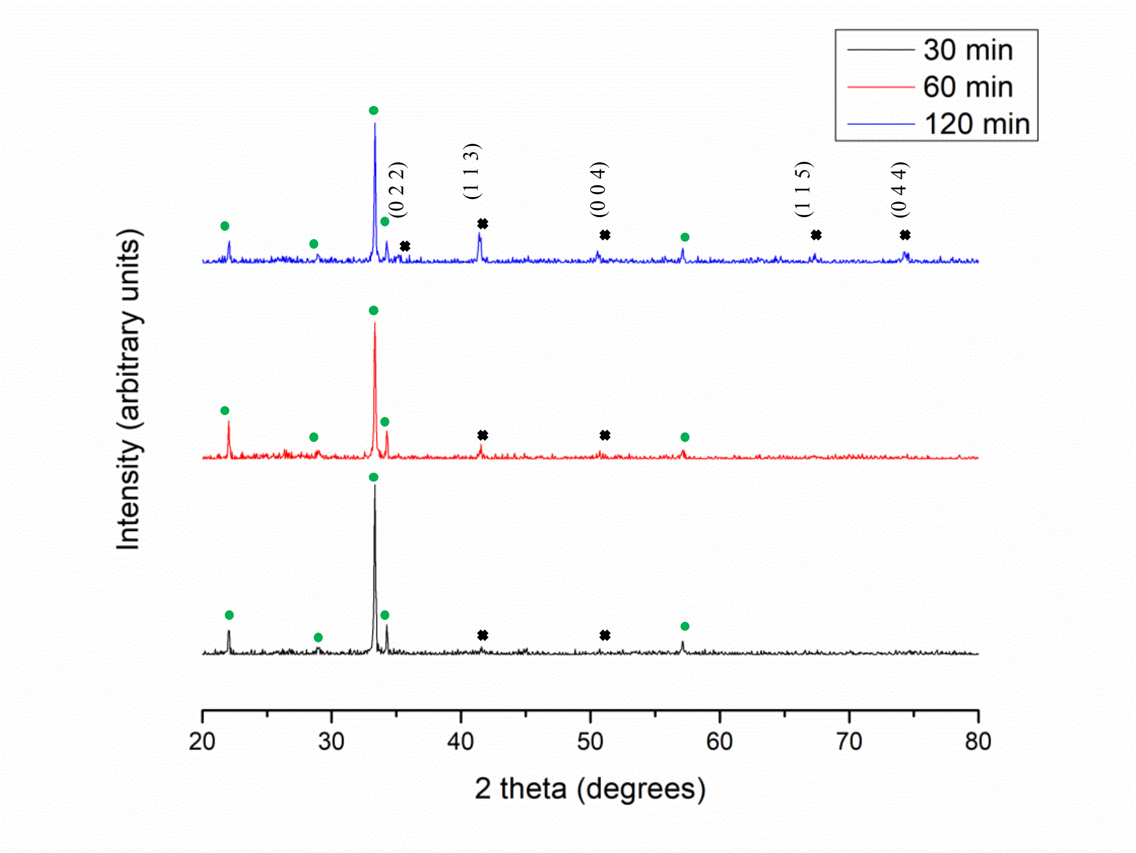

Figure 6.1 XRD of films deposited for various times with P_r= 150 rpm (magnetite peaks are denoted by black squares, substrate peaks are denoted by green circles)

Figure 6.2 illustrates the evolution of the hierarchical microstructure of films deposited at 150 rpm. At the initial stages, after 15 mins of deposition, the film consisted of several interwoven hexagonal plates of varying sizes (typically 1-5 µm). Their thicknesses varied from a few tens of nanometers to a few microns. This morphology is typical of the green rust phases that belong to the rhombohedral crystal system[58]. After

30 mins of deposition, the microstructure of the film consisted of densely packed clusters of several hundreds of magnetite nanoflakes. The size of the clusters varied from 5-10 μm. Nanoflakes were 35-50 nm thick and 200-400 nm wide. An important observation was that their edges were not perfectly smooth and showed nanoscale dimples, roughness and striations. Some of them were also decorated with small 50-100 nm sized nanoparticles. On depositing for 60 mins, the overall size of the clusters remained the same (5-10 μm). However, they were made up of more coarsened (40-60 nm thick) and densely packed nanoblades. A majority of the nanoblades now showed tapering edges. There was also an increase in nanoparticles decorating the nanoblade surfaces. After 120 mins, some of the clusters appeared to have fused together to form larger clusters. As a result, their sizes had a much broader range between 5-20 μm. Further, the nanoblade density within them increased. Superficial regions were encrusted with nanoparticles while those closer to the substrate had little or no nanoparticles on them.

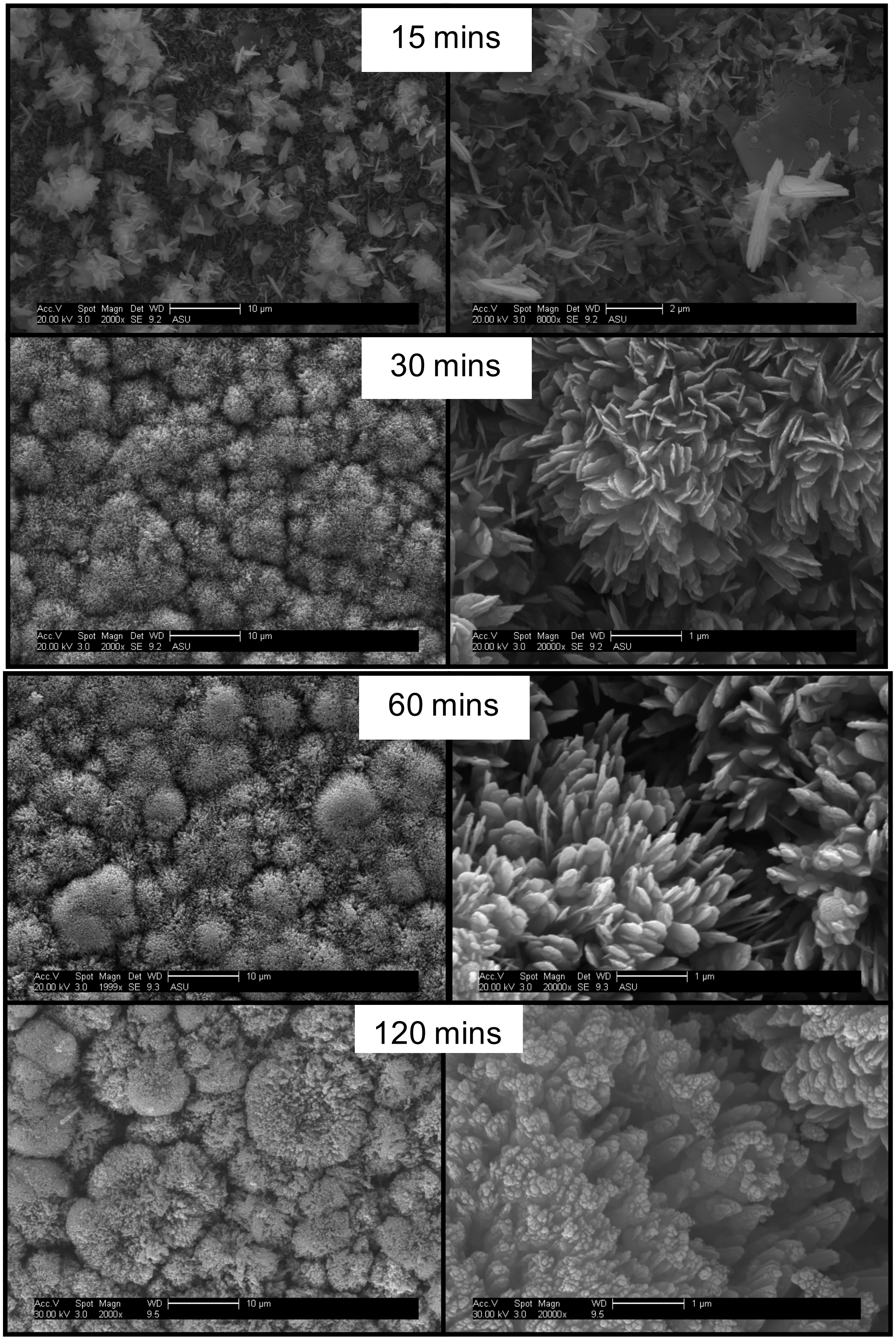

Figure 6.2 Morphological evolution of films deposited with P_r= 150 rpm

The phase evolution of films deposited at 200 rpm was similar to the 150 rpm deposition. After 15 mins, the film deposited was green-blue in color and was confirmed to be made up of green rust (I) by electron diffraction. At 30 mins, the film turned black and consisted of magnetite. The intensity of the magnetite peaks in XRD then progressively increased with increase in deposition time to 60, 90 (Figure 6.3) and 120 mins (not shown here).

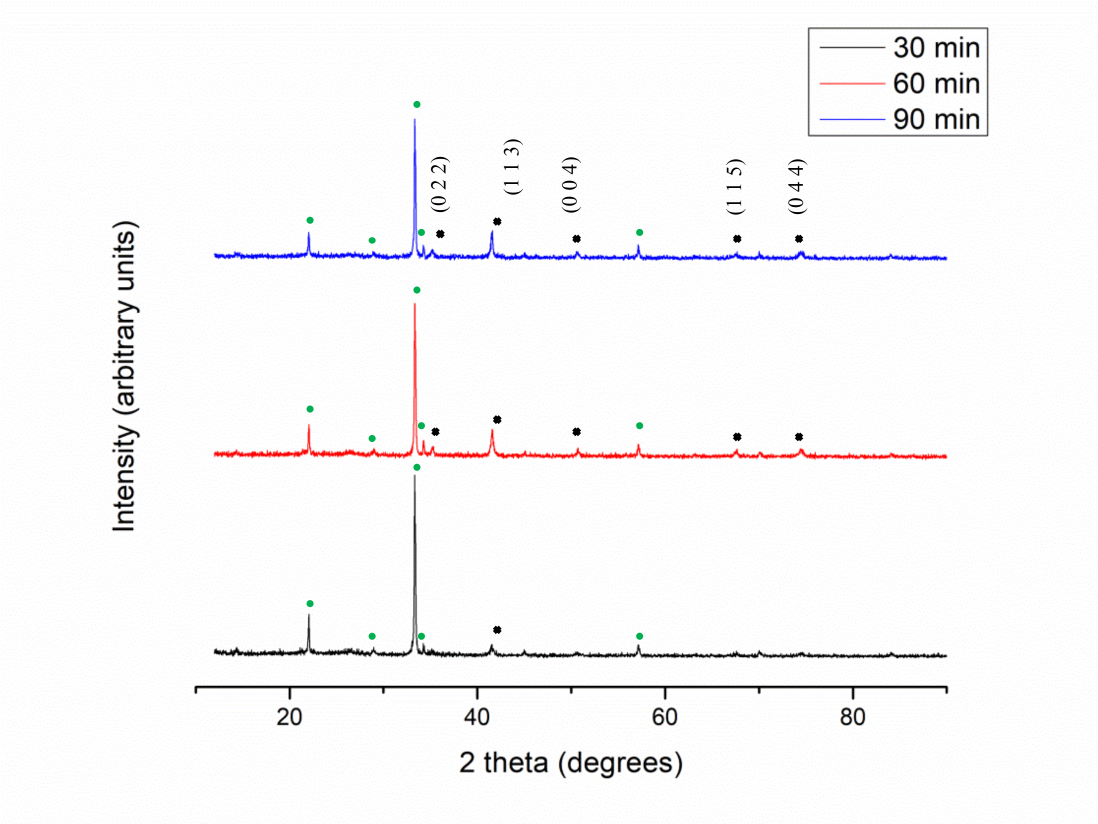

Figure 6.3 XRD of films deposited for various times with P_r= 200 rpm (magnetite peaks are denoted by black squares, substrate peaks are denoted by green circles)

Figure 6.4 illustrates the evolution of the hierarchical microstructure of films deposited at 200 rpm. The green-blue film obtained after 15 mins consisted of interwoven hexagonal plates 1-5 μm in size. At 30 mins, the black colored film consisted of 5-10 μm sized (densely packed) clusters of several hundred magnetite nanoflakes. The nanoflakes were 35-50 nm thick and 500 nm – 1 μm wide. Nanoscale roughness at the flake edges were very evident, appearing as a combination of edge cuts (dimples) and topological prominences corresponding to nanoparticles. The flat faces of the flakes were encrusted with 50-100 nm nanoparticles. After 60 mins, a new structural organization was observed. Some of the clusters now consisted of columns of stacked mosaic discs, although, numerous nanoflakes still existed within the clusters. Their surfaces were coated with coarsened nanoparticles of varying sizes, suggesting that crystal nucleation was accompanied by continuous reorganization. This was further evident when the deposition time was increased to 90 and 120 mins leading to the disappearance of nanoflakes altogether within the clusters. Only uniform 3-10 μm long columns of stacked mosaic discs that grew out of the substrate plane remained.

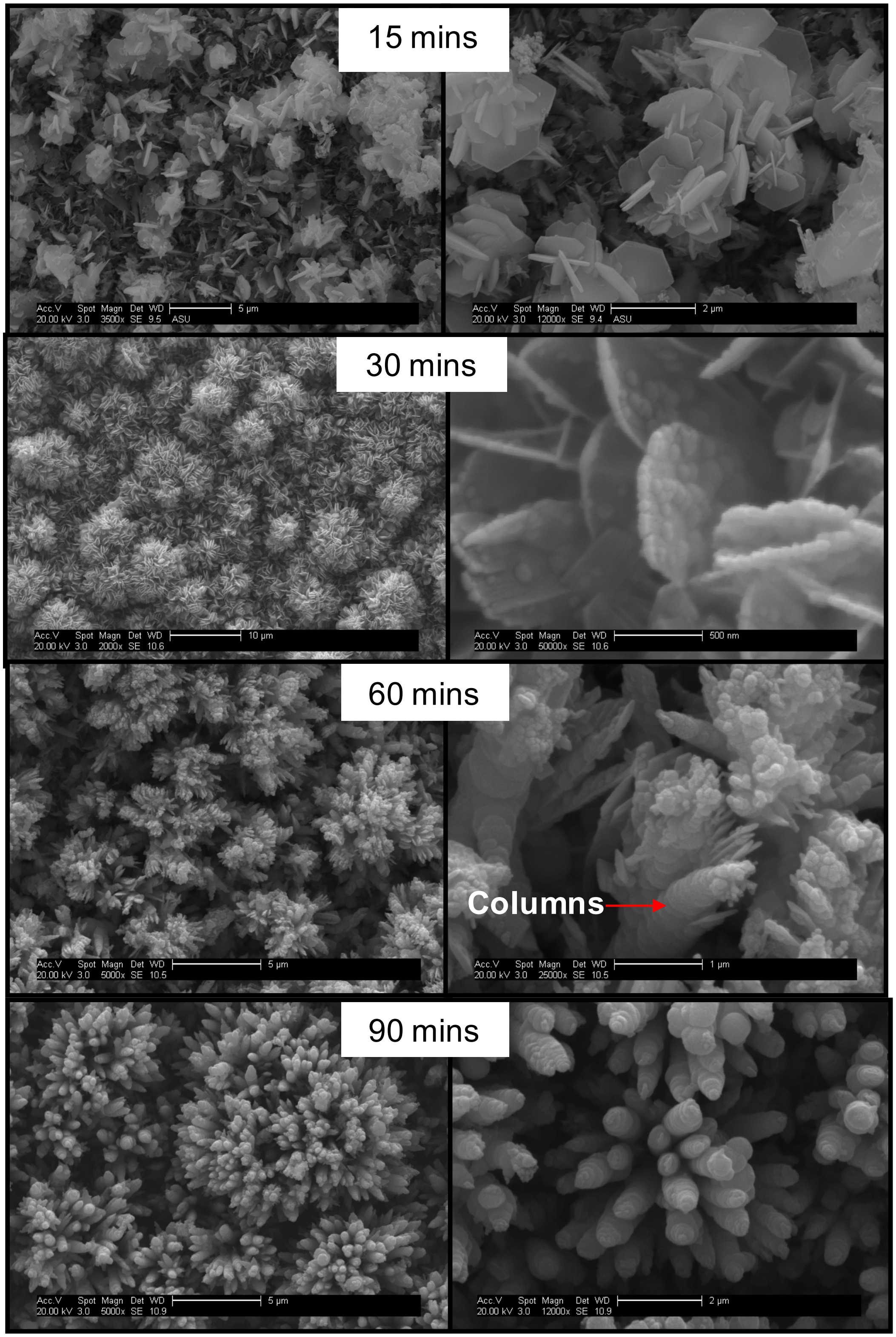

Figure 6.4 Morphological evolution of films deposited with P_r= 200 rpm

Based on the above observations, a combination of topotactic transformation, self assembly/reorganization and coarsening processes is suggested in the evolution of phase and microstructure of the magnetite films. A detailed description of these processes is explained below.

Growth mechanisms of hierarchically structured porous magnetite films:

The initial stages of deposition up to 30 mins were identical for both 150 rpm and 200 rpm platen rotation rates. Upon reaction between precursor solution droplets on the substrate, the nucleation and growth of hexagonal plates of green rust (I) occurred. Figure 6.5a shows a low magnification TEM image of the hexagonal plates. The SAED pattern of one such plate (Figure 6.5b inset), confirmed that this phase was the iron hydroxycarbonate phase[58, 59]. Owing to the layered/lamellar nature of green rust (and hence high surface energies), they aggregate to form intertwined clusters to decrease their surface energies. This phase transformed into magnetite after 30 mins. The corresponding change in morphology was from hexagonal plates to nanoflakes and their assembly into more uniform clusters (Figures 6.2 and 6.4). An additional structural feature observed was nanoparticles on the surface of the nanoflakes.

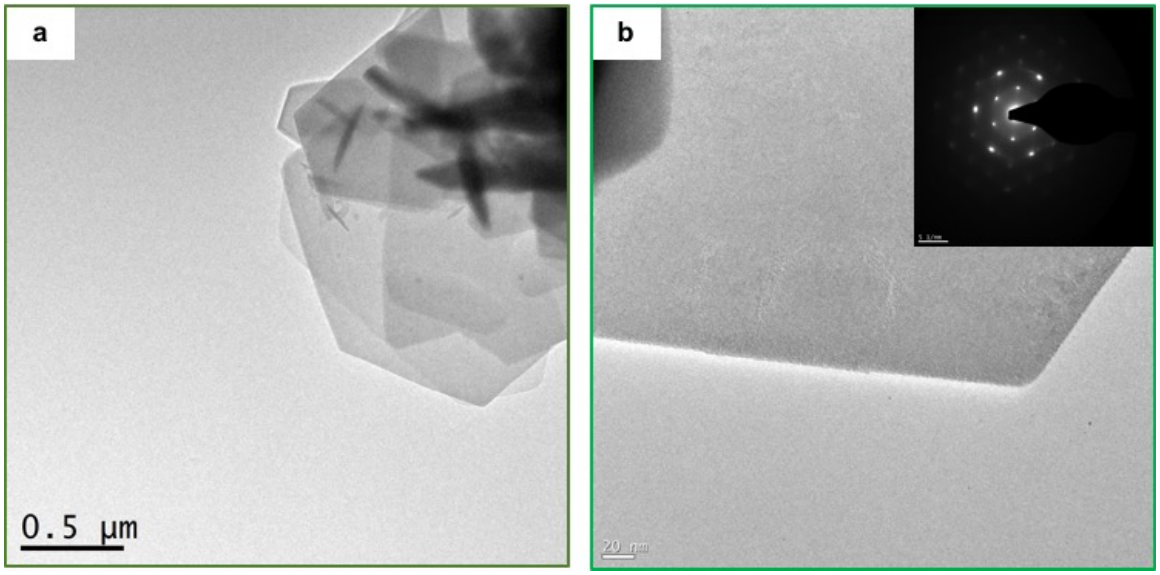

Figure 6.5 (a) Low magnification TEM image of green rust platelets, (b) A green rust plate and its corresponding SAED pattern (inset)

As described in chapter 3, the green rust phase is a layered compound with the layers made up of edge sharing octahedrons with iron (Fe^{2+} and Fe^{3+}) in their centers. The layers are held by the carbonate anions. Magnetite on the other hand is made up of edge sharing FeO_6 octahedrons (with either Fe^{3+} or Fe^{2+} at their centers), that form an open network stabilized by individual Fe-centered tetrahedra, which connected with the network via their corners. Figure 6.6 illustrates polyhedral models of the two phases. It is evident from these representations, that the $[1\ 1\ 1]_R$ direction of the green rust phase (R -3 m structure) is parallel to the $[1\ 1\ 1]_C$ direction of magnetite (F d -3 m structure) and have similar symmetry. This relationship is favorable for the topotactic transformation of green rust (I) to magnetite. This transformation was described by A.L.Mackay [48] and has been extended to structural analogs of other transition metal hydroxides and their oxides [56, 60-62]. Mackay proposed that green rust transformed to spinel magnetite via dehydration.

In other words, it only involved the loss of water layers and migration of Fe ions into new positions[48].

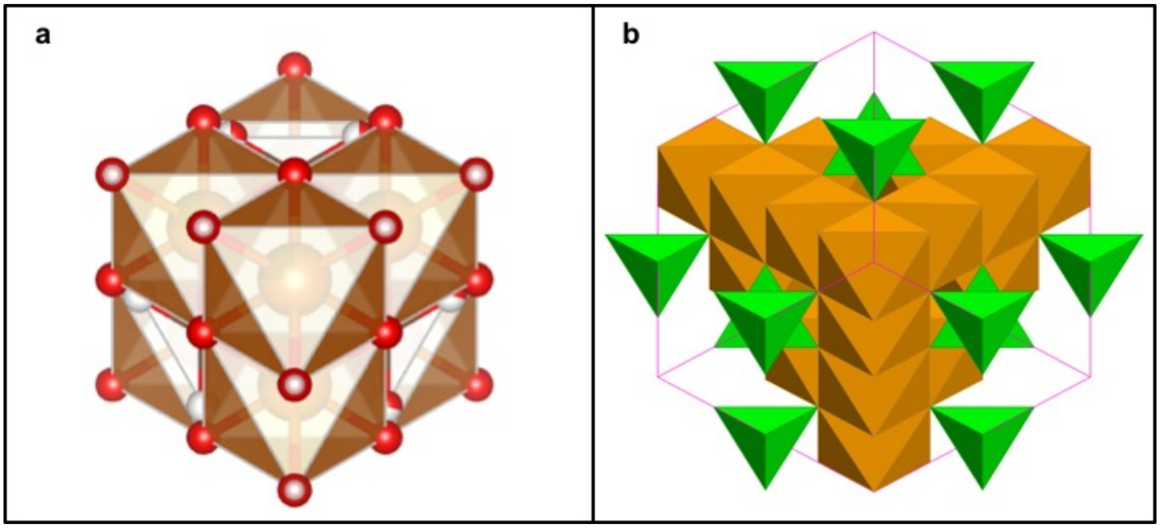

Figure 6.6 Polyhedral representation of the crystal structures (created using VESTA 3[63] and *CrystalMaker*®[64] softwares) of (a) iron hydroxycarbonate (rhombohedral axes) and (b) magnetite, as seen from [1 1 1] directions.

Magnetite nanoflakes obtained after 30 mins of deposition occurred as a result of the above topotactic transformation (TT). This was confirmed by the absence of green rust peaks in the XRD pattern (due to its complete consumption by solid state reaction) and by the product magnetite retaining its anisotropic morphology. An additional aspect of TT is that, if the product phase is denser than the precursor phase, the product crystal will contain pores or cracks due to the volume contraction associated with the transformation [2]. In Fe-bearing compounds, the density increases from hydroxide to oxyhydroxide (typically 2.5 - 4 g/cc) to oxide phases (density of magnetite = 5.1-5.2 g/cc) [49]. Hence, the density of magnetite (oxide) is greater than that of the green rust (oxyhydroxide). Consequently, pores and cracks were observed in a high magnification SEM image as well as a TEM image of a nanoflake (observed as contrast variations within the nanoflake) (Figure 6.7). The latter also showed a large number of magnetite nanoparticles constituting the nanoflake. This is because the precursor phase in TT serves as a heterogeneous nucleation surface and induces the nucleation of several product phase nuclei (which are crystallographically oriented in the 3-D crystal matrix of the precursor) [29]. Nanoflakes further associate to form organized clusters in order to decrease their surface energy.

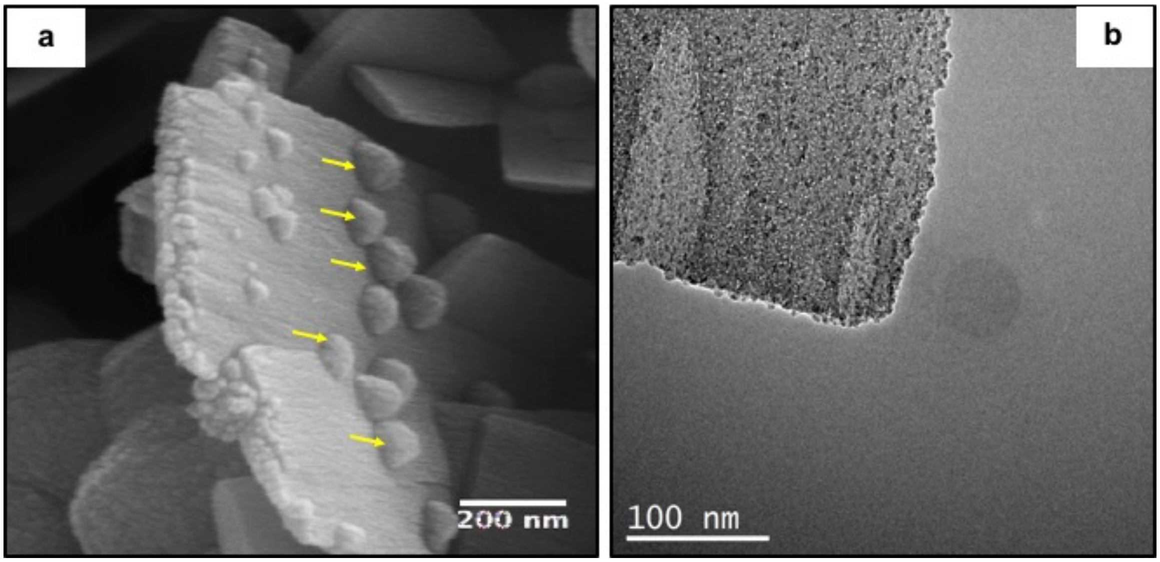

Figure 6.7 (a) SEM image of a nanoflake showing cracks on its surface (the arrows show epitaxially growing magnetite crystals) (b) TEM image of a nanoflake showing contrast variations and constituent nanoparticles

The crystallographic relationship between the green rust and magnetite can also lead to epitaxial growth of magnetite on the surface of a transforming nanoflake. Epitaxy involves the formation of a secondary crystal on the crystal face of another or same material. Since the spin spray process involves the continuous supply of fresh solution onto the substrate, epitaxial nucleation of magnetite nuclei occurred in conjunction with the topotactic transformation. This was confirmed by the presence of nanoparticles on the surface of the nanoflakes (Figure 6.7a).

The subsequent stages of microstructural evolution involved further nucleation of magnetite nanoparticles and their re-organization and coarsening. This re-organization (and hence, the final morphology) was dependent on the rotation speed of the platen. After 60 mins at 150 rpm, nanoflakes had grown in length to about 3-5 μm but not in width. Their edges tapered towards the apex and, as a result, exhibited a blade-like morphology. This taper showed that the growth front was along the longer axis. Their thicknesses increased (40-60 nm) as well but not as fast as their lengths. Some nanoblades exhibited slight lateral shrinkage which is attributed to coarsening or Ostwald ripening. Smaller spherical nanoparticles continued to exist superficially on the nanoblades confirming the continual nature of magnetite nucleation at these stages (due to constant supply of fresh reactants). These nanoparticles would eventually fuse with or undergo Ostwald ripening to increase size of the nanoblades. This was evident with increase in the length and thickness of the nanoblades after 90 and 120 mins. Figure 6.8 summarizes the growth mechanisms and morphological evolution for films deposited at 150 rpm.

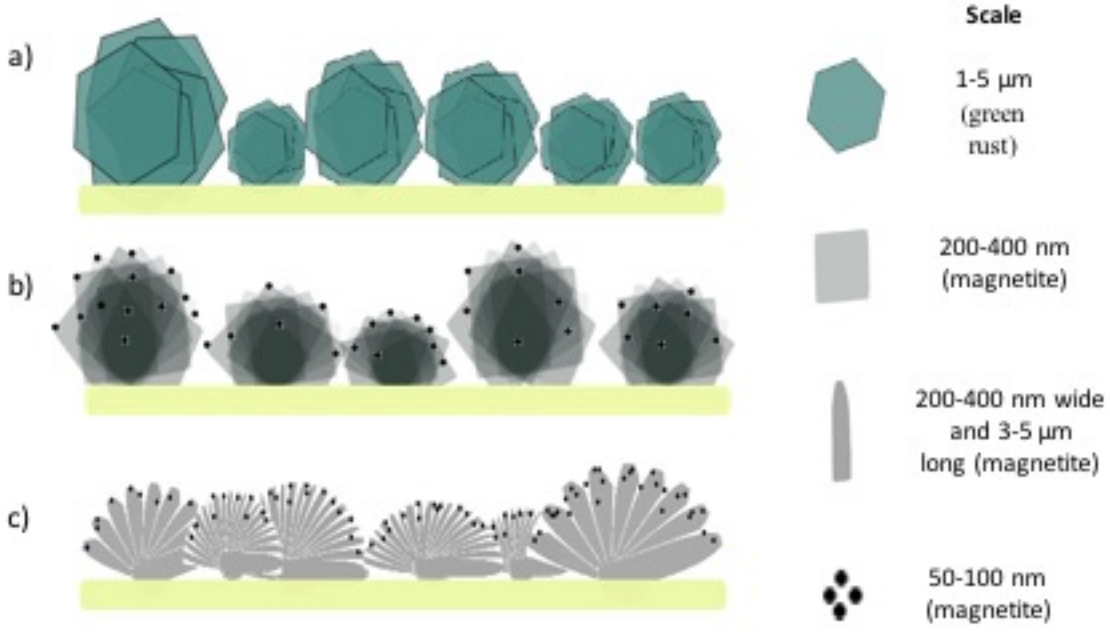

Figure 6.8 (a-c) Schematic illustration of growth mechanism of films deposited at P_r= 150 rpm. The dark dots in b) and c) represent nucleating magnetite nanoparticles

After 60 mins at 200 rpm, columnar stacks of mosaic discs began to form by self-assembly and reorganization of magnetite nanoparticles nucleating on the surface of the nanoflakes. By 90 mins (and even after 120 mins), only the columns existed. At higher platen rotation rates, fresh reactant solutions were depleted in the plane of the substrate due to their short residence times. As a result, crystal growth and reorganization were biased towards the source of solutions, which was the nebulizers placed perpendicular to the substrate. Hence, most of the columns were perpendicular or nearly perpendicular to the substrate (Figure 6.9). Figure 6.10 summarizes the growth mechanisms and morphological evolution for films deposited at 200 rpm.

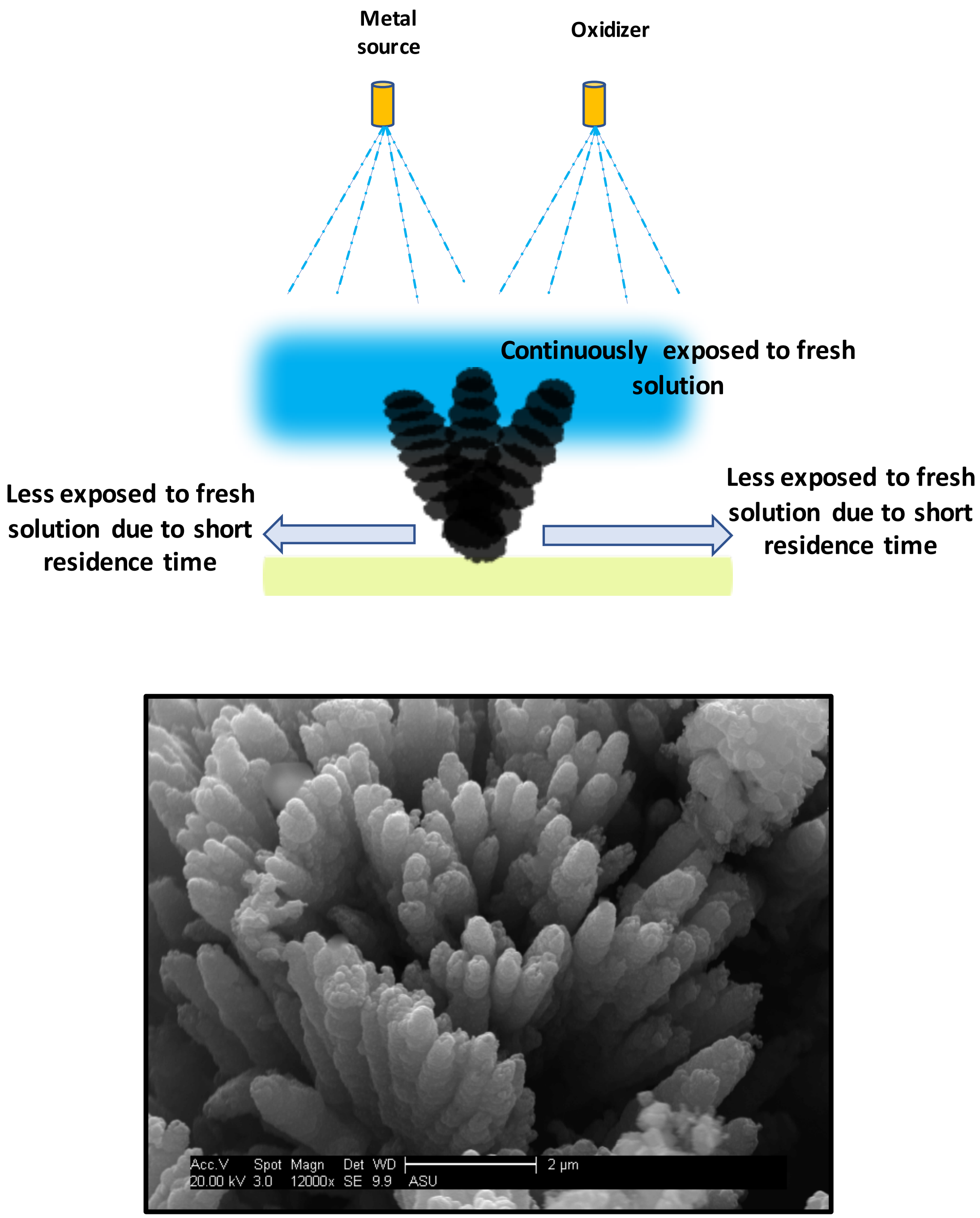

Figure 6.9 Schematic illustration of preferential vertical growth of columns (above) and an SEM image (below) depicting the same

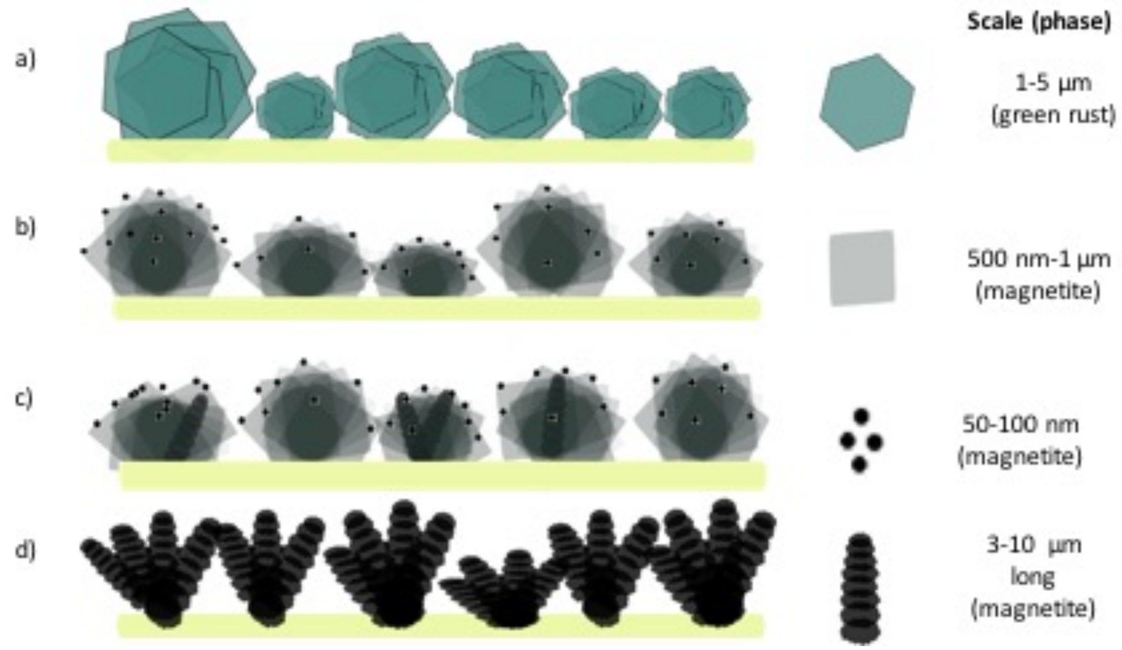

Figure 6.10 (a-d) Schematic illustration of growth mechanism of films deposited at P_r= 200 rpm. The dark dots in b) and c) represent nucleating magnetite nanoparticles

6.2 Time resolved microstructure evolution of dense magnetite films:

Dense magnetite films were obtained when low [HCO_3^-] or [Fe^{2+}] concentrations (Figure 4.15) were used in the oxidant solutions. Time resolved experiments were carried out to understand the microstructural evolution for one such dense film deposited with [Fe^{2+}] = 16.7 mM and [HCO_3^-] = 10 mM. The platen rotation speed (P_r) was fixed at 200 rpm. Deposition was carried out separately for 5, 20, 60, 90 and 120 mins, following which the films were analyzed for phase purity using X-ray and electron diffraction, and SEM for microstructural analysis.

Owing to the low deposition rates of these films, X-ray diffraction was not helpful for phase identification at the early stages of deposition. This was primarily due to the extremely low thickness (a few tens of nanometers) of films and, hence, weak signal intensities. Additionally, the X-ray intensities from the mineral embedded in the PEEK substrates were sufficiently high to obscure the magnetite peaks. In order to overcome this problem, the 5 min deposition was carried out directly on a Cu TEM grid attached to the substrate. Phase identification was then carried out by HRTEM analysis. Figure 6.11 shows SEM and TEM images of this film. It consisted of several 10-50 nm wide and 100- 150 nm long spindle shaped particles. These were in-turn made of smaller sub-units, thereby exhibiting a mosaic structure. The internal porosity within the spindles and their rough surfaces alluded to their formation by aggregation of the smaller sub-units. An FFT diffractogram obtained from a HREM image of a spindle showed single crystalline spot pattern despite their mosaic structure. This indicated their formation by oriented aggregation [12, 65, 66]. The spot pattern corresponded to hematite (α-Fe_2O_3). Similar morphologies of hematite were synthesized in solution by Ocana et al.[12], and Frandsen et al.[66]. The mechanism for their formation was proposed to occur by the aggregation of sub-units of akaganeite (β-FeOOH), an iron oxyhydroxide phase that belongs to the monoclinic crystal system. Analysis of our sample showed only the mosaic spindles of hematite. While this suggested the involvement of a similar aggregation mechanism, the actual presence of akaganeite (β-FeOOH) was not detected.

Deposition for the subsequent time intervals were not carried out directly on the TEM grid as films became too thick (>100 nm) for observation by TEM. At the same time, a film deposited for 20 mins was still considerably thin for XRD. In order to improve peak intensity and resolution, XRD was instead carried out at grazing incidence (source fixed at 5° with respect to the sample) for a narrow 2θ (detector) range of 40°-43°. This range was chosen as the 100% intensity peak (corresponding to the (1 1 3) plane) of the spinel structured iron oxides (magnetite and maghemite) was between 41.4° to 41.7°. A broad and low intensity peak with its center at 41.69° (Figure 6.12) was observed in the corresponding GIXRD (grazing incidence XRD) pattern. While this confirmed that the transformation from the hexagonal hematite (α-Fe_2O_3) to spinel structure had begun with 20 mins of deposition, the film obtained was dark brown in color. Since magnetite films are typically black or grey in color, this film was likely maghemite (γ-Fe_2O_3). At subsequent deposition times of 60, 90 and 120 mins, films showed more distinct peaks of the spinel phase, with a corresponding increase in peak intensities and sharpness with deposition time (Figure 6.13). These films were all grey in color, thereby confirming the phase to be magnetite.

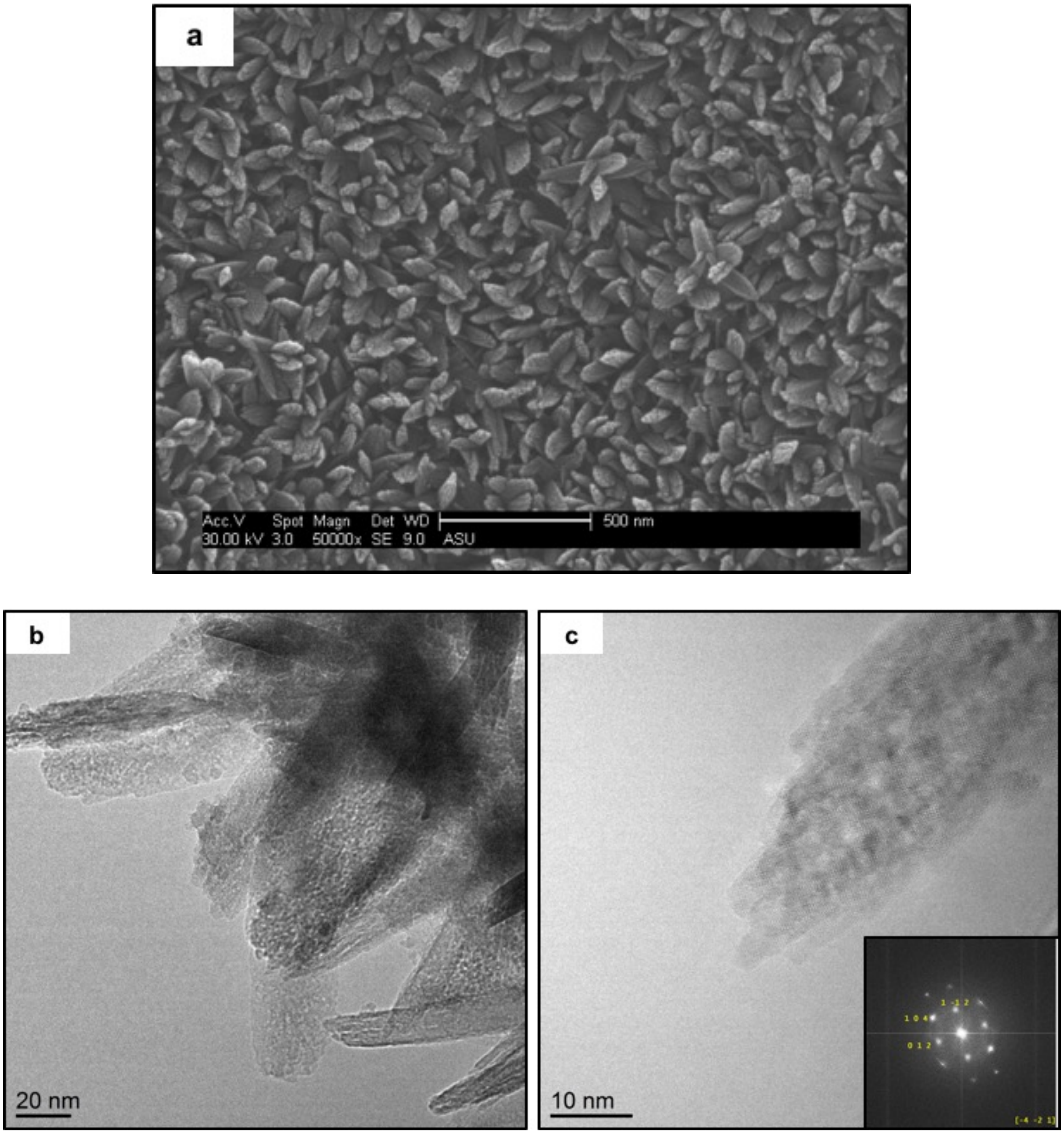

Figure 6.11 (a) SEM image of film after 5 mins of deposition (b) TEM image showing mosaic nature of spindles (c) HRTEM image and FFT (inset) of a single mosaic spindle

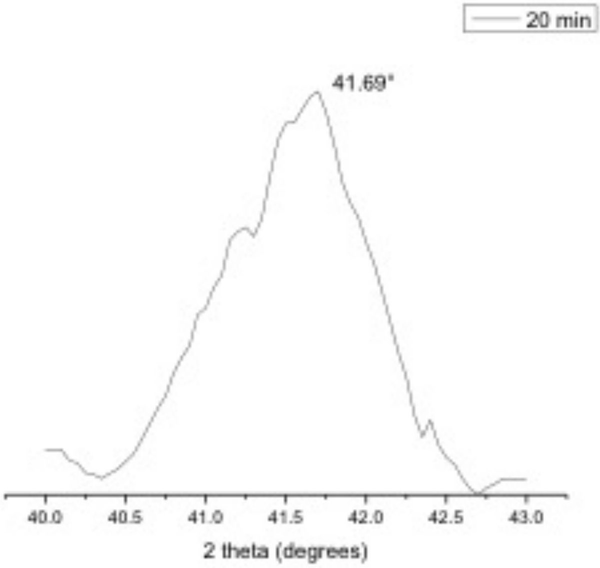

Figure 6.12 GIXRD of film deposited for 20 mins showing a broad (1 1 3) maghemite peak

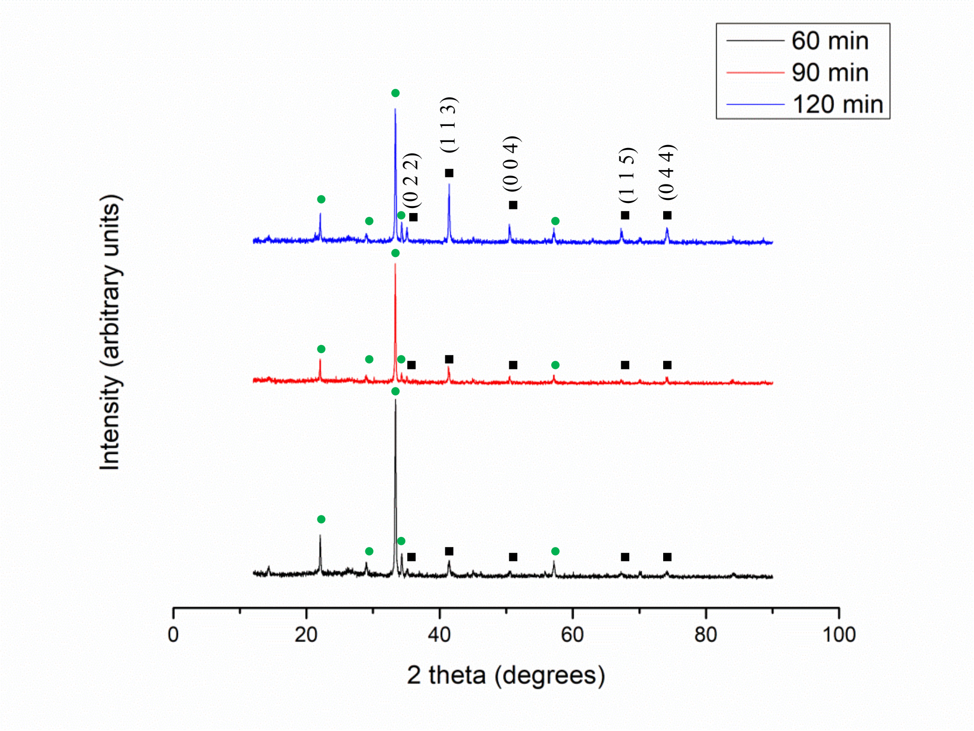

Figure 6.13 XRD of films deposited at 60, 90 and 120 mins (magnetite peaks are denoted by black squares, substrate peaks are denoted by green circles)

Figure 6.14 shows the morphological evolution of these films. After 20 mins deposition, the maghemite film comprised nearly monodisperse ~100 nm mosaic spherical clusters. They were made up of smaller 10-20 nm primary nanoparticles. In several regions of the film, mosaic spheres further assembled to form 1-D arrays/chains or even 2-D layers. However, at this stage, the film was still fairly porous. The magnetite film after 60 mins of deposition was comparatively denser and consisted of clusters made up of 200-300 nm sized mosaic faceted crystals. The size of the clusters was not uniform and varied from a few tens to few hundreds of nanometers. The faceted crystals were made up of smaller 15-50 nm sized nanoparticles. Even though the plan view SEM images showed an apparent porous structure, a cross-section image revealed dense packing within the film. It can therefore be concluded that the voids seen in the former were restricted only to the top-most regions (surface) of the films. Further increase in time to 90 and 120 mins led to continued increase in density and thickness of the films. The facets became more evident in the mosaic crystals, and were typically shaped like truncated octahedrons.

An important observation was the transition in the cross-sectional structure of the film from 60 to 120 mins. At 60 mins, the cross-section of the film was characterized by isotropic or equiaxed crystal shapes. With increasing thickness of the film, at 90 mins, an apparent preferential growth outward from the plane was observed. At 120 mins, the cross-section was made up of columns of varying thicknesses.

Crystallite sizes were calculated from XRD peak broadening by applying the Scherrer equation (using MDI Jade9 software) to the (1 1 3) peaks (100 % intensity peak of magnetite) of the samples deposited at 20, 60, 90 and 120 mins. At 20 and 60 mins, the sizes were 10.1 nm and 54.1 nm. These sizes were comparable to the size of primary nanoparticles (calculated from SEM) that made up the mosaic assemblies in the films. For films deposited for 90 and 120 mins, the crystallite sizes could not be calculated from XRD as they exceeded the 100 nm limit for application of the Scherrer equation. In comparison, the SEM images taken at these time intervals showed the presence of 15-50 nm sized nanoparticles (that made up the mosaic faceted crystals) (Fig. 6.15). The difference between the two suggested the involvement of low temperature sintering or coarsening between the nanoparticles and hence, larger crystallite size (as indicated by XRD).

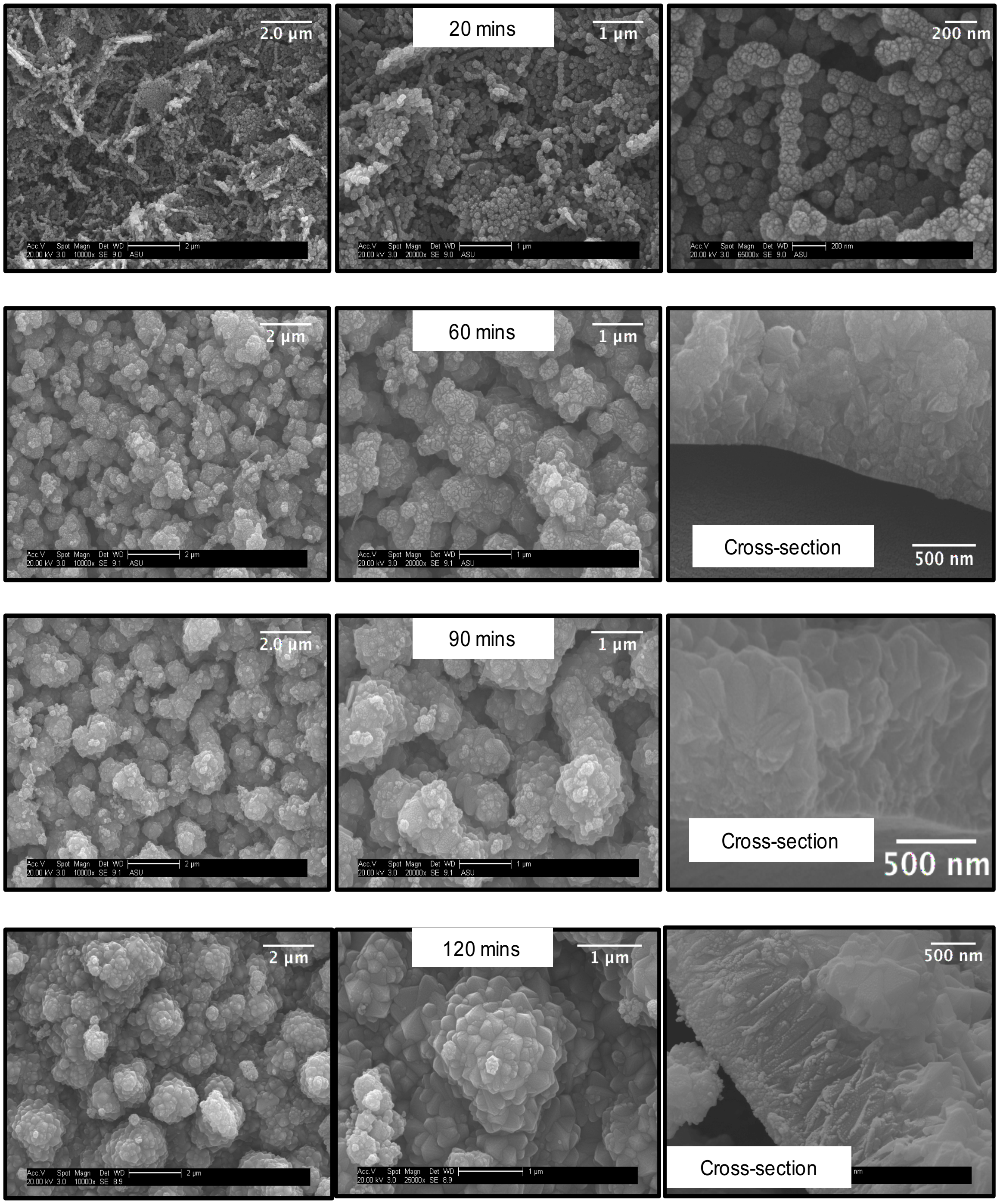

Figure 6.14 Morphological evolution of dense magnetite films

Based on the above observations, it can be said that the crystallization of dense magnetite films also involved similar phenomena to that of porous films. These were solid-state phase transformations, self-assembly/reorganization and coarsening processes. However, the nature of phase transformations and rate at which these processes occurred were different. A detailed description of these processes is explained below.

Growth mechanisms of dense magnetite films:

As discussed in the previous section, the very early stages of deposition (5 mins) began with the formation of spindle shaped hematite nanoparticles. Based on their mosaic structure, it was proposed that a precursor oxyhydroxide phase, akaganeite (β-FeOOH) may have been involved in the formation of the hematite spindles. After 20 mins of deposition, hematite (α-Fe_2O_3) underwent phase transformation to form spinel structured maghemite (γ-Fe_2O_3).

Although hematite is the more stable polymorph in bulk, energetic cross-overs at the nanoscale leads to maghemite being comparably or more stable (depending on particle size) [67]. It has also been suggested that hematite nanoparticles may possess maghemite like surface structures [67]. Additionally, such phase transformations are often catalyzed by the presence of Fe^{2+} in the synthesis environment[68-71]. This is due to the feasibility of electron-hopping between the surface adsorbed Fe^{2+} and Fe^{3+} in the bulk of the oxide [70]. Mackay[48] described the transformation between these two phases to be epitactic rather than topotactic. He reasoned that, although these two phases had considerable similarity, going from one phase to the other required relatively large positional shifts of oxygen.

The phase transformation observed after 20 mins of deposition occurred via the above mechanism. Hematite spindles formed at the early stages are constantly exposed to Fe^{2+} from fresh reactant solution that continued to be sprayed. This served to trigger the solid-state phase transformation to maghemite. Nucleating maghemite nanoparticles (~10-20 nm), then progressively underwent self-assembly: first, into ~100 nm mosaic spheres, and then assembled into 1-D arrays/chains and 2-D layers.

Maghemite and magnetite have a very close structural resemblance to one another, and that aids the formation of a continuous solid solution of these phases[67]. Once again, the adsorption of Fe^{2+} from the incoming spray on maghemite served to induce its phase transformation to magnetite. By 60 mins of deposition, the film had completely turned grey, suggesting complete transformation to magnetite. At this stage, cross-section SEM images showed that the films were dense. Several clusters made up of mosaic faceted crystals were observed. With time, (nucleating and) self-assembling magnetite nanoparticles did so along specific crystallographic directions to develop facets. These facets continued to become more distinct with increase in deposition time to 90 and 120 mins. Figure 6.15 shows octahedrally shaped mosaic crystals with beveled edges from a film deposited for 120 mins. It is evident that it is made up of smaller primary nanoparticles. Comparison with standard crystal habits of magnetite showed that the triangular faces corresponded to the {1 1 1} family of planes and the truncated faces corresponded to the {1 1 0} family of planes [72]. Wulff model and DFT studies by Santos-Carballal et al. [73] showed the equilibrium shape of magnetite crystals to be made up of (1 0 0) planes truncated at the corners by the (1 1 1) planes. However, the most common habits of particulate crystals in synthetic and natural environments were octahedrally shaped crystals that were sometimes truncated by (1 1 0) planes[74]. This showed that the self-assembly of magnetite nanoparticles into ordered faceted crystals in our present case, was largely thermodynamically driven (presence of (1 1 1) faces). The appearance of (1 1 0) planes is attributed to kinetic factors during synthesis.

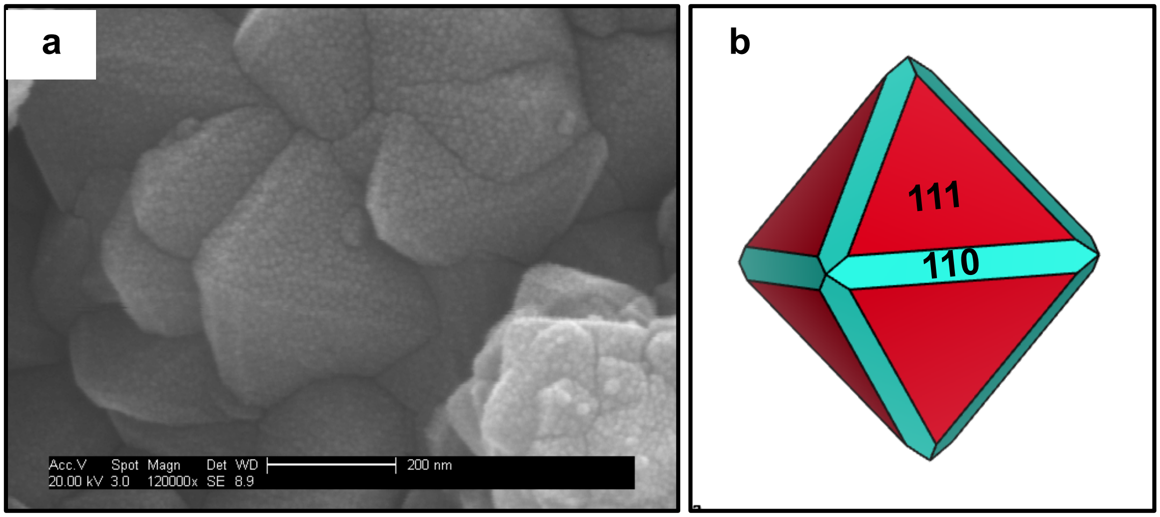

Figure 6.15 (a) Mosaic truncated octahedron (b) magnetite crystal shape generated using VESTA 3 [63] (red faces correspond to {1 1 1} family of planes and blue faces correspond to {1 1 0} family of planes)

6.3. Comparison of growth mechanisms with other studies on oxide deposition via chemical solution:

Traditionally, two major growth mechanisms were described for oxide thin film deposition from aqueous solutions[22]. These were a) ion-by-ion growth that involved the adsorption of ions from solution onto the substrate followed by heterogeneous nucleation of solid and growth and, b) particle attachment or cluster deposition in which colloidal particles nucleated in the bulk of the solution, aggregated and eventually adhered to the substrate due to electrostatic and/or Van der Waal's forces. For a given oxide material, deposition could be switched from one regime to another by varying supersaturation of the solution. However, more recently, these two mechanisms have been identified to be just the limiting cases by Parikh et al.[75]. The same authors acknowledged the difficulty in attributing thin film growth to a singular process owing to the additional possibility of formation of amorphous or crystalline precursor phases. More importantly, while the above mechanisms were based on extensive research efforts in aqueous thin film deposition of various oxides and chalcogenides, the majority of these studies involved deposition by immersion of static substrates in liquid solutions (chemical bath deposition, liquid phase deposition, etc.). These solutions would then decrease in supersaturation with time. This was clearly different from the spin spray deposition that involved constant supply of fresh solutions on the rotating substrate followed by its removal by spinning.

Perhaps, a more similar process was the liquid flow deposition (LFD) method in which fresh precursor solutions were continuously flowed over a substrate placed in the deposition chamber[27]. Previously, Abe et al. used this technique to deposit spinel ferrites[76, 77]. In a more recent study by Supothina et al. [27], the SnO_2 film growth by

LFD was attributed to particle attachment rather than heterogeneous nucleation. The possibility of involvement of precursor phases to SnO_2 was not discussed. Lipowski et al.[78] have discussed the importance of a transient amorphous phase in solution during the deposition of ZnO films. They found that the formation of high quality films was related to the presence of the intermediate amorphous phase in solution.

Considering the growing body of evidence that particle mediated crystallization pathways are crucial to the growth of crystals in solution, we have found through our study that such mechanisms also play a vital role in microstructural development of magnetite films deposited by spin spray deposition. We have additionally identified the different precursor phases to magnetite and described their transformations to the magnetite. Since our films were deposited in the micro-droplet regime (implying micro-volumes of solution), it was more likely that the early stages of nucleation of precursor phases was heterogeneous and happened when the droplets reacted on the substrate. However, homogeneous nucleation within the droplets cannot be completely ruled out. As pointed out by Deguire et al. [79], unambiguous determination of which process dominated is not possible by mere *ex-situ* analysis of film microstructure.

6.4 Role of intermolecular forces in film deposition and nanoparticle self-assembly:

Films deposition by SSD involved the aggregation or self-assembly of nanoparticles. The intermolecular forces involved in bringing about deposition and self-assembly can be sub-divided into:

a) Forces between particles in the solution (in the SSD case, droplets)
b) Forces between particles in solution and substrate (initial stages of deposition)

c) Forces between particles in solution and deposited film (after the entire substrate has been covered by the target material).

The forces between particle surfaces interacting through liquid medium have been described by the Derjaguin-Landau-Verwey-Overbeek (DLVO) theory[80]. According to this theory, the net interaction energy between two surfaces in solution involved contributions from two major components: van der Waal's (vdW) and electrostatic (or Coulombic) forces. This can be expressed as,

$$V_{total} = V_{vdW} + V_{el}$$

vdW forces are attractive in nature and generally exist at short particle separations. On the other hand, electrostatic forces (arising from the electric double layer of charges adjacent the surface in solution) are generally repulsive and prevent the surfaces from coming in contact with one another. Overall, the nature of aggregation, i.e. reversible or irreversible, random or oriented, is dependent on the sum of these interactions. The DLVO theory is extensively used to study particle aggregation (largely identical) in colloidal solutions. It has also been extended to study particle deposition onto flat substrates.

Both vdW and electrostatic forces are key factors in influencing the ordered assembly of nanoparticles. They are particularly sensitive to the size of nanoparticles and nature of solution (pH, concentration etc.). Efforts have been taken to quantify the magnitude of these forces with respect to oriented attachment of nanoparticles in the formation of anisotropic nanostructures in solution. W.He et al.[81, 82] derived analytical expressions for these forces in the case of oriented attachment of spherical nanoparticles to form nanorods. It was found that DLVO forces can be affected by a number of factors such as nanoparticle approach direction (on-axis or off-axis approaches), separation distance, aspect ratio of nanorods and size of nanoparticles.

Other key factors determining the magnitude of DLVO forces, especially, the electrostatic forces are the pH and ionic strength of the solution. The former particularly influences aggregation as it determines how far away the solid nanoparticles are from their iso-electric point. It has been suggested that oriented aggregation of nanoparticles in solution could be expected at pHs closer to the isoelectric point[7]. Most of the experiments in this study were carried out at pH between 8-8.6 which was not very far from the isoelectric point of magnetite (typically 7.2 to 8). This could be the reason for the observation of organized nanoparticle self-assembly.

In spin spray deposition (SSD), an additional aspect of nanoparticle assembly was the mobility of particles within the droplets, as well as, on the substrate. It has been widely accepted that nanoparticle self-assembly occurring in homogeneous solutions are likely due to Brownian motion of particles[7]. The kinetics of aggregation in colloidal solutions are commonly described by models similar to the Smoluchowski model of colloidal growth[7, 10, 83]. However, reliance on Brownian motion alone will require long periods of time to bring about assembly. One could overcome this problem by increasing the temperature or by stirring the solution to increase the frequency of collisions. The SSD, in effect, involved doing both and in much smaller volumes of liquid. Owing to the small size of the droplets, the frequency of nanoparticle collisions can be expected to be higher. This was further amplified by movement of the droplets along the substrate due to the rotating platen. In other words, a co-operative motion of particles due to Brownian effects and fluid movement on the substrate served to bring about self-assembly in SSD.

6.5. Implications of non-classical crystallization in microstructure development of thin films:

It is evident from our studies that the crystallization of magnetite films cannot be described purely by classical nucleation and growth theories i.e., monomer addition (atom-by-atom or ion-by-ion). The involvement of solid precursor phases and their subsequent transformation to the final oxide (magnetite) confirmed crystal growth by non-classical crystallization. Further, such pathways bore a huge influence on the final microstructure of films obtained.

It has been shown that porous magnetite films crystallized by topotactic transformation from layered green rust precursor. This led to formation of anisotropic morphologies (nanoflakes, nanoblades and columns) in the final microstructure of these films. On the other hand, dense magnetite films crystallized via precursor hematite spindles (100-150 nm long) that subsequently transformed to spherical maghemite nanoparticles (10-20 nm) and finally, magnetite. Hence, such films had more isotropic nanoparticle assembly to form mosaic spheres or faceted structures. Additionally, the reason for the poor adherence of porous films was also the formation of the hexagonal plates of green rust. Owing to their large sizes (1-5 µm), they did not adhere well to the substrate and were more likely to be affected (washed away) by the fluid flow than smaller nanoparticles[27]. Dense films adhered very well to substrate owing to the small particle sizes of their precursor phases.

The rate of nanoparticle aggregation and organization also influenced the final microstructure of thin films. Moreover, uniform nanoparticle aggregation was key to obtaining uniform microstructures across the entire substrate. This was achieved by preventing liquid pooling as described in chapter 4. Porous films were obtained when high concentrations of precursor solutions were used. Their growth rates were very high (as high as ~130 nm/min). In other words, the rates of crystal nucleation, transformation and organization were high. As a result, the final microstructure of porous films could be influenced by changing the residence time of solutions on the substrate (varying rotation rate of the platen). Alternately, dense films were obtained for reduced concentrations of precursor solutions. Their growth rates were much lower (~5-50 nm/min). Hence, their microstructure was made up of isotropic nanoparticle assemblies and closer to thermodynamically expected equilibrium morphologies. In effect, the growth of porous films can be viewed as a far-from-equilibrium regime of deposition while that of dense films can be viewed as closer-to-equilibrium deposition.

Through this research, we have gained an understanding of how non-classical crystal growth phenomena can be employed to tailor the formation of hierarchical nanostructures. Hierarchically organized magnetite nanostructures such as those observed in our porous films have been receiving growing attention in the scientific community owing to their high surface areas[84]. This makes them attractive candidates for catalysis and waste water treatment as demonstrated by multiple studies[84-87]. They are also cost-effective as they can be recovered using external magnets. The added significance of our research is the rapid and facile synthesis of such nanostructures onto large area substrates without the use of organic templates for bringing about self-assembly. Previous studies by D. Zhang, Ray et al.[3] have also shown that mosaic grain structures such as those observed in the dense films led to enhanced high frequency magnetic properties. Such films find applications in the electromagnetics field as patch antennas, noise suppressors etc.[31]

6.6 Conclusions:

Time-resolved studies of magnetite deposition by the spin spray process have confirmed the involvement of solid precursor phases prior to the formation of magnetite. These precursor phases have also been identified via TEM analysis. Porous magnetite films formed via transformations from hexagonal green rust (iron hydroxycarbonate) while dense films were deposited via transformations from hematite and maghemite. Involvement of a layered precursor led to the presence of anisotropic morphologies in porous films. On the other hand, dense films were made up of more isotropic morphologies. In both cases, subsequent particle assembly and coarsening led to the formation of hierarchical microstructures. The concentrations of precursor solutions dictated the rate of solid formation, transformation and assembly. This in-turn affected the density and adhesion of the films.

Chapter 7

SUMMARY AND CONCLUSIONS

The focus of this research was to understand the experimental controls of the microstructure evolution of magnetite films deposited at low temperatures from aqueous solutions using a strongly-biased, two dimensional growth process. This was achieved by non-classical crystallization pathways and typically involved nanoparticle self-assembly. Although such pathways have been found to be ubiquitous in crystal growth in natural and synthetic environments, they have rarely been studied in the context of microstructure development in thin film science. In this research, the spin spray deposition (SSD) method was adapted to study magnetite film growth via non-classical pathways. This involved the hydrolysis of ferrous chloride reactant solutions by bicarbonate-based oxidant solutions at low temperatures (70-100°C). The process was very much akin to a gas phase deposition system, but involved the continuous spraying of fresh aqueous reactants. A rotating substrate ensured that the nucleation, growth and assembly of nanoparticles were restricted to a thin, nearly 2-D reaction zone at the substrate surface. As a result, crystal growth very much included the influences of the fluid dynamics of the sprayed reactants and liquid flow on the substrate. An early indication of this came with the observation that homogeneous film microstructures were obtained only when fluid flow was manipulated to operate in the micro-droplet regime (that is, where fluid flow on the substrate can be described by discrete droplets that varied in size between 10-50 microns[31]).

Film deposition was studied as a function of various process parameters such as the number of nebulizers, nebulizer configuration, platen rotation speed and solution chemistry. Two types of films were deposited depending on the concentrations of precursor solutions used. These were either porous and dense films. The former was thicker (typically > 5 µm) and grew at high deposition rates (often reaching >100 nm/min). As a result, they exhibited poor adhesion to the substrate. On the other hand, dense films grew at much lower rates (~5-50 nm/min) and were well adhered.

Microstructures of magnetite films obtained typically consisted of hierarchically ordered crystal morphologies spanning length scales from tens of nanometers to a few microns. Porous films consisted of clusters of agglomerated sub-units such as nanoflakes, nanoblades and columns (anisotropic morphologies). On the other hand, dense films consisted only of isotropic morphologies such as mosaic microspheres and faceted polycrystals. Time-resolved studies carried out to study growth mechanisms showed that an interplay of non-classical crystallization (or crystallization by particle attachment) pathways such as formation of metastable solid precursor phases and nanoparticle assembly (dictated by fluid flow) were the reason behind these differences. The type of precursor phase depended upon the solution chemistry employed to deposit films. Porous magnetite films formed via transformations from hexagonal green rust (iron hydroxycarbonate) while dense films were deposited via transformations from hematite and maghemite. Following these solid-state transformations (to magnetite), nucleating magnetite nanoparticles further underwent self-assembly to give hierarchical microstructures.

Ultimately, the various aspects of this research can be reconciled in the form of a schematic (Figure 7.1) similar to one constructed by A.Rao and H. Colfen in the context of biomineralization.[88]. In our case, the schematic describes crystal growth in spin spray deposition from the perspective of energy barriers associated with various processes such as nucleation, phase transformation, aggregation and growth. Pathway A represents classical crystal growth described by monomer-by-monomer addition. Here, the free energy barrier corresponds to the formation of a critical nucleus of magnetite. It has been clearly demonstrated in this study that this pathway cannot describe crystal growth in spin spray deposition. Rather, non-classical pathways B and C were responsible for magnetite formation and morphological development. At high rates of solid formation or high deposition rates in SSD, pathway B occurred. It involved the formation of a metastable precursor (green rust, hematite etc.) that subsequently underwent transformation to magnetite. Following this nucleating magnetite nanoparticles underwent hierarchical aggregation into polycrystalline aggregates that scaled from a few nanometers to few microns. Aggregates, in certain cases, showed preferential orientation at the nanoscale. This pathway described well, the growth processes involved in the deposition of porous films.

Pathway C occurred when aggregation was slower and more organized. It was attributed to the crystallization of dense films. Pathways B and C are kinetically controlled pathways and hence, their effects are expressed in crystal morphology[89]. Kinetic control in this study was achieved by a combination of quasi-two-dimensional process control and solution chemistry. It is important to note that the final stage represented by bulk magnetite crystals was never reached in this research. All morphologies synthesized showed hierarchical organization of nanoparticles.

The versatility of parameters available to control liquid mobility (and hence, nanoparticle mobility) makes spin spray deposition an excellent method for the development of films with tailored microstructures. An added knowledge of various metastable polymorphs or precursor phases in the system of interest and their transformations could be particularly useful in obtaining desired morphologies.

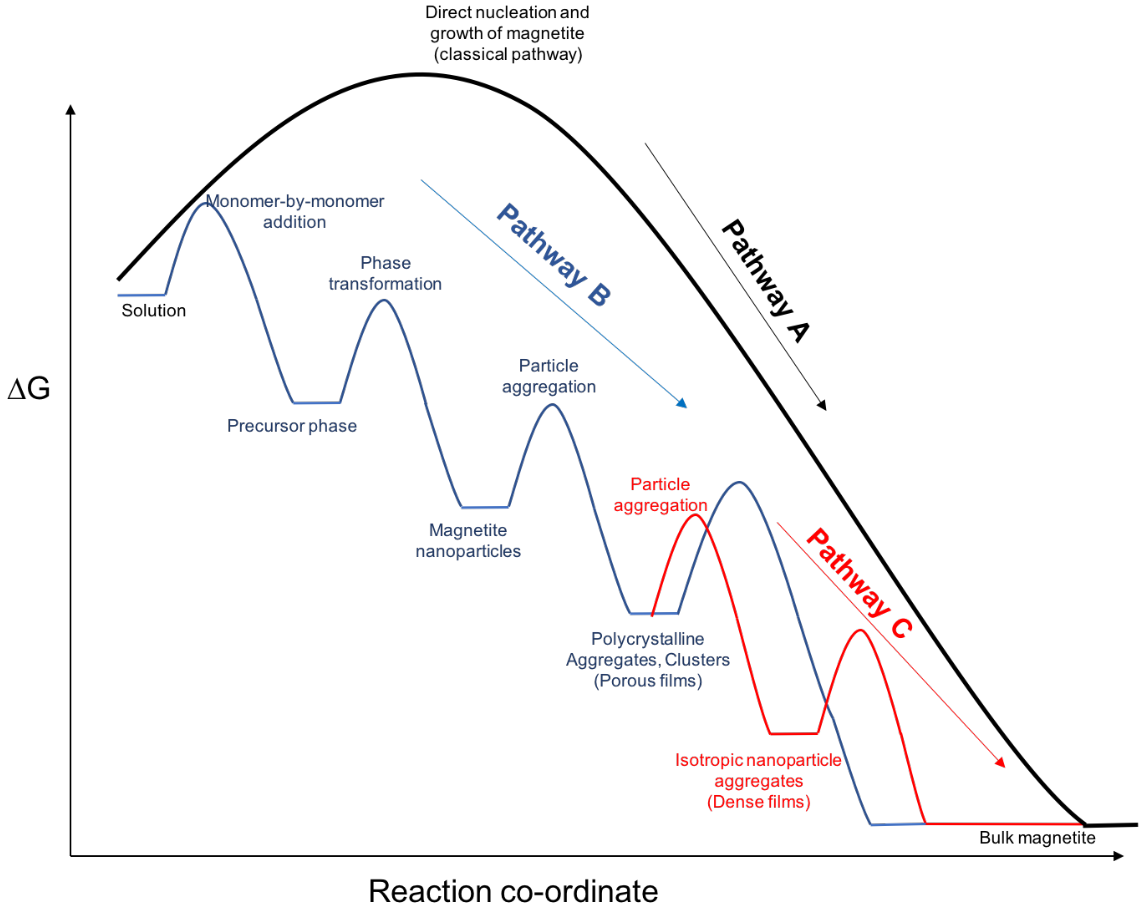

Figure 7.1 Schematic demonstrating the complexity of the free energy landscape (Pathways B and C) in crystal growth by spin spray deposition. Pathway A represents crystal growth

as described by classical pathways.

Perspectives on film growth in spin spray deposition via non-classical crystallization:

Based on our studies, three key mechanistic aspects to magnetite film growth in spin spray deposition via non-classical pathways were identified. These were essentially linked to the process parameters employed to carry out deposition.

1. **Formation of metastable or transient precursor phases:** Magnetite film deposition never actually began with the direct nucleation of magnetite. Metastable solid phases always preceded it. The formation of precursor phases was likely due to kinetic reasons, which is a common observation in material systems such as iron oxides, that exhibit a wide variety of polymorphs (nucleation barriers to amorphous or hydrated crystalline phases are generally lower than that of pure crystalline phases). The initial gestation period of deposition involved the nucleation and growth of the precursor phases, leading to an eventual complete coverage of the substrate. Structural characteristics of the precursor phase can influence the final morphology of magnetite, as was observed with porous films. The formation of anisotropic sub-units of magnetite like nanoflakes and nanoblades were possible only because the layered green rust phase nucleated first. Preservation of structural morphologies of the solid precursor was due to the solid-state transformation to magnetite. This was facilitated by the fact that spin spray deposition was not carried out in homogeneous bulk solution (like in chemical bath deposition), thereby, avoiding dissolution-reprecipitation. Such transformations could be exploited for a targeted approach towards obtaining non-equilibrium crystal morphologies. In other words, by manipulating the solution chemistry to control which precursor phase

nucleates, the structural characteristics of the precursor could be imposed onto the final solid phase. This could be extended to film deposition of all metal oxides that have structural polymorphs such as TiO_2, Al_2O_3, etc.

2. **Solid state transformation to magnetite and disappearance of the precursor phase:** The precursor phases were transient. Following the gestation period, the deposited precursor phases started undergoing solid state transformations (topotactic or structural reorganization) to form magnetite. It was interesting to note that once the transformation to magnetite had begun, subsequent nucleation and growth did not involve the formation of the transient phases again, although the solution chemistry remained the same. The formation of magnetite on the substrate, seeded (or biased) further nucleation of magnetite only. Based on these observations, it was hypothesized that the surface onto which the solutions were sprayed, influenced the nucleating phase. The initial substrate surface was pristine PEEK, which induced the nucleation of either green rust or hematite (depending upon solution chemistry). However, after the entire substrate had been covered with the precursor phase, solutions were instead being sprayed onto what became a substrate of the precursor phase. This was followed by the solid-state transformation of the precursor phase, leading to heterogeneous nucleation of magnetite nanoparticles. With time, the entire (precursor) surface underwent transformation to magnetite, leaving a surface made only of magnetite. Solutions sprayed on this surface then involved only the nucleation and growth of magnetite only.

3. **Nanoparticle self-assembly:** The latter stages of deposition involved self-assembly of

nucleating magnetite nanoparticles into hierarchically organized morphologies. Self-assembly of nanoparticles can be envisaged to occur within the droplets before depositing on the substrate and also, directly on the substrate. The final morphology was directly dependent on rate of nanoparticle aggregation. The latter was in turn dependent on two major factors: a) rate of solid (nanoparticle) formation (controlled by solution chemistry and flow rates) and, b) liquid residence time (controlled by solution flow rates and platen rotation rate). When the rate of solid formation matched with the residence time required to assemble in an organized fashion (as in the case of dense films), isotropic and near-equilibrium crystal shapes were observed. On the other hand, when the rate of solid formation was high as compared to liquid residence times, particle assembly was less organized, leading to unusual morphologies such as the columnar stacks of mosaic discs (porous films).

The above discussion is based on studies pertaining to magnetite (or the family of iron oxides). However, it is expected that similar mechanisms would be involved in solution synthesis of other metal oxides by spin spray deposition. Thus, a holistic approach towards microstructure development in spin spray deposition would involve optimization of various process parameters to control each of the above mechanisms.

Future work:

Through this research, a qualitative description of non-classical crystallization pathways in the spin spray deposition of magnetite films has been given. A quantitative description of thermodynamic and kinetic phenomena leading to the nucleation of precursor phases (instead of magnetite) still needs to be explored. Crystal nucleation is dependent on the supersaturation of the solutions. Determination of supersaturation in a single homogeneous bulk solution (as a function of solution pH and concentration) has been demonstrated by Zhang et al.[90]. However, with SSD, supersaturation in the liquid phase is brought about by reaction of droplets from two different solutions. In other words, solution mixing in micro-volumes brings about solid formation. Hence, determination of true supersaturation would require an understanding of droplet mixing. Droplet mixing is also influenced by the dynamics of the rotating platen. Hence, a combination of computational fluid dynamics (to understand micro-droplet mixing) and thermodynamic modeling (to predict phase stability) is needed for construction of a predictive model to control the phase of nucleating material, rate of solid formation and particle self-assembly.

Another key aspect would be the evaluation of magnetic behavior of these films to identify key areas of applications. As mentioned previously, dense magnetite films are of particular interest to the electromagnetics community owing to their improved high frequency magnetic permeability. Magnetic property measurement of films deposited by bicarbonate based oxidant solutions, followed by comparison to existing studies by Ray et al. [3, 31] on ferrite films with ammonia/acetate based oxidant solutions, can give an insight into the key factors of synthesis that control the film performance. A variety of anisotropic nanostructures were observed in porous films. Effect on these unusual morphologies on the directionality of magnetic properties can be evaluated by techniques such as superconducting quantum interference device (SQUID) magnetometry and electron holography.

REFERENCES

1. De Yoreo, J.J., et al., *Crystallization by particle attachment in synthetic, biogenic, and geologic environments.* Science, 2015. **349**(6247): p. aaa6760.

2. Cölfen, H. and M. Antonietti, *Mesocrystal Systems*, in *Mesocrystals and Nonclassical Crystallization*. 2008, John Wiley & Sons, Ltd. p. 113-177.

3. Zhang, D., et al., *Magnetic domain structure in nanocrystalline Ni-Zn-Co spinel ferrite thin films using off-axis electron holography.* Journal of Applied Physics, 2014. **116**(8): p. 083901.

4. Zhang, Q., S.-J. Liu, and S.-H. Yu, *Recent advances in oriented attachment growth and synthesis of functional materials: concept, evidence, mechanism, and future.* J. Mater. Chem., 2009. **19**(2): p. 191-207.

5. Yoreo, J.J.D. and P.G. Vekilov, *Principles of nucleation and growth.* Reviews in Mineralogy and Geochemistry, 2003. **54**: p. 57-93.

6. Cölfen, H. and M. Antonietti, *Examples of Crystals Challenging the Classical Textbook Mechanism*, in *Mesocrystals and Nonclassical Crystallization*. 2008, John Wiley & Sons, Ltd. p. 51-72.

7. Penn, R. and J. Banfield, *Morphology development and crystal growth in nanocrystalline aggregates under hydrothermal conditions: Insights from titania.* Geochimica et Cosmochimica Acta,, 1999. **63**(10): p. 1549–1557.

8. Niederberger, M. and H. Colfen, *Oriented attachment and mesocrystals: non-classical crystallization mechanisms based on nanoparticle assembly.* Phys Chem Chem Phys, 2006. **8**(28): p. 3271-87.

9. V.K.Ivanov., et al., *Oriented attachment of particles- 100 years of investigations of non-classical growth.* Russian Chemical Reviews, 2014. **83**(12): p. 1204-1222.

10. Penn, R.L., *Kinetics of Oriented Aggregation.* The Journal of Physical Chemistry B, 2004. **108**(34): p. 12707-12712.

11. Ikeda, T., Y. Oaki, and H. Imai, *Thin films that consist of CuO mesocrystal nanosheets: an application of microbial-mineralization-inspired approaches to thin-film formation.* Chem Asian J, 2013. **8**(9): p. 2064-9.

12. Ocaña, M., M.P. Morales, and C.J. Serna, *The Growth Mechanism of α-Fe2O3 Ellipsoidal Particles in Solution.* Journal of Colloid and Interface Science, 1995. **171**(1): p. 85-91.

13. Shindo, D., et al., *Internal Structure Analysis of Monodispersed Peanut-Type Hematite Particles Produced by the Gel-Sol Method.* Journal of Colloid and Interface Science, 1994. **168**(2): p. 478-484.

14. Niederberger, M., et al., *An Iron Polyolate Complex as a Precursor for the Controlled Synthesis of Monodispersed Iron Oxide Colloids.* Chemistry of Materials, 2002. **14**(1): p. 78-82.

15. Lee Penn, R., J.J. Erbs, and D.M. Gulliver, *Controlled growth of alpha-FeOOH nanorods by exploiting-oriented aggregation.* Journal of Crystal Growth, 2006. **293**(1): p. 1-4.

16. Yu, D., et al., *Oriented assembly of Fe3O4 nanoparticles into monodisperse hollow single crystal microspheres.* Journal of Physical Chemistry B, 2006. **110**(21667-21671).

17. Liu, X., et al., *Ionic liquid-assisted solvothermal synthesis of oriented self-assembled Fe3O4 nanoparticles into monodisperse nanoflakes.* CrystEngComm, 2013. **15**(17): p. 3284.

18. Wan, J., et al., *Insight into the formation of magnetite mesocrystals from ferrous precursors in ethylene glycol.* Chem Commun (Camb), 2015. **51**(88): p. 15910-3.

19. Alexandra Navrotsky, L.M., Juraj Majzlan, *Size driven structural and thermodynamic complexity in iron oxides.* Science, 2008. **319**: p. 1635-1638.

20. Navrotsky, A., *Energetic clues to pathways to biomineralization: precursors, clusters, and nanoparticles.* Proc Natl Acad Sci U S A, 2004. **101**(33): p. 12096-101.

21. Gao, Y. and K. Koumoto, *Bioinspired Ceramic Thin Film Processing: Present Status and Future Perspectives.* Crystal Growth & Design, 2005. **5**(5): p. 1983-2017.

22. Niesen, T.P. and M.R. De Guire, *Review: Deposition of Ceramic Thin Films at Low Temperatures from Aqueous Solutions.* Journal of Electroceramics, 2001. **6**(3): p. 169-207.

23. Masanori, A. and T. Yutaka, *Ferrite-Plating in Aqueous Solution: A New Method for Preparing Magnetic Thin Film.* Japanese Journal of Applied Physics, 1983. **22**(8A): p. L511.

24. Abe, M., *Ferrite plating: a chemical method preparing oxide magnetic films at 24–100°C, and its applications.* Electrochimica Acta, 2000. **45**: p. 3337-3343.

25. Abe, M. and Y. Tamaura, *Ferrite plating in aqueous solution: New technique for preparing magnetic thin film.* Journal of Applied Physics, 1984. **55**(6): p. 2614-2616.

26. Abe, M., et al., *Ultrasound enhanced ferrite plating; bringing breakthrough in ferrite coating synthesized from aqueous solution.* IEEE Transactions on Magnetics, 1997. **33**(5): p. 3649-3651.

27. Supothina, S., M.R. de Guire, and A.H. Heuer, *Nanocrystalline Tin Oxide Thin Films via Liquid Flow Deposition.* Journal of the American Ceramic Society, 2003. **86**(12): p. 2074-2081.

28. Abe, M., et al., *High speed deposition of high-quality ferrite films from aqueous solution at low temperatures (≤90 °C).* Journal of Applied Physics, 1987. **61**(8): p. 3211-3213.

29. Abe, M., et al., *Plating of ferrite film on 8" disc at 70°C by "spray-spin-coating" method.* IEEE Transactions on Magnetics, 1987. **23**(5): p. 3432-3434.

30. Kondo K., C.T., Yoshida S., Okamoto S., Shimada Y., Matsushita N., Abe M., *FMR Study on Spin-Sprayed Ni-Zn-Co Ferrite Films With High Permeability Usable for GHz Noise Suppressors.* IEEE Transactions on Magnetics, 2005. **41**(10).

31. Ray, N., *Synthesis and Characterization of Nanocrystalline Nickel-Zinc Spinel Ferrite Thin Films Using the Spin-Spray Deposition Method.* Proquest Dissertations and Theses, 2013.

32. Physics, K.L.I.f.N.a.R. https://fys.kuleuven.be/iks/nvsf/experimental-facilities/x-ray-diffraction-2013-bruker-d8-discover.

33. http://nptel.ac.in/courses/102103047/module6/lec34/1.html.

34. http://www.nanoimages.com/sem-technology-overview/.

35. Shah, A. *Transmission Electron Microscope*. 6th Advanced Materials Characterization Workshop, 2012.

36. Matsushita N., C.C.P., Mizutani T., Abe M., *Ni–Zn ferrite films with high permeability (mu'=~30, mu"=~30) at 1 GHz prepared at 90°C.* Journal of Applied Physics, 2002. **91**(10).

37. Matsushita N., N.T., Abe M, *Ni–Zn–Co Ferrite Films Prepared at 90 C Having mu"= 30 at 3GHz.* IEEE Transactions on Magnetics, 2002. **38**(5).

38. Ailoor S.K., T.T., Kondo K., Tada M., Nakagawa T., Abe M., Yoshimuraa M. and Matsushita N., *Coupling of MnZn-ferrite films onto electronic components by a novel solution process for high frequency applications.* Journal of Materials Chemistry 2009. **19**: p. 5510-5517.

39. Mirabello, G., J.J.M. Lenders, and N.A.J.M. Sommerdijk, *Bioinspired synthesis of magnetite nanoparticles.* Chemical Society Reviews, 2016. **45**(18): p. 5085-5106.

40. Ahn, T., et al., *Formation Pathways of Magnetite Nanoparticles by Coprecipitation Method.* The Journal of Physical Chemistry C, 2012. **116**(10): p. 6069-6076.

41. Jolivet, J.-P., E. Tronc, and C. Chanéac, *Iron oxides: From molecular clusters to solid. A nice example of chemical versatility.* Comptes Rendus Geoscience, 2006. **338**(6-7): p. 488-497.

42. Jolivet, J.P., C. Chaneac, and E. Tronc, *Iron oxide chemistry. From molecular clusters to extended solid networks.* Chem Commun (Camb), 2004(5): p. 481-7.

43. Mackay, A., *Green rust- a pyoraurite type structure (reply).* Nature, 1976. **263**: p. 353.

44. McGill, I., B. McEnaney, and D. Smith, *Crystal structure of green rust formed by corrosion of cast iron.* Nature, 1976. **259**(5540): p. 200-201.

45. Taylor, R., *Formation and properties of Fe (II) Fe (III) hydroxy-carbonate and its possible significance in soil formation.* Clay minerals, 1980. **15**(4): p. 369-382.

46. Benício, L.P.F., et al., *LAYERED DOUBLE HYDROXIDES: NANOMATERIALS FOR APPLICATIONS IN AGRICULTURE.* Revista Brasileira de Ciência do Solo, 2015. **39**: p. 1-13.

47. Mackay, A., *The Oxides and Hydroxides and Their Structural Inter-relationships.* Croatica Chemica Acta, 1959. **31**.

48. Mackay, A., *Some aspects of the topochemistry of the iron oxides and hydroxides.* Proceedings of the Fourth International Symposium on the Reactivity of Solids Amsterdam, 1960: p. 571-583.

49. Ruby, C., et al., *Oxidation modes and thermodynamics of FeII-III oxyhydroxycarbonate green rust: dissolution-precipitation versus in-situ deprotonation; about the fougerite mineral*. 2009.

50. Penn, R.L., et al., *Epitaxial Assembly in Aged Colloids.* The Journal of Physical Chemistry B, 2001. **105**(11): p. 2177-2182.

51. Petuskey, W., *Nanoferrite overview.* 2010.

52. Schneider, C.A., W.S. Rasband, and K.W. Eliceiri, *NIH Image to ImageJ: 25 years of Image Analysis.* Nature methods, 2012. **9**(7): p. 671-675.

53. Biswas, S., et al., *Structural study of TiO2 hierarchical microflowers grown by aerosol-assisted MOCVD.* CrystEngComm, 2017. **19**(11): p. 1535-1544.

54. Penn, R.L., D. Li, and J. Soltis, *A Perspective on the Particle-Based Crystal Growth of Ferric Oxides, Oxyhydroxides, and Hydrous Oxides*. Vol. 20. 2017. 257-273.

55. Oswald H.R., F.W., Brunner P., From Molecule to Cell: Symposium on Electron Microscopy (Ed. P. Buffa), CNR, Roma, 1964: p. 141.

56. Myers, J.C. and R.L. Penn, *Controlling heterogenite particle morphology and microstructure by varying synthetic conditions.* Materials Research Bulletin, 2011. **46**(5): p. 649-657.

57. Cölfen, H. and M. Antonietti, *Mechanisms of Mesocrystal Formation*, in *Mesocrystals and Nonclassical Crystallization*. 2008, John Wiley & Sons, Ltd. p. 179-236.

58. Legrand, L., et al., *Electroanalytical and kinetic investigations on the carbonate green rust-Fe (III) redox system.* Journal of the Electrochemical Society, 2003. **150**(2): p. B45-B51.

59. Kassim, J., T. Baird, and J. Fryer, *Electron microscope studies of iron corrosion products in water at room temperature.* Corrosion Science, 1982. **22**(2): p. 147-158.

60. Song, C., et al., *Design, controlled synthesis, and properties of 2D CeO2/NiO heterostructure assemblies.* CrystEngComm, 2017. **19**(48): p. 7339-7346.

61. Ortega, K.F., et al., *Topotactic Synthesis of Porous Cobalt Ferrite Platelets from a Layered Double Hydroxide Precursor and Their Application in Oxidation Catalysis.* Chemistry - A European Journal, 2017. **23**(51): p. 12443-12449.

62. Gunter, J.R., Oswald, Hans-Rudolf, *Attempt to a systematic classification of topotactic reactions.* Bulletin of the Institute for Chemical Research, Kyoto University 1975. **53**(2): p. 249-255.

63. Momma, K. and F. Izumi, *VESTA 3 for three-dimensional visualization of crystal, volumetric and morphology data.* Journal of Applied Crystallography, 2011. **44**(6): p. 1272-1276.

64. *CrystalMaker®: a crystal and molecular structures program for Mac and Windows. CrystalMaker Software Ltd, Oxford, England.*

65. Banfield, J.F., et al., *Aggregation-Based Crystal Growth and Microstructure Development in Natural Iron Oxyhydroxide Biomineralization Products.* SCIENCE, 2000. **289**: p. 751-754.

66. Frandsen, C., et al., *Aggregation-induced growth and transformation of [small beta]-FeOOH nanorods to micron-sized [small alpha]-Fe2O3 spindles.* CrystEngComm, 2014. **16**(8): p. 1451-1458.

67. Navrotsky, A., L. Mazeina, and J. Majzlan, *Size-Driven Structural and Thermodynamic Complexity in Iron Oxides.* Science, 2008. **319**(5870): p. 1635-1638.

68. Chernyshova, I.V., M.F. Hochella Jr, and A.S. Madden, *Size-dependent structural transformations of hematite nanoparticles. 1. Phase transition.* Physical Chemistry Chemical Physics, 2007. **9**(14): p. 1736-1750.

69. Schaefer, M.V., C.A. Gorski, and M.M. Scherer, *Spectroscopic Evidence for Interfacial Fe(II)−Fe(III) Electron Transfer in a Clay Mineral.* Environmental Science & Technology, 2011. **45**(2): p. 540-545.

70. Williams, A.G.B. and M.M. Scherer, *Spectroscopic Evidence for Fe(II)−Fe(III) Electron Transfer at the Iron Oxide−Water Interface.* Environmental Science & Technology, 2004. **38**(18): p. 4782-4790.

71. Yang, L., et al., *Kinetics of Fe(II)-Catalyzed Transformation of 6-line Ferrihydrite under Anaerobic Flow Conditions.* Environmental Science & Technology, 2010. **44**(14): p. 5469-5475.

72. Kostov, I., *Mineralogy*. 1968, Edinburgh; London: Oliver & Boyd.

73. Santos-Carballal, D., et al., *A DFT study of the structures, stabilities and redox behaviour of the major surfaces of magnetite Fe3O4.* Physical Chemistry Chemical Physics, 2014. **16**(39): p. 21082-21097.

74. Cornell, R.M. and U. Schwertmann, *Crystal Morphology and Size*, in *The Iron Oxides*. 2004, Wiley-VCH Verlag GmbH & Co. KGaA. p. 59-94.

75. Parikh, H. and M.R. De Guire, *Recent progress in the synthesis of oxide films from liquid solutions.* Journal of the Ceramic Society of Japan, 2009. **117**(1363): p. 228-235.

76. Goto, Y., et al., *Improvement in Deposition Rate and Quality of Films Prepared by "Thin Liquid-Film" Ferrite Plating Method.* IEEE Translation Journal on Magnetics in Japan, 1988. **3**(2): p. 159-165.

77. Goto, Y., et al., *Ferrite Plating by Means of Thin Film of Reaction Solution; "Thin Liquid-Film Method".* IEEE Translation Journal on Magnetics in Japan, 1987. **2**(3): p. 235-236.

78. Lipowsky, P., et al., *Controlling the Assembly of Nanocrystalline ZnO Films by a Transient Amorphous Phase in Solution.* The Journal of Physical Chemistry C, 2008. **112**(14): p. 5373-5383.

79. Guire, M.R.D., et al., *Chemical Bath Deposition*, in *Chemical Solution Deposition of Functional Oxide Thin Films*, T. Schneller, et al., Editors. 2013, Springer Vienna: Vienna. p. 319-339.

80. Verwey, E.J.W., *Theory of the Stability of Lyophobic Colloids.* The Journal of Physical and Colloid Chemistry, 1947. **51**(3): p. 631-636.

81. He, W., et al., *The evaluation of Coulombic interaction in the oriented-attachment growth of colloidal nanorods.* Analyst, 2012. **137**(21): p. 4917-4920.

82. He, W., et al., *An analytical expression for the van der Waals interaction in oriented-attachment growth: a spherical nanoparticle and a growing cylindrical nanorod.* Physical Chemistry Chemical Physics, 2012. **14**(13): p. 4548-4553.

83. Herrington, T.M. and B.R. Midmore, *The rapid aggregation of dilute suspensions: An experimental investigation of Smoluchowski's theorem using photon correlation spectroscopy.* Powder Technology, 1991. **65**(1): p. 251-256.

84. Han, L., Y. Chen, and Y. Wei, *Hierarchical flower-like Fe3O4 and [gamma]-Fe2O3 nanostructures: Synthesis, growth mechanism and photocatalytic properties.* CrystEngComm, 2012. **14**(14): p. 4692-4698.

85. Li, G., J. Lan, and G. Li, *Chrysanthemum-like 3D hierarchical magnetic [gamma]-Fe2O3 and Fe3O4 superstructures: facile synthesis and application in adsorption of organic pollutants from water.* RSC Advances, 2015. **5**(3): p. 1705-1711.

86. Li, X., et al., *Hierarchically structured Fe3O4 microspheres: morphology control and their application in wastewater treatment.* CrystEngComm, 2011. **13**(2): p. 642-648.

87. Datta, K.J., et al., *Synthesis of flower-like magnetite nanoassembly: Application in the efficient reduction of nitroarenes.* Scientific Reports, 2017. **7**(1): p. 11585.

88. Rao, A. and H. Cölfen, *Mineralization Schemes in the Living World: Mesocrystals*, in *New Perspectives on Mineral Nucleation and Growth: From Solution Precursors to Solid Materials*, A.E.S. Van Driessche, et al., Editors. 2017, Springer International Publishing: Cham. p. 155-183.

89. Cölfen, H. and M. Antonietti, *Physico-Chemical Principles of Crystallization*, in *Mesocrystals and Nonclassical Crystallization*. 2008, John Wiley & Sons, Ltd. p. 7-50.

90. Zhang, G., et al., *Titanium Oxide Nanoparticles Precipitated from Low-Temperature Aqueous Solutions: I. Nucleation, Growth, and Aggregation.* Journal of the American Ceramic Society, 2008. **91**(12): p. 3875-3882.